ABSTRACT

Title of dissertation: AN APPARATUS FOR LIGHT-LESS ARTIFICIAL GAUGE FIELDS AND NEW IMAGING TECHNIQUES

Abigail Perry, Doctor of Philosophy, 2015

Dissertation directed by: Dr. I.B. Spielman and Professor S.L. Rolston
Joint Quantum Institute,
National Institute of Standards and Technology
and
University of Maryland Department of Physics

The thesis presented has three components: experiments with artificial vector potentials, a new atom-chip apparatus designed and built for light-less fictitious gauge fields, and an imaging experiment. First, we introduce experiments with light-induced vector potentials using two-photon Raman coupling to simulate charged particles using charge neutral Bose-Einstein condensates (BECs). Depending on the spatial and temporal properties of the engineered vector potential, it is possible for ultracold atoms to experience different variants of an effective Lorenz force such as; magnetic fields, electric fields, and spin-orbit coupling, via coupling between an atom's internal spin and its linear momentum. In this context, we discuss the main focus of this thesis, the design and construction of an atom-chip apparatus for ^{87}Rb BECs for experiments with light-less artificial gauge fields. Eliminating the source of heating due to spontaneous emission will open new paths to explore

artificial gauge fields in alkali fermions and will be a step towards the realization of simulated topological insulators using ultracold atoms. Finally, we will describe in detail an imaging experiment performed on this new apparatus, the reconstruction of the two-dimensional column density of a BEC using multiple defocused images taken simultaneously.

AN APPARATUS FOR LIGHT-LESS ARTIFICIAL GAUGE FIELDS AND NEW IMAGING TECHNIQUES

by

Abigail Reiko Perry

Dissertation submitted to the Faculty of the Graduate School of the
University of Maryland, College Park in partial fulfillment
of the requirements for the degree of
Doctor of Philosophy
2015

Advisory Committee:
Dr. Ian Spielman, Advisor
Professor Steve Rolston, Chair
Professor Mario Dagenais, Dean's Representative
Professor Christopher Monroe
Dr. Trey Porto

Dedication

To Machiko, Christopher, Justin, and Malcolm Perry

Table of Contents

List of Tables

List of Figures

Chapter 1: Introduction

My research has been divided between three separate but related laboratories. The focus of my Ph.D. work from 2011-2015 at the University of Maryland has been on the development of a new atom-chip based quantum simulation experiment in the Laser Cooling and Trapping Group on the campus of the National Institute of Standards and Technology (NIST) Gaithersburg. During 2008-2010, I worked on the University of Maryland campus as part of the team developing an ultracold Rb-Li quantum degenerate mixtures experiment. Prior to this, I spent 1.5 years at NIST working in the lab that first created artificial gauge fields for Bose-Einstein Condensates. In each of these labs, I worked with a number of different talented people, all under the supervision of Ian Spielman. Here, I discuss my initial work on light-induced artificial vector potentials, setting the stage for my current project, light-less artificial gauge fields. This project's goal is the simulation of topological matter [1] and for quantum simulation using an atom-chip. Finally, I will describe our most recent imaging experiment performed with the new apparatus.

Light-induced gauge fields: Ultracold atoms are highly controllable and tunable, making them an ideal platform for simulating and studying idealized condensed matter systems that are often difficult to probe in the absence of disorder.

These systems include the integer and fractional quantum Hall effects in a two-dimensional electron gas. These topological insulators are isolated from the environment, providing dissipation-less edge currents while insulating in the bulk. To learn more about these fascinating states of matter, we endeavor to make neutral quantum gases behave as charged particles in a magnetic field.

In our experiments, the Hamiltonian of a charge neutral ^{87}Rb Bose-Einstein condensate (BEC) is engineered to simulate the Hamiltonian of a charged particle by introducing an artificial vector potential $\mathbf{A}$ into the system. The momentum, $\mathbf{p}$, of the atom's contribution to the kinetic energy, $\mathbf{p}^2/2m$, is changed to $\mathbf{p} \rightarrow \mathbf{p} - q\mathbf{A}$, characteristic of a charged particle in an electromagnetic field. In our work detailed in Ref. [2], a spatially uniform vector potential was demonstrated with a BEC using a pair of counter-propagating Raman laser beams. The two-photon Raman transition couples the atom's internal state to its linear momentum. The dressed-state dispersion relation becomes $E \approx (\mathbf{p} - q\mathbf{A})^2/2m^*$, so that the atom has an effective mass $m*$, and the location of the shifted energy minimum determines the strength of the vector potential. The relative strength of the vector potential is experimentally tunable with the Raman detuning δ (using a bias magnetic field to change the Zeeman shift), and coupling, which is dependent on the Raman laser intensity. In the experiment, we measured the vector potential's dependence on δ at different Raman coupling strengths, which agreed with a single-particle model. We visualized the composition of the spin-momentum coupled dressed states by diabatically removing the Raman coupling and applying a magnetic field gradient to Stern-Gerlach separate the internal spin states after time of flight.

This experiment served as a stepping stone to subsequent experiments with non-uniform vector potentials in our laboratory as well as others. These experiments include artificial magnetic and electric fields, spin-orbit coupling, higher order partial waves, Zitterbewegung, and the spin Hall effect (publications [3], [4], and [5], respectively).

Light-less artificial gauge fields: During my third year of graduate school, I started my main thesis project, where I designed and constructed an apparatus for ^{87}Rb BECs. This apparatus will enable experiments with light-less artificial gauge fields using a nanofabricated in-vacuum atom-chip. The chip will be used solely for the purpose of creating these vector potentials; not, as is common, for BEC production. This work strives to realize artificial vector potentials that are unachievable using the traditional method which employs Raman laser beams.

To make significant progress in engineering vector potentials for alkali fermions, which could realize topological insulators, heating due to spontaneous emission must be overcome. The heating diminishes the lifetime of a Raman dressed cloud, and limits the time during which an experiment can be performed. To achieve sufficient Raman coupling strength with minimal heating, the single-photon detuning of a Raman beam must be of order the excited state fine structure splitting. However, for alkali fermions, heating due to scattering becomes prohibitive at these detunings due to their small excited state fine structure. For example, the splitting in ^{87}Rb is one-thousand times that of ^{6}Li.

The light-induced Raman coupled Hamiltonian arises from the vector light-shift of the Raman laser beams. The vector light-shift may be interpreted as an

effective, spatio-temporally oscillating magnetic field. We propose to mimic this interaction using the real oscillating (radio-frequency (RF)) magnetic fields from an atom-chip [6]. A nanofabricated atom chip with micron scale wires will achieve comparable length scales to the light-induced case, and the near-field magnetic fields ≈ 5 μm from the chip surface will provide sufficient coupling strengths. Because of this, the chip must be placed in-vacuum. Additionally, the individual control over the atom-chip wires will allow for fine spatial variations in the Raman coupling strengths not previously possible, such as abrupt turn-off of the coupling (within one lattice period ≈ 3 μm) on the edges to create edge states. The first prototype of the chip is currently being bench tested in the laboratory.

The apparatus itself has been built and reliably produces ^{87}Rb BECs with highly stable atom number. We use standard laser cooling techniques to magnetically trap a cloud of atoms at of order 10 μK from room temperature vapor in a spin-polarized ground state. We trap in the F=2 manifold and take advantage of the factor of two gained in the trap strength over the F=1 manifold. We magnetically transport the atoms 44 cm vertically in $\approx$2 s, and achieve BEC in a crossed dipole trap using the techniques described in [7]. We then microwave-transfer the atoms into the ground $|F = 1, m_F = -1\rangle$ state during dipole evaporation to reach degeneracy. While the chip is under development, we performed our first imaging experiment with the new apparatus.

Multiple off-resonance defocused imaging: In cold atom experiments, each image of light refracted and absorbed by an atomic ensemble, carries a remarkable amount of information. Numerous imaging techniques including absorption,

fluorescence, phase-contrast (PCI), and off-resonance defocused (ORD) imaging are commonly used. We extend ORD to image BECs. In the ORD method, there exists an exact solution to the wave equation. This defines a direct relationship (transfer function) between the intensity of the probe light which has interacted with the atoms and the two-dimensional column density of the atomic cloud. This transfer function, used to compute the column density, is characterized by divergences at certain spatial frequencies. The locations of these divergences are dependent on the detector distance z from the focus. By placing multiple detectors with different degrees of defocus, we eliminate these systematic artifacts present in the ORD method.

Experimentally, the multiple-camera off-resonance defocused (MORD) method may be incorporated into existing set-ups with minimal additional equipment. We use two non-polarizing beam splitters to divide the atomically absorbed and phase shifted beam into three beams with nominally equal intensities. We simultaneously capture the images using three cameras placed at different distances away from the focal plane. Combining the three images eliminates the shot-noise amplification that occurs at the divergences of single-camera reconstructions.

Further, our simulations of absorption, PCI, and MORD imaging show that the statistical uncertainty in the measured optical depth using MORD imaging is comparable to or below those of other imaging techniques.

Chapter 2: Artificial Gauge Fields

2.1 Introduction to light-induced vector potentials

Here, we discuss the concept of "artificial gauge fields" [8–10] in which we apply an *engineered* vector potential $\mathbf{A}$ to a BEC [11, 12]. The high experimental controlability and tunability of BECs make them ideally suited for this endeavor. An ultracold atomic gas in the presence of $\mathbf{A}$ can simulate various interesting condensed matter phenomena [13, 14] that are difficult or impossible to probe in actual condensed matter systems. The spatial and temporal properties of $\mathbf{A}$ realized in the experiment determine what phenomena is simulated.

We modify the Hamiltonian of a neutral atom $\hat{H} = \mathbf{p}^2/2m + V(\vec{r})$ to include a gauge field via the replacement $\mathbf{p} \rightarrow \mathbf{p} - q\mathbf{A}$, where $\mathbf{p}$ is the canonical momentum of the atom, and q is the artificial charge associated with the fictitious vector potential $\mathbf{A}$: so that the charge neutral atoms making up the BEC behave like charged particles interacting with an electromagnetic field. Depending on the properties of $\mathbf{A}$, the BEC may experience a fictitious magnetic field $\mathbf{B} = \nabla \times \mathbf{A}$ [15], electric field $\mathbf{E} = -\partial\mathbf{A}/\partial t$ [16], or more exotic effects such as spin-orbit coupling (SOC) from a matrix valued $\mathbf{A}$ [5, 17]. Our new atom-chip apparatus aims to expand on the fictitious gauge fields that have been studied thus far; in particular, spin-orbit

coupled physics. Therefore, in this chapter, we discuss the SOC case in detail. The engineered SOC Hamiltonian models a neutral ^{87}Rb atom as a charged particle in a solid, whose spin state is coupled to its linear momentum.

In solids with SOC, a particle moving with momentum $\hbar\mathbf{k} = \hbar(k_x, k_y, k_z)$ in a static electric field $\mathbf{E} = E_0\mathbf{e}_z$ in the laboratory frame experiences a magnetic field $\mathbf{B}_{SO} = E_0(\hbar/mc^2)(-k_y, k_x, 0)$ in its moving frame [17], where c is the speed of light and m is the mass of the particle. In the moving frame, the electron's magnetic moment $\boldsymbol{\mu}_{\mathrm{B}}$ couples via the Zeeman interaction to this field: $\hat{H}_z = -\boldsymbol{\mu}_{\mathrm{B}} \cdot \mathbf{B}_{SO}$. This effective Zeeman interaction, called Rashba SOC, couples the spin and linear momentum of the charged particle: $-\boldsymbol{\mu}_B \cdot \mathbf{B}_{SO} \propto \hat{\sigma}_x k_y - \hat{\sigma}_y k_x$, where $\hat{\sigma}_{x,y,z}$ are the Pauli matrices operating on the internal spin states. In two dimensions, linear SOC can be described by the sum of the Rashba term and the Dresselhaus ($\propto -\hat{\sigma}_x k_y - \hat{\sigma}_y k_x$) term. In a landmark experiment [17], a Hamiltonian was engineered in cold atoms to realize a system with equal Rashaba and Dresselhaus SOC:

$$\hat{H}_{SOC} = \frac{\hbar^2\hat{\mathbf{k}}^2}{2m}\hat{1} - [\hat{B} + \hat{B}_{SO}(\hat{\mathbf{k}})] \cdot \boldsymbol{\mu} = \frac{\hbar^2\hat{\mathbf{k}}^2}{2m}\hat{1} + \frac{\Omega}{2}\hat{\sigma}_z + \frac{\delta}{2}\hat{\sigma}_y + 2\alpha\hat{\mathbf{k}}_x\hat{\sigma}_y, \qquad (2.1)$$

where Ω is the Raman coupling strength, and δ is the detuning from Raman resonance. The constant α describes the SOC strength. Generally, α is fixed by the properties of a solid, and is only slightly-tunable in any given sample. However, in cold-atom systems, the coupling strength can be experimentally controlled [17] by changing the intersection angle between the Raman laser beams (for light-induced SOC), or by changing the "Raman" wire periodicity of an atom-chip. In the following, we describe the origin of these terms in the spin-orbit coupled Hamiltonian for

a neutral ^{87}Rb atom interacting with electromagnetic fields.

2.2 Experimental set-up

We use a Raman dressing scheme to introduce a vector potential into the Hamiltonian of a ^{87}Rb BEC. We start with the BEC in the magnetically trappable $5S_{1/2}$ ground hyperfine state $|F = 1, m_F = -1\rangle$, the atoms are then dressed with two Raman laser beams counter-propagating along $\mathbf{e}_x$ with frequencies ω_L and $\omega_L + \Delta\omega_L$, and orthogonal linear polarizations, as shown in Fig. 2.1. We apply a bias field $B_0\mathbf{e}_y$, which sets the quantization axis and Zeeman shifts the atom's hyperfine states. The atoms experience two-photon Raman transitions [18, 19] between the m_F levels of the ground $F = 1$ state with single-photon recoil momentum $\hbar k_r = 2\pi\hbar/\lambda$ from each Raman beam, where λ is the wavelength of the beams. We define recoil energy $E_r = \hbar^2 k_r^2/2m$, where m is the mass of the atom.

The general set-up described by Fig. 2.1 is used in all of the fictitious gauge field experiments performed on the "RbK" apparatus, with slight variations in the values of λ, B_0, and the intersection angle between the two Raman laser beams. Next, we discuss the Hamiltonian of the Raman dressed atom.

2.3 Dressed state Hamiltonian: three-level case

The real-space Hamiltonian for a BEC dressed using the Raman coupling scheme described in Sec. 2.2 is

$$\hat{H} = \left[\frac{\hbar^2(k_y^2 + k_z^2)}{2m} + V(\mathbf{r})\right]\hat{1} + \hat{H}_x, \tag{2.2}$$

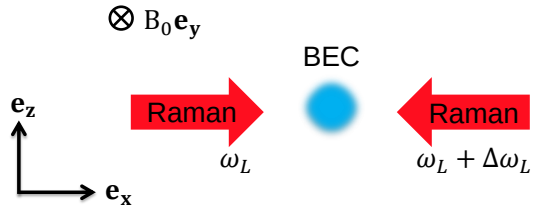

Figure 2.1: Raman coupling set-up. Two Raman laser beams counter-propagating along $\pm\mathbf{e}_x$ with crossed linear polarizations provide two-photon coupling between the magnetic sublevels m_F of the ground electronic state $5S_{1/2}$, $F = 1$ of ^{87}Rb. The $F = 1$ state is Zeeman split by an external magnetic field applied along $\mathbf{e}_y$ that defines the quantization axis. With respect to the quantization axis, the beams propagating along $\mathbf{e}_x$ and -$\mathbf{e}_x$ have polarizations π and σ, respectively.

where we may separate the Raman coupled part of the Hamiltonian, $\hat{H}_x$, from the rest of the Hamiltonian because the momentum transfer direction of the Raman beams is only along $\mathbf{e}_x$. The $\hat{H}_{y,z}$ Hamiltonian is that of a free particle (first term on the right-hand side), plus $V(\mathbf{r})$. The optical dipole trap provides the potential $V(\mathbf{r})$, and the unit matrix acting on the Zeeman split $F = 1$ spin space $|m_F\rangle \in \{|-1\rangle, |0\rangle, |+1\rangle\}$ is $\hat{1}$.

The coupling between the spin states in $\hat{H}_x$ comes from the atom-light interaction between the BEC and Raman beams. An atom interacts with the electric fields

$$E_1(\mathbf{r},t) = E_1 e^{ik_L x - i\omega_L t}\mathbf{e}_y, \text{ and } E_2(\mathbf{r},t) = E_2 e^{-ik_L x - i(\omega_L+\Delta\omega_L)t}\mathbf{e}_z \tag{2.3}$$

of the two Raman beams (Fig. 2.1). For beams of equal intensities $E_1 = E_2 = E_0$, the total electric field is

$$E_{\text{total}}(x,t) = E_0\left[e^{-ik_L x - i\omega_L t}\mathbf{e}_y + e^{ik_L x - i(\omega_L+\Delta\omega_L)t}\mathbf{e}_z\right]. \tag{2.4}$$

The interaction Hamiltonian arises from the vector light-shift proportional to $E^*_{\text{total}} \times E_{\text{total}}$, which behaves like an effective magnetic field $B_{eff} \propto -E_0^2 \cos(2k_L x + \Delta\omega t)\mathbf{e}_x$.

Along with the atom's magnetic moment $\mu = g_F m_F \mu_B$, this gives rise to the Raman interaction $\hat{H}_R = -\boldsymbol{\mu} \cdot \mathbf{B}_{eff}$. In the frame rotating at frequency $\Delta\omega_L$, and using the rotating-wave approximation, the interaction Hamiltonian in the basis of the bare spin states $\{|-1\rangle, |0\rangle, |+1\rangle\}$ is

$$\hat{H}_x/\hbar = \Omega_R/2 \begin{pmatrix} 0 & e^{i2k_L x} & 0 \\ e^{-i2k_L x} & 0 & e^{i2k_L x} \\ 0 & e^{-i2k_L x} & 0 \end{pmatrix}. \tag{2.5}$$

In momentum space, we use the spin-momentum basis to find the gauge transformed Hamiltonian

$$\hat{H}_x/\hbar = \begin{pmatrix} \hbar(k_x + 2k_L)^2/2m - \delta & \Omega_R/2 & 0 \\ \Omega_R/2 & \hbar k_x^2/2m - \epsilon & \Omega_R/2 \\ 0 & \Omega_R/2 & \hbar(k_x - 2k_L)^2/2m + \delta \end{pmatrix}. \tag{2.6}$$

The tunability associated with inducing artificial gauge fields in a cloud of ultracold neutral atoms is evident: the laser intensity determines the Raman Rabi frequency (coupling strength) Ω_R, the strength of the bias magnetic field determines the Zeeman shifts, i.e., the Zeeman detuning δ and the quadratic Zeeman shift $\epsilon/h = \epsilon_B B_0^2$, where $\epsilon_B = 7.1772 \times 10^{-2}$ kHz/G^2.

Diagonalization of $\hat{H}_x$ results in three eigenvalues $E_j(\tilde{k}_x)$, where $j = 1, 2, 3$. The properties of the resulting dispersion relations are largely dependent on the values of Ω_R, and δ. The quadratic Zeeman shift ϵ provides a small energy offset to the dispersion curves. Example plots of $E_j(\tilde{k}_x)$ are shown in the left-hand column of Fig. 2.2. The sans-Raman coupling, free-particle dispersion curves of the bare spin states are shown in black; the three Raman dressed energy bands are shown in red.

The lowest energy band is approximately harmonic about the dispersion minimum $\tilde{k}_{min}$: $E_{j=1}(\tilde{k}_x) \approx \hbar^2(\tilde{k}_x - \tilde{k}_{min})^2/2m^*$, where $\hbar\tilde{k}_{min} = qA$, and m^* is an effective mass. In Sec. 2.4.1, we discuss the procedure used to load atoms into the lowest energy dressed state $E_{j=1}$. The induced vector potential, given by the position of the dressed state minimum, is $\mathbf{A} = (A_x, 0, 0)$. This vector potential commutes with itself, i.e., $\mathbf{A}$ is "Abelian."

The Raman beams couple spin states with the atom's linear momenta; $|m_F, k_x\rangle$. The two-photon Raman transition couples adjacent m_F states, i.e. states that differ in angular momentum by $\hbar\Delta m_F = \pm\hbar$ and by linear momentum $2\hbar k_r$. The three Raman-coupled basis states [2, 20] are

$$\Psi(\tilde{k}_x) = \{|-1, \tilde{k}_x + 2k_r\rangle, |0, \tilde{k}_x\rangle, |+1, \tilde{k}_x - 2k_r\rangle\}. \tag{2.7}$$

Next, we describe the experimental sequence we developed to demonstrate the gauge field Hamiltonian 2.6, and describe the results.

2.4 Experimental procedure

2.4.1 Adiabatic dressing

In our first fictitious fields experiment [2], Raman dressing was used to create a light-induced, spatially uniform, effective vector gauge potential for a ^{87}Rb BEC in the $F = 1$ ground hyperfine state. This experiment, paved the way for the many non-uniform artificial gauge fields experiments that followed. The results of the uniform vector potential experiment agreed with the single-particle model described

above.

The experiment started with a BEC prepared in $|m_F = -1, k_x = 0\rangle$ to be loaded into the lowest energy $E_{j=1}(\tilde{k}_x)$ Raman dressed state. To adiabatically load into $E_{j=1}(\tilde{k}_x)$, the BEC must be loaded with quasimomentum $\tilde{k}_{min}$, which is where $\tilde{k}_x = 0$ when $\delta = 0$. However, a 3D BEC created in a hybrid quadrupole plus crossed-dipole trap using the methods described in Ref. [7], would start out in the dressed state $j = 1$ with quasimomentum $\tilde{k}_x = -2k_r$.

To transfer the atoms to the $\tilde{k}_x = 0$ state, the atoms are first RF dressed with RF frequency $\omega_{rf} = \Delta\omega_L$ and loaded into the lowest energy RF dressed state. This is a two step adiabatic process: first, the RF coupling is ramped onto the desired value in 1 ms with the detuning set far off resonance (by turning up the bias magnetic field). Then second, the detuning is ramped to resonance in 9 ms. Adiabaticity is easily reached because the RF-dressed band gap energy $\hbar\Omega_{RF}/\sqrt{2}$ where $\Omega_{RF}/2\pi = 12$ kHz has the affiliated time scale ≈ 20 μs, which is much less than the ramp times.

Next, the atoms in the lowest energy RF dressed state are Raman coupled by ramping on the Raman beams adiabatically (with respect to the energy gap $\approx \hbar\Omega_R$ between the dressed energy bands and the trap frequency along $\mathbf{e}_x$) to the desired Raman coupling strength Ω_R in 20 ms. The RF coupling is then turned off in 2 ms, leaving the atoms in the lowest energy Raman dressed state $j = 1$ with $\tilde{k}_x = 0$. Atoms in an effective vector potential (i.e. $\tilde{k}_{min} \neq 0$) may then be achieved by adiabatically ramping on a detuning δ away from Raman resonance ($\delta = 0$) in ≈ 20 ms. This combined coupling scheme was studied in Ref. [21].

The dressing procedure described for this particular experiment is common to all experiments (with variations in the exact energy and time scales) that followed, with the exception of the synthetic partial waves [3] experiment. This experiment observed effective higher order partial waves as a result of the modified collision interactions between two BECs that were Raman dressed with equal and opposite momenta. In the partial waves experiment, instead of preparing the atoms by loading them all into the energy minimum of the lowest energy dressed state, two spatially overlapping BECs were prepared with momenta $\pm 2k_L$. Since the BECs then load into the Raman dressed energy band at $k_{min} = \pm 2k_L$, the atoms oscillate in the optical trap. Because of this, the Raman dressing sequence was modified: the Raman beams were ramped on in 1 ms, still adiabatic with respect to the band gap, but fast compared to the quarter period of the optical trap frequency along $\mathbf{e}_x$. Doing so ensures the momenta of the two BECs remain the same during the dressing stage. At a quarter period, a BEC with non-zero starting momentum would maximally change its speed inside a harmonic trap.

Next, we discuss the techniques used to make measurements on a Raman dressed cloud after performing an experiment. Again, these techniques apply generally to any gauge fields measurements made in the lab, but we refer to the original vector potential experiment and discuss its results.

2.4.2 Measurements

The relative strength of the vector potential is experimentally found by measuring the spin and momentum decompositions of the Raman dressed BEC. Though a ground-state BEC has zero group velocity, the momenta of the three spin components under Raman dressing are dependent on the values of δ and Ω_R. To prepare for the measurement, we diabatically turn-off the Raman coupling (i.e. the Raman laser beams) and apply a magnetic field gradient to Stern-Gerlach separate the three spin states after time-of-flight (TOF). During TOF, the cloud ballistically expands and the three momentum components become spatially resolved, as shown in the right-hand column of Fig. 2.2. The presented data is spin- and momentum-separated along the vertical and horizontal axes, respectively. The on-resonance case, (a), shows the expected $\pm 2k_r$ momenta acquired by the $m_F = \pm 1$ states from the two-photon Raman coupling. At a non-zero detuning, $\hbar\delta = -2E_r$, shown in (b), all spin states have acquired a non-zero velocity, along with corresponding changes in the population fractions (such that the mean velocity remains zero).

2.5 Dressed state Hamiltonian: two-level case

We next describe the two-level Raman-coupled scheme used to realize SOC. Experimentally, we want to reduce the thee-level system into an effective two-level system and simulate the two spin states of a spin-1/2 fermion such as an electron. This is accomplished by applying a bias field large enough to detune the $m_F = +1$ state from Raman resonance with the $m_F = 0, -1$ states via the quadratic

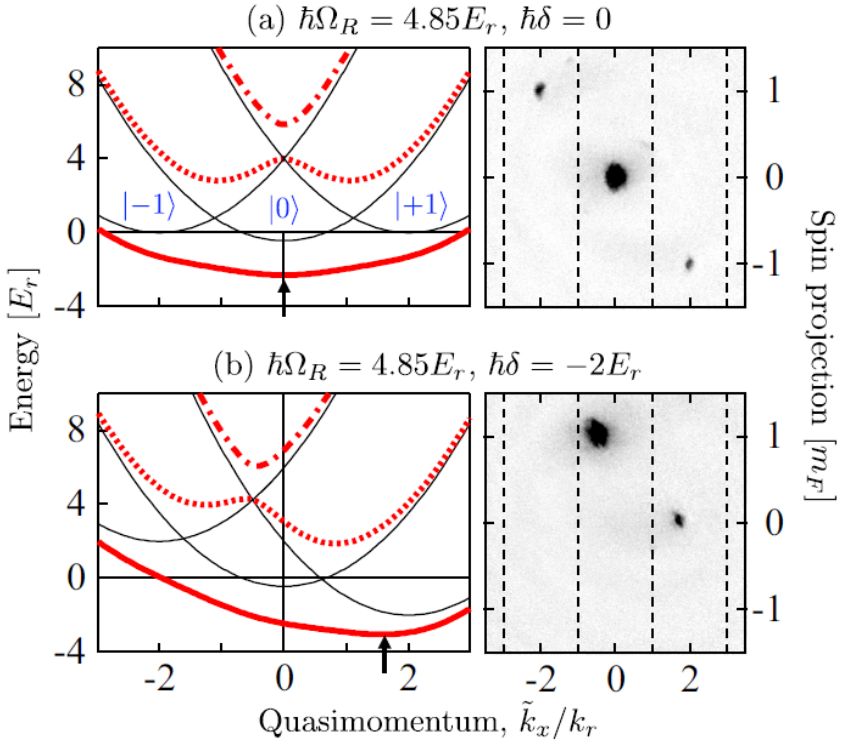

Figure 2.2: In the left-hand column, the bare spin free-particle dispersion curves are shown in black. The energy dispersion relations of the three Raman dressed eigenstates $E_j(\tilde{k}_x)$ where $j = 1...3$ are depicted in red. In the right-hand column are the corresponding images taken in the laboratory after TOF, which shows the spatially resolved spin and momentum decompositions of the Raman dressed state. In both cases (a) and (b), the atoms were dressed with Raman coupling strength $\hbar\Omega_R = 4.85\ E_r$, and quadratic Zeeman shift $\hbar\epsilon = 0.44\, E_r$. (a) $\hbar\delta = 0$, the minimum of the lowest energy dressed state $E_{j=1}$ is at $\tilde{k}_x = 0$, i.e. there is no effective vector potential. (b) $\hbar\delta = -2E_r$, the $E_{j=1}$ minimum, indicated by the black arrow, shifts to $\tilde{k}_{min} \neq 0$, so that each spin state acquires a non-zero phase velocity from the induced vector potential.

Zeeman shift ($|\epsilon| \geq |\delta|, \Omega$). The bias field $B_0\mathbf{e_y}$ provides the linear Zeeman shift $\omega_z/2\pi \approx 4.81$MHz, and the Raman beams have a fixed frequency difference $\Delta\omega_L \approx \omega_z$ (Fig. 2.3). We are left with two pseudo-spin states $|\uparrow\rangle = |F = 1, m_F = 0\rangle$ and $|\downarrow\rangle = |F = 1, m_F = -1\rangle$ with respect to the $\mathbf{e}_y$ quantization axis. The relevant coupled states are reduced to

$$\Psi(k_x) = \{|-1, k_x - k_L\rangle, |0, k_x + k_L\rangle\} \tag{2.8}$$

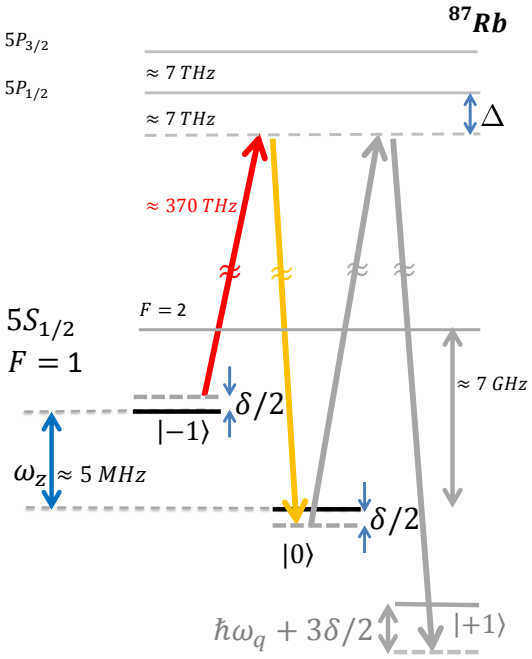

Figure 2.3: Two-level energy diagram for the spin-orbit coupling scheme. A two-photon Raman transition couples the atom's internal state to its linear momentum. The Raman laser beams have a single-photon detuning Δ, which is of order the excited state fine structure splitting. The Raman beams are detuned by δ from the $|-1\rangle$ and $|0\rangle$ Zeeman states. A large enough magnetic field provides the quadratic Zeeman shift of order the linear shift $|\epsilon| \geq |\delta|, \Omega$. This decouples the $|+1\rangle$ state from the $|-1\rangle$, $|0\rangle$ states (negligible Raman coupling to the $|+1\rangle$ state).

The Raman beam geometry was modified to intersect at $\theta = \pi/2$ for the SOC case [17] so that the new energy scale $E_L = \hbar^2 k_L^2/2m$, where $k_L = k_r \cos(\theta/2) = \sqrt{2}\pi/\lambda$. The associated two-level Hamiltonian is

$$\hat{H}_x/\hbar = \begin{pmatrix} \frac{\hbar}{2m}(k_x - k_L)^2 + \delta/2 & \Omega_R/2 \\ \Omega_R/2 & \frac{\hbar}{2m}(k_x + k_L)^2 - \delta/2 \end{pmatrix} \tag{2.9}$$

Here $\delta = \Delta\omega_L - \omega_z$ is the detuning from Raman resonance, and Ω_R is the Raman coupling frequency. The SO coupling strength $\alpha = E_L/k_L$ is a function of the Raman beam wavelength λ and intersection angle θ, but is independent of the Raman coupling strength Ω_R.

Diagonalization of the Hamiltonian for a given coupling strength Ω_R gives dispersion curves symmetric about quasimomentum $q = 0$ for $\delta = 0$ Fig. 2.4.

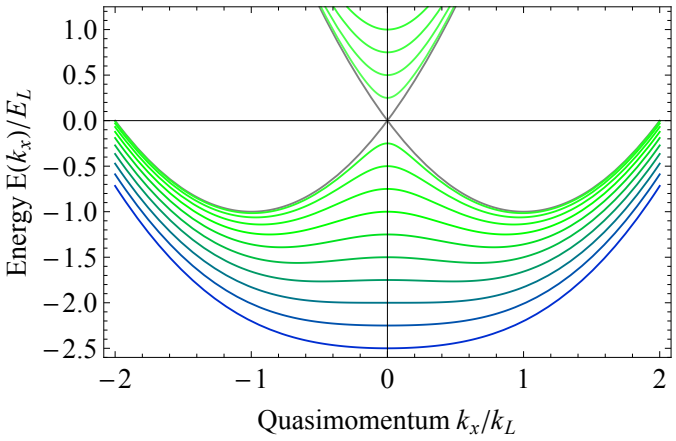

Figure 2.4: SOC dispersion curves. Black curves give the free-particle dispersion for the bare spin states absent Raman coupling. For small Raman coupling strengths $\Omega_R < 4E_L$, the Raman coupled dispersion has two minima. For large $\Omega_R > 4E_L$, the dispersion has a single minima. In both cases, the curvature about the minima has been modified from the free-particle case, so that the Raman-coupled atom has a single-particle effective mass m^*.

The dispersion curves are plotted for $\delta = 0$ and varying Raman coupling strengths Ω_R. In the SOC regime where $\hbar\Omega_R < 4E_L$, dispersion curves have two minima corresponding to dressed pseudo-spin states $|\uparrow'\rangle$ and $|\downarrow'\rangle$. For larger coupling strengths, the two minima combine into a single minimum, so that the system described is a spinless boson. The dressed states decompose into the bare spin states, and the location of the dressed minima are variable with δ. It is in the single-minimum regime that previous experiments realized artificial electric and magnetic fields [15, 16].

For non-zero detuning and $\hbar\Omega_R \gg 4E_L$, the dispersion minima k_{min} shifts. The new minima are approximately harmonic near $\tilde{k}_{min}$: $E(k_x) \approx \hbar^2(k_x \pm k_{min})^2/2m^*$, with effective mass $m^* = \hbar^2[d^2E(k_x)/dk_x^2]^{-1}$ determined by the dispersion curva-

ture. Dressed energies $E(k_x)$ are analogous to the Hamiltonian $(\mathbf{p} - q\mathbf{A})^2/2m$ for a particle with charge q interacting with vector potential $\mathbf{A}$. Then $\tilde{k}_{min} = qA/\hbar$ and the magnitude of $\mathbf{A}(\delta, \Omega_R)$ are bounded: $-2k_L < qA/\hbar < +2k_L$ [2]. The strength of the vector potential $\mathbf{A}$ determines the fraction of atoms in each spin and momentum state. Further, the strength, spatial, and temporal properties of $\mathbf{A}$ are experimentally controlled with different Raman beam intensities to vary coupling strength Ω_R, and properties of the detuning via changes in bias magnetic field (Zeeman shift) δ [15, 16].

It has been shown experimentally [17] that, absent Raman coupling, a BEC formed from $|\uparrow, k_x = \tilde{k}_x + k_L\rangle$ and $|\downarrow, k_x = \tilde{k}_x - k_L\rangle$ spatially mix. However, a quantum phase transition into SOC occurs when $\Omega_R = 0.19\, E_L$. In this regime, the dressed spin states spatially separate from effective spin interactions.

The two-minima regime of the two-level Raman dressed Hamiltonian was used to realize the spin-Hall effect (SHE) for the first time in a BEC. In the SHE, two spin states experience equal and opposite spin-dependent Lorentz-like forces. The force is orthogonally directed to the particle's direction of motion, in analogy to the Hall effect for charged particles. The SHE has been observed for electrons flowing in spin-orbit coupled condensed matter systems [22, 23]. In our experiment, we introduced spin-dependent Lorentz forces to pseudospin-1/2 ^{87}Rb BECs by engineering spin- and space-dependent vector potentials [5].

The experimental realization of the SHE built on the methods described for two-level Raman dressing of a ^{87}Rb BEC, with a key new feature: spatially inhomogeneous SOC. Since the Raman coupling strength is proportional to the intensity of

the Raman beams, the strength of Ω_R, and therefore of A, is dependent on where in space the atomic cloud is located inside the Raman beams' Gaussian intensity profile. The dynamic control over the optical trap beam allowed the Raman coupling to be both position and time dependent. The dressed state was prepared with equal populations in each (dressed) spin polarized state. The spin mixture was then suddenly displaced in the harmonic trap to a final displacement associated with a different Ω_R. Each spin state acquired momentum along $\mathbf{e}_x$, which was both opposite in direction for the two spins, and related to its final momentum along $\mathbf{e}_y$, characteristic of the SHE.

2.6 Dressed states without lasers: atom-chip experiment

2.6.1 Motivation

Going beyond spin-orbit coupling (SOC) achieved in previous bosonic ^{87}Rb experiments necessitates more involved experimental set-ups. For example, non-Abelian SOC requires Raman coupling in more than one-dimension. The Raman detuning, Δ, must provide sufficient Raman coupling $\Omega_R \propto 1/\Delta^2$, but also be far enough detuned from the excited state fine structure splittings to limit scattering. The scattering rate is proportional to $1/\Delta^2$, so that we quickly reach a limit as Δ is increased to minimize scattering. In the case of an optical dipole trap discussed in Sec. 2.7, scattering is not a limiting factor because the light-shift for large detunings scales as $1/\Delta$, so that a far-red detuned laser beam can provide strong confinement at high intensities. For sufficient Raman coupling and minimal scattering, the

optimal detuning from the ground to first excited fine structure (D1) transition is approximately equal to the excited state fine structure splitting, 7.1 THz for ^{87}Rb (Fig. 2.3).

Future experimental interests include the study of alkali fermions such as ^{40}K and ^{6}Li, for the modeling of topological insulators with neutral atoms. However, the light-induced Raman coupling scheme will result in high rates of scattering: the fine-structure splitting is only 1.7 THz for ^{40}K, and just 10 GHz for ^{6}Li. Therefore, the lifetime for moderate Raman coupling strengths will be limited by large spontaneous emission rates. This limit on experimental lifetime imposed by scattering rates suggests the need for a non-optical coupling method.

2.6.2 Light-less "Raman" coupling

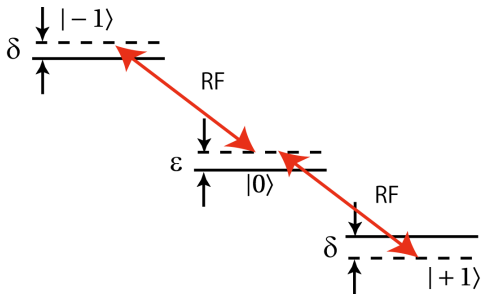

Figure 2.5: The magnetic sublevels of the ground hyperfine $F = 1$ state are Raman coupled with RF fields from an atom-chip. The RF frequency detuned δ from RF resonance couples the spin states (pictured). An RF field has the wavelength scale $\approx$ 10 m, compared to the length scale $\approx$ 800 nm associated with Raman transitions using laser light. Thus, the length scale associated with an RF field is not appropriate for imparting momentum kicks on the atom; we therefore propose the use of a *moving* near-field RF field to achieve the desired length scales.

In this section, we introduce light-less Raman coupling using radio-frequency (RF) magnetic fields from an atom-chip. As we showed in Sec. 2.3, the atom-light

interaction looks like a rapidly varying effective magnetic field (vector light-shifts) where

$$\mathbf{B_{eff}} \propto \mathbf{e_z} \cos(\delta\mathbf{k} \cdot \mathbf{x} - \delta\omega t). \tag{2.10}$$

To eliminate lasers and use radio-frequency (RF) magnetic fields to Raman couple the Zeeman split ground hyperfine states $|F = 1, m_F = -1, 0\rangle$ of ^{87}Rb, we will use an atom-chip in place of Raman beams to eliminate spontaneous emission and spatial constraints that arise with use of complicated laser beam set-ups. The RF will couple the spin states in the usual way, as shown in Fig. 2.5. The strong near-fields of the atom-chip will replace the laser-atom interaction [6]. The coupling field produced by the chip must carry momentum (as in the Raman-with-light case) to couple the hyperfine states. We will accomplish this using a set of semi-rectangular gold wires spaced $a \approx 900$ nm apart on an atom-chip. The wire separation is etched with ion milling. This results in the separation between the wires to taper from ≈ 150 nm at the top, down to ≈ 50 nm at the bottom (see Fig. 2.6). The wires carry currents

$$I_m = I_0 \sin(qx - \omega t + \phi_m), \tag{2.11}$$

where m is the wire number, q is the wave vector, and ϕ_m is the phase. A three-phase current scheme creates a moving magnetic lattice, and the speed of the motion is determined by the frequency of the changing current in the "Raman wires." The currents of neighboring wires are shifted in phase by $2\pi/3$ to produce the moving magnetic lattice.

The proposed atom-chip must be placed in-vacuum because we require chip-

to-BEC distance of $\approx 5\mu$m (Fig. 2.6), a distance which is within the "sweet spot" region for both a strong *and* spatially uniform (along $\mathbf{e}_x$) Raman coupling strength. The chip design considerations are further discussed in Sec. 2.6.3.

The chips are fabricated at the Center for Nanoscale Science and Technology (CNST) at NIST Gaithersburg using electronic beam lithography, and the gold wires were written on a commercially purchased Si substrate. A thin ≈ 5 nm layer of titanium was deposited on the Si to bond to gold. Each Raman wire has a cross-section of 150 nm (height) by 850 nm (width), with a spacing ≈ 150 nm between individual wires at the surface. Due to fabrication constraints, the spacing between wires tapers down from 150 nm to 50 nm at the base. The first test chip is pictured in Fig. 2.7. To ensure uniform coupling over the entire length of a BEC, 96 parallel wires were fabricated. Three distinct regions of wires were fabricated with different wire periodicities. This added flexibility will allow the light-less Raman scheme to be realized with three different characteristic length scales.

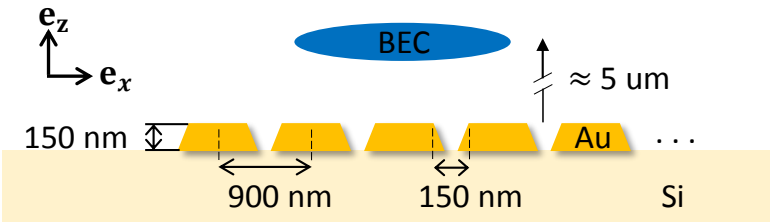

Figure 2.6: To achieve sufficient Raman coupling strengths, the BEC must be $\approx 5\mu$m from the chip surface (i.e. within the evanescent region of the moving RF magnetic field produced by the chip). Adjacent wires are spaced ≈ 900 nm apart, and the separation between wires varies between ≈ 150 nm (top) to ≈ 50 nm (bottom). The separation taper is a consequence of the ion milling technique used to etch the wires during fabrication. The near-field wavelength of the three-phase RF field is then 2.7μm.

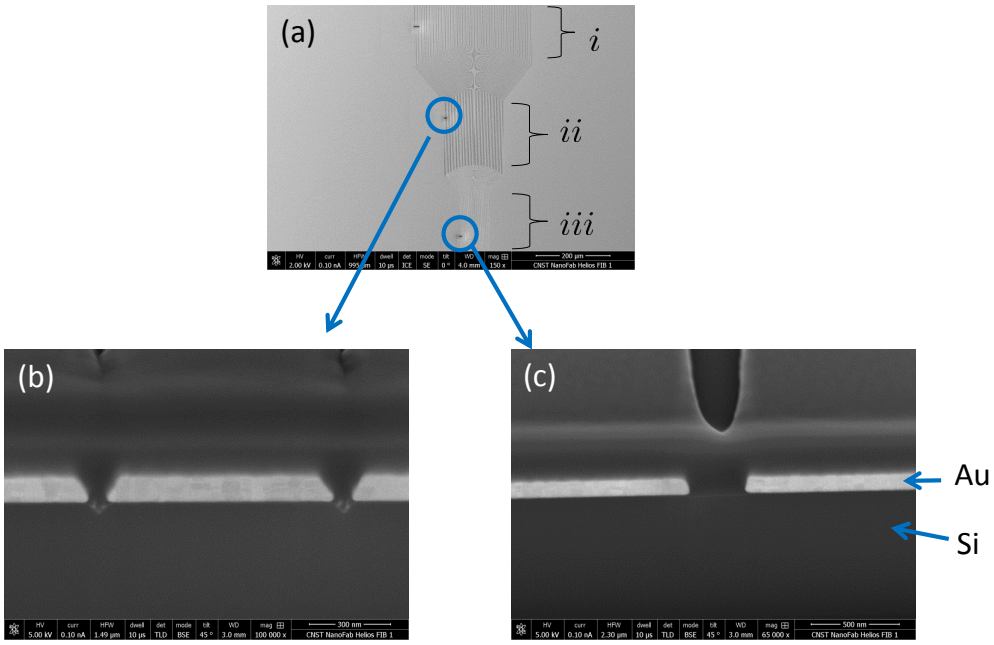

Figure 2.7: First successful test chip fabricated, ready for bench testing. (a) Full top-down view of the 96 wires. There are three regions of parallel wires; each region has different wire periodicity. (b) cross-section view of region *ii*, and (c) cross-section view of region *iii*.

2.6.3 Raman-with-light vs. rf Raman

In general, the rf Raman coupling will take place at different length scales from the Raman-with-light case (although the angle of intersection of optical beams can be used to tune the length scale of the interactions much as in an optical lattice [24]). The different wire spacings are inversely proportional to the momentum that the chip-generated near-field magnetic field will be able to impart to the atoms. The near field magnetic field from the wires is,

$$B(z) \propto I_m \exp(-2\pi z/\lambda_{rf}) \tag{2.12}$$

for Raman wires, where λ_{rf} is the periodicity of the current in the Raman wires, and z is the distance from the chip surface. The strength of $B(z)$ (analogous to the Raman laser intensity in the Raman-with-light case) determines the Raman coupling strength. To overcome the exponential decay of the evanescent wave near the chip surface, we must trap the atoms at a distance of order λ_{rf} from the chip surface. Given the current design, a uniform coupling strength in the plane parallel to the chip surface requires a distance of 3$\sim$5 μm from the surface. A plot of the Raman coupling strength as a function of $\mathbf{e}_x$ for the distance $z = 2\,\mu$m from the chip surface is shown in Fig. 2.8(a). The dark blue curve represents the time-averaged coupling strength, uniform over the dimensions of a typical BEC. For sufficient coupling strengths, we would like to place the BEC as close as possible to the parallel wires producing the moving magnetic field. However, for distances $z < a$, the time-averaged coupling oscillates at the wire periodicity. At distances $z \gtrsim a$, the coupling becomes uniform; therefore the optimal operating region for our experiments is at small distances z that satisfy the uniformity condition. Additionally, the Raman coupling strength as a function of the distance z from the chip surface is shown in Fig. 2.8(b), for the three wire periodicities fabricated on the atom-chip: $\lambda_{eff} = 5.4\,\mu$m, $10.8\,\mu$m, and $16.2\,\mu$m. Further, uniform coupling in the direction perpendicular to the surface requires that the BEC be thin along this direction.

Although atom-chips are commonly purposed for BEC production (such as magnetic trapping with wires on the chip), we will use our chip solely for the purpose of creating the Raman coupling (degeneracy will be reached in an optical trap). Moreover, due to the unusually close placement of the BEC to the chip surface,

near-surface effects such as spin-flips due to thermally induced currents in the room temperature gold surface (Johnson noise), and perhaps even the distortion of the trapping potential due to the Casimir-Polder potential [25], should be considered. A shorter BEC lifetime would limit the duration of time we have to perform experiments. However, since the BEC will be tightly confined along $\mathbf{e}_z$ (2D BEC) and the Casimir-Polder force falls off quickly with distance z from the surface ($\propto 1/z^4$), we expect the Casimir-Polder force to have negligible affects. In addition, the spin-flip rate due to Johnson noise from the gold wires is expected to be insignificant: 0.05 $\text{s}^{-1} \sim 0.15$ s^{-1} in the spatial region of interest to the BEC 3 μm to 5 μm.

For the Raman beams we use wavelength $\lambda \approx 800$ nm, so the relevant energy scale is $E_L = \hbar^2 k_L^2/2m \approx h \cdot 3$ kHz $\approx k_B \cdot 150$ nK. A Raman transition is a two-photon process, while RF Raman using a real moving magnetic field is a single-photon process. Thus, it is appropriate to compare the RF length scales to half of λ, ≈ 400 nm. The length scale for the chip $\lambda_{RF} > 2a$ is limited by the wire spacing $2a \approx 2$ μm. The minimum wire periodicity that could be fabricated on the chip was constrained by the wire cross-section we expected to be necessary to avoid significant heating of the wires. $E_{RF} = h \cdot 20$ Hz $= k_B \cdot 3$ nK, and $-2k_{RF} < \frac{eA}{\hbar} < +2k_{RF}$, the vector potential bounds being a factor of ≈ 8 smaller than the Raman-with-light case. The benefits of the chip method include the relative ease with which complex coupling schemes can be designed, including spatially varying coupling.

If a larger-magnitude artificial vector potential is desired, there are several options to get an E_{RF} comparable to E_L. One option is to use the alkali fermions, which are smaller in mass. For example, ^{6}Li would result in a factor of 10 gain in

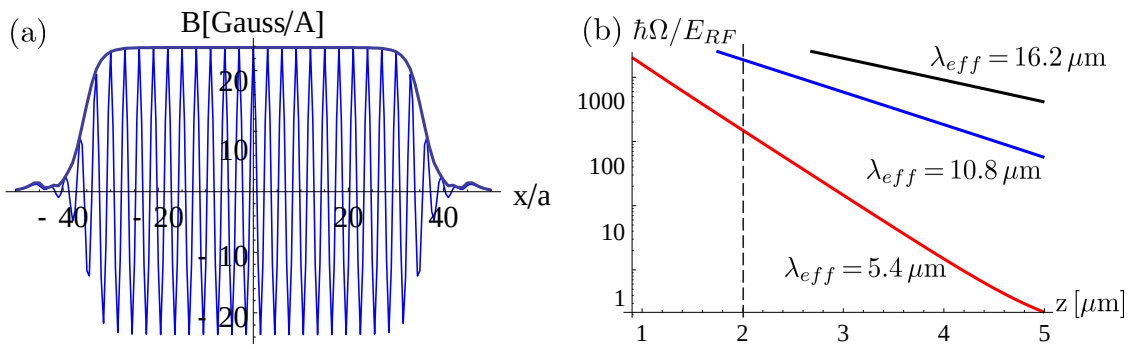

Figure 2.8: A constant coupling over the dimensions of the BEC (as in the light-induced coupling case) requires the time-averaged magnetic field value to be constant. For small distances $z < a$, where a is the spacing between adjacent wires, the coupling oscillates over space. The optimal value is $z = 2a \sim 3a$, the smallest value of z for which the coupling is constant. The calculated time-averaged coupling is shown as dark blue in (a) for $\lambda_{eff} = 5.4\,\mu$m at $z = 2\,\mu$m from the chip surface. We desire the smallest z feasible because the coupling strength drops off exponentially along z. The calculated coupling strength as a function of the distance z away from the chip surface for different wire periodicities is shown in (b) for $I_0 = 1\,$mA.

the recoil energy. Another option is to two-rf-photon couple the $m_f = 1$ and $m_f = -1$ spin states instead of single-rf-photon coupling $m_f = -1, 0$. The momentum difference between the two spin states is then increased by $2k_r$, so that E_r has a factor of 4 gain in energy scale.

As mentioned, the first atom-chip for RF-Raman-coupling induced artificial gauge fields experiments is currently being bench tested. Empirically, we found that we are able to run currents higher than anticipated [26] through the chip wires. This means a larger range of Raman coupling strengths is at our disposal. While the predicted breakdown current was $\approx$ 50 mA, currents up to $\approx$ 130 mA were run through each wire with no noticeable heating of the wires, i.e. the resistance across each wire stayed constant. A current of just $\sim$ 1 mA will provide Raman coupling strength $\hbar\Omega_R \sim E_{RF}$ at distance $z \approx 5$ μm from the chip surface. In

addition, the less stringent constraint on the wire cross-section will allow future chips to be designed with smaller than 900 nm wire periodicities, possibly closing the gap between the length scales of RF Raman and light-induced Raman couplings.

Chapter 3: Quantum degenerate gas production

In our experiment, we achieve Bose-Einstein condensation of ^{87}Rb atoms starting with standard laser cooling techniques followed by evaporation to degeneracy in a hybrid optical dipole plus magnetic trap [7]. Here we provide an overview of the laser cooling and trapping procedure we use on the Rubidium Chip (RbChip) apparatus, which includes the hybrid trap technique developed on the Rubidium II apparatus (now Rubidium Potassium (RbK)), as detailed in Ref. [7]. The steps to degeneracy are summarized in Table 3.1 and Fig. 3.5.

We start by capturing atoms from room-temperature Rb vapor in a six-beam magneto-optical trap (MOT) in the MOT cell with loading enhanced by light-induced atomic desorption (LIAD) [27, 28]. The atoms are then trapped in a magnetic quadrupole trap and magnetically transported [29] from the MOT cell to the science cell using a series of overlapping anti-Helmholtz coil pairs. The details of the magnetic transport are discussed in Sec. 4.3. Upon completion of the transport, we perform rf-forced evaporation in the magnetic trap. The magnetic field gradient is then lowered, so that the magnetic trapping potential no longer exceeds that of gravity, to transfer the cloud into a red-detuned crossed optical dipole trap (ODT). Finally, we perform evaporation in a crossed ODT to reach quantum degeneracy.

3.1 Introduction: Doppler cooling

Our task is to cool room-temperature atoms from vapor, ≈ 300 K, until they reach quantum degeneracy at ≈ 100 nK. The first step is to collect atoms in a MOT using Doppler cooling, which for example is commonly utilized in a Zeeman slower. While the RbK experiment has a Zeeman slower, the RbChip experiment does not. However, we give a brief description of it here for pedagogy. A Zeeman slower utilizes one-dimensional (1D) Doppler cooling in combination with an external, spatially varying magnetic field to cool and slow atoms before they are captured in a MOT. The basic ideas of Doppler cooling can be understood with this 1D example. A beam of atoms traveling along $\mathbf{e}_x$ is slowed by a fixed frequency laser beam propagating along $-\mathbf{e_x}$ (Fig. 3.1). As the atoms slow due to preferential absorption of counter-propagating near resonant radiation, the Doppler shift of their transition frequency decreases. This issue is remedied with the application of a spatially varying magnetic field that changes the Zeeman splitting of the internal spin states of the atoms as they move and slow so that the atoms stay on resonance with the laser beam frequency.

A photon absorbed imparts momentum $\hbar k_L$ to an atom at resonance with its laser frequency ω_L, where $k_L = 2\pi/\lambda_L$ is the wave number of the plane-wave laser with free-space wavelength λ_L (Fig. 3.1). For an atom moving at speed v in the direction opposite to the laser beam propagation, the atomic resonance frequency ω_0 in the laboratory frame is Doppler shifted by $k_L v$ in the reference frame of the atom, so that the atom is resonant with a laser which has angular frequency $\omega = \omega_0 - k_L v$. The laser cooling beam must then have frequency ω_L that is red-detuned from ω_0

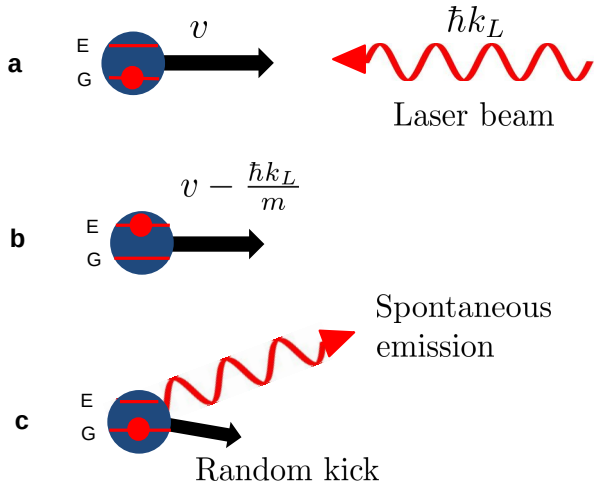

Figure 3.1: Doppler cooling. (a) An atom travels along $\mathbf{e_x}$ with velocity v, opposite the propagation direction of a laser beam with momentum $\hbar k$. (b) An atom absorbs light resonant with its internal electronic states, including both Doppler and Zeeman shifts. The atom is excited to its excited state, and the light imparts momentum $\hbar k$ on the atom. (c) The spontaneous emission decay of the atom back to its ground electronic state produces a random momentum kick which averages to net zero over many cycles.

to be absorbed by the atom: $\omega_L = \omega_0 + \delta$, where detuning $\delta < 0$. The absorbed photon is then spontaneously emitted in a random direction (Fig. 3.1c). Over the course of many absorption-emission cycles from an incident laser beam, the random momentum kicks average to zero and the net momentum kick is directed opposite to v (Fig. 3.1b): the atom is slowed.

To achieve significant cooling, many cycles of absorption and spontaneous emission are necessary. The recoil velocity $v_r = \hbar k_L/m \approx 6$ mm/s for ^{87}Rb, where m the mass of a single rubidium atom, is the change in the atom's velocity due to absorption of a photon. At room temperature (300 K), the most probably velocity of ^{87}Rb atoms is $\approx$ 240 m/s, so that tens of thousands of momentum kicks are

necessary to significantly slow the atoms. To accomplish this task, we couple the $|5S_{1/2}; F = 2\rangle$ ground to the $|5P_{3/2}; F' = 3\rangle$ excited state (the D_2 cycling transition) using $\lambda \approx 780$ nm laser light.

The internal electronic states used to Doppler cool neutral ^{87}Rb atoms are shown in Fig. 3.2. The atomic cooling transition used in laser cooling and trapping is the cycling transition accessed using σ (circularly) polarized cooling beams. This D_2 transition is the optimal cooling transition because it has the largest transition probability (i.e. largest Clebsch-Gordan coefficient). In addition, angular momentum selection rules require an atom in $|5P_{3/2}; F' = 3, m'_F = 3\rangle$ to spontaneously decay back down to $|5S_{1/2}; F = 2, m_F = 2\rangle$, where the atom rejoins the cooling cycle. In addition to the cooling transition, atoms have a small but finite probability of making the off-resonant transition several linewidths away from the cooling transition, $|5S_{1/2}; F = 2\rangle \rightarrow |5P_{3/2}; F' = 2\rangle$. The atom may then spontaneously emit back to $|5S_{1/2}; F = 2\rangle$ or to the dark $|5S_{1/2}; F = 1\rangle$ state. Atoms in the dark state are no longer at resonance with the laser beam due to the large ($\gg \Gamma$) 6.8 GHz splitting between the two electronic ground states. We, therefore, apply an additional repump laser beam resonant with the $|5S_{1/2}; F = 1, m_F = 1\rangle \rightarrow |5P_{3/2}; F' = 2, m'_F = 2\rangle$ transition to pump the atoms out of the dark state (Fig. 3.2). Some of these atoms will decay to $|5S_{1/2}; F = 2\rangle$ and rejoin the cooling cycle.

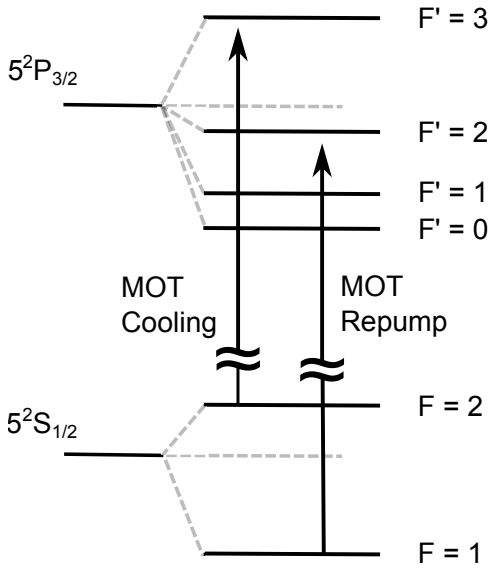

Figure 3.2: ^{87}Rb D2 line hyperfine structure level diagram. The primed states represent the excited state hyperfine structure. The MOT cooling and repump laser wavelengths are red-detuned from the $F = 2$ to $F' = 3$ and $F = 1$ to $F' = 2$ transitions, respectively. The detuning compensates for the Doppler shift seen by the atom traveling in the direction opposite the laser beam propagation.

3.2 Limits of Doppler cooling

The maximum scattering force from the absorption process is limited by the rate of spontaneous emission (an atom cannot absorb faster than it can emit a photon). The steady-state excited state population for a two-level atom is

$$\rho_{22} = \frac{\Omega^2/4}{\delta^2 + \Omega^2/2 + \Gamma^2/4}. \tag{3.1}$$

The laser intensity I and coupling strength Ω (the Rabi frequency, the rate at which the atom oscillates between the ground and excited states) are related by $I/I_{SAT} = 2\Omega^2/\Gamma^2$ where the saturation intensity for the cooling transition is $I_{SAT} = \hbar\omega^3\Gamma/12\pi c^2$, where ω is the frequency of the transition, and c is the speed of light. For large laser intensities $I \to \infty$, $\Omega \gg \delta, \Gamma$, so that $\rho \to 1/2$. Then the scattering

force $F = \hbar k \Gamma \rho_{22}$ has a maximum $F_{max} = \hbar k \Gamma / 2$. The maximum acceleration is then $a_{max} = F_{max}/m = \hbar k \Gamma / 2m = v_r / 2\tau$, where τ is the lifetime of the $5P_{3/2}$ excited state. For ^{87}Rb, $a_{max} \approx 2 \times 10^5 \mathrm{m/s}^2$, $v_r \approx 6$ mm/s, and $\tau \approx 26$ ns. For two counter-propagating laser beams, the net cooling scattering force slows the atoms so that they can only slowly diffuse out of the beams: an optical molasses. This force is a damping force $F_{molasses,cool} = -\alpha v$, for small velocities $kv \ll \Gamma$, and negative (red) detuning $\delta < 0$. The damping coefficient α is a function of δ, and $\alpha > 0$ only when the laser is red-detuned from atomic resonance. This damping force competes with momentum diffusion from spontaneous scattering to a lowest Doppler limited temperature T_D, limited by the natural line-width Γ of the excited state by the relation $k_B T_D = \hbar \Gamma / 2$. For ^{87}Rb, the Doppler temperature is $T_D \approx 146\,\mu$K.

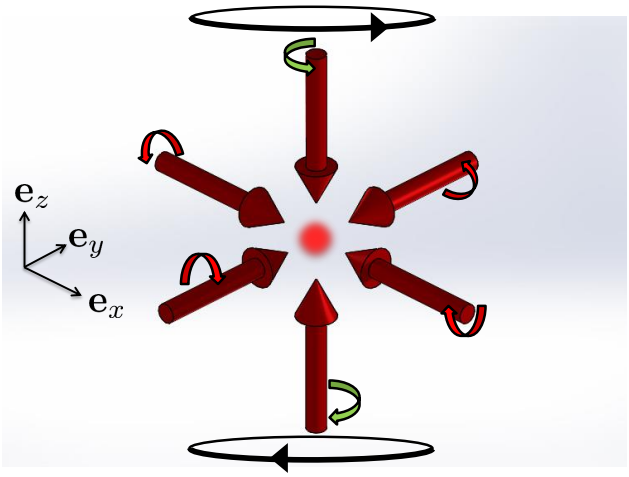

Figure 3.3: Magneto-optical trap. Three properly polarized counter-propagating pairs of orthogonal laser beams along with an external anti-Helmholtz magnetic field make a magneto-optical trap (MOT).

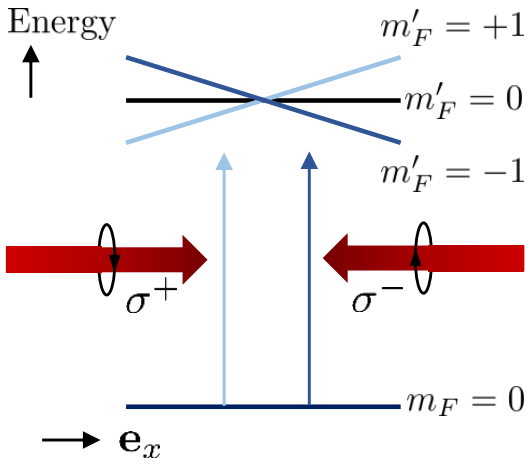

Figure 3.4: MOT energy level separation as a function of position. Note that the $\sigma^+(\sigma^-)$ beams couple to opposite $m_f = 1(-1)$ Zeeman states.

3.3 Magneto-optical trap

Our procedures for Bose-Einstein condensate (BEC) production all start by loading atoms into a magneto-optical trap (MOT), as shown in Fig. 3.5 stages (i) to (ii). The MOT is typically used as a first step toward BEC because of its large capture volume, reasonable capture velocity, and the fairly long lifetime of the trapped atoms. The MOT combines three orthogonal pairs of counter-propagating laser beams with a weak magnetic field gradient (weak compared to the gravity gradient, such that the atoms are not magnetically trapped) of ≈ 10 G/cm to form a trapping region [30]. The field gradient is created by a pair of anti-Helmholtz coils that run currents in opposite directions with a field minimum of zero at the trap center (Fig. 3.3). The polarizations of the laser beams play a crucial role in a MOT (Fig. 3.4). Near the quadrupole trap center, the field varies linearly as $\mathbf{B} = B'(x, y, -2z)$. Since the magnetic field is symmetric along $\mathbf{e}_x$ and $\mathbf{e}_y$, the gradients along $\mathbf{e}_x$ and $\mathbf{e}_y$ are equal, and because $\nabla \cdot \mathbf{B} = 0$, $(\partial B_x/\partial x) + (\partial B_y/\partial y) - (\partial B_z/\partial z) = 0$. The weak fields provide a Zeeman splitting $\Delta E = g_F \mu_B m_F B$ of the atom's internal energy levels near the trap minimum. Each counter-propagating laser beam pair has opposite circular polarizations—right-handed circular (σ^+) and left-handed circular (σ^-) that allow angular momentum transitions $\Delta m_F = +1$, and $\Delta m_F = -1$, respectively (Fig. 3.4). As an atom travels away from the MOT trap center, its internal hyperfine level splitting increases with the field. An atom that sees a red-detuned beam will feel a restoring force when its internal energy reaches a point in space where it is at resonance with the laser

frequency. The laser is detuned of order the natural linewidth ($\Gamma/2\pi \approx 6$ MHz) of the transition.

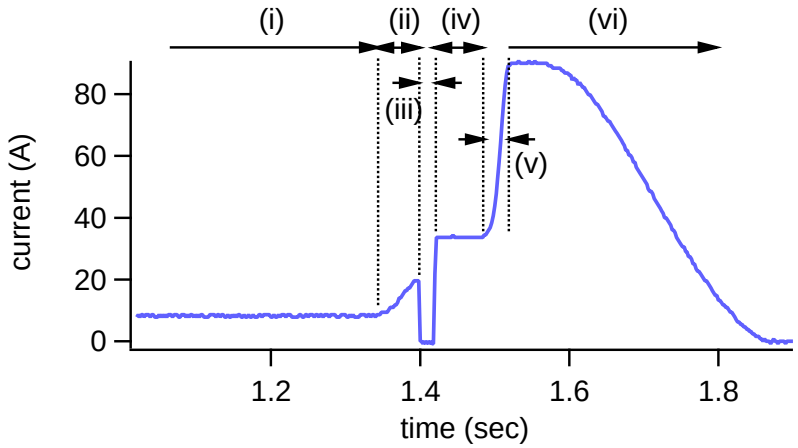

Figure 3.5: Quadrupole trap current as a function of time. The anti-Helmholtz coil pair used for the first stages of laser cooling and magnetic trapping is sequenced as follows: (i) Vaporous ^{87}Rb atoms are captured and cooled in the magneto-optical trap (MOT) for $\sim$1 sec. The loading of the MOT happens in the first $\sim$0.5 sec using light-induced atomic desorption (LIAD). (ii) CMOT. (iii) The magnetic field is turned-off for the molasses stage. (iv) Magnetic trap is on to recapture the atoms (MOT laser off). (v) Adiabatic increase in the trap depth for a compressed trap to get ready for magnetic transport. (vi) Magnetic transport starts, to be discussed in detail in Sec. 4.3.

Typically, the number of atoms captured in a MOT is $N \approx 10^9$, with temperature $T \approx 100\,\mu$K. We typically load the MOT for 0.5 s to 3.0 s depending on background vapor pressure and desired number of atoms into the science cell.

3.4 Optical molasses

After the atoms are trapped and cooled in the MOT, we perform polarization gradient cooling by suddenly turning the quadrupole field to zero, while keeping the laser beam pairs used for the MOT on. The three orthogonal pairs of counter-propagating laser beams provide the damping forces necessary to cool atoms in a sub-

Doppler optical molasses [31]. Molasses is performed for a short period (step (iii) in Fig. 3.5) immediately after the MOT stage. Since atoms move in three-dimensions, the optical molasses laser beams must propagate along all three axes for capture. It is important to note that the molasses itself is not a trap, and does not spatially confine the atoms.

Optical molasses uses the polarizations associated with laser beams to sub-Doppler cool atoms. While Doppler cooling is limited by the excited state line width of the atom $\approx$ 6MHz for ^{87}Rb, the Sisyphus cooling mechanism of molasses is limited by the recoil energy $E_r/h \approx 4$ kHz of the atom, meaning that the change in energy per a Doppler cooling process is larger than that in the Sisyphus effect. Each set of counter-propagating beams create a spatially varying light-shift. An atom that repeatedly climbs up this gradient, absorbs a photon, then spontaneously decays to the bottom of the hill, experiences a decrease in energy related to the height of the hill for each occurrence. The process is ultimately limited by the recoil energy gained from spontaneous emission. In the alkali atoms, Sisyphus cooling operates at energies below the Doppler cooling limit, and can further cool atoms below the Doppler limit. Our apparatus utilizes a 19 ms molasses stage (Fig. 3.5 (iii)).

3.5 Magnetic trap

After laser cooling atoms in a MOT, then molasses, the atoms are transferred to a magnetic trap [32] for transport and evaporative cooling [33]. In the magnetic

Table 3.1:

MOT quadrupole coil current sequence					
		time	current (A)	ramp type	frequency ($\Gamma/2$)
1	LIAD MOT	0.5 s to 3 s	8.5	constant	2.6
2–3	MOT /CMOT	1.0 s	$8.5, 20$	half Gaussian	$2.5, 2.7$
4	molasses	19 ms	to $I = 0$	exponential	23.2
5	optical pumping	681 μs			10.6
6	magnetic trap	0.1 s	34	constant	
7	magnetic trap compress	0.1 s	34,90	half Gaussian	
8	magnetic transport	2.2 s	Sec. 4		
9	rf evaporation	5 s		linear	20-4 MHz
10	decompression i	4 s	$70, 50$	linear	
11	decompression ii	3 s	$50, 22$	linear	

capture stage shown in Fig. 3.5(iv), the quadrupole current is suddenly turned back on. Magnetic traps have large trap volumes that allow good spatial mode-matching to the size of the laser cooled atomic cloud. This, in addition to the simplicity in design (the same pair of quadrupole coils used for the MOT are used for magnetic trapping in an experiment) and the tight confinement the trap can provide (much larger than gravity gradient), explains its wide usage.

The magnetic trap provides a state-dependent conservative potential using gradient forces to keep the atoms near the quadrupole center. These forces arise from the interaction between the atomic magnetic dipole moment and the external magnetic field $\mathbf{B}$. The potential energy experienced by an atom is $U = -\boldsymbol{\mu} \cdot \mathbf{B} = g_F \mu_B m_F B$. The field from the quadrupole trap is linear near the trap center. For circular coils it has the form;

$$U(\mathbf{r}) = \mu B' \sqrt{x^2 + y^2 + 4z^2}, \tag{3.2}$$

where B' is the magnetic field gradient in the $\mathbf{e_x} - \mathbf{e_y}$ plane; half the gradient along $\mathbf{e_z}$. Then the force experienced by an atom due to $U(\mathbf{r})$ is

$$\mathbf{F} = -\nabla U = -g_F \mu_B m_F \left(\frac{\partial B}{\partial x}, \frac{\partial B}{\partial y}, \frac{\partial B}{\partial z} \right), \tag{3.3}$$

so that the linear potential is trapping when the force points in the weak field direction, towards the center of the trap. This requires $g_F m_F > 0$, and the atoms that satisfy this condition are called low-field seekers—$|F = 1, m_F = -1\rangle$, $|F = 2, m_F = +1\rangle$, $|F = 2, m_F = 2\rangle$ states for ^{87}Rb—while high-field seekers $|F = 1, m_F = +1\rangle$, $|F = 2, m_F = -1\rangle$, $|F = 2, m_F = -2\rangle$ get expelled from the trapping region. Spin-projectionless atoms in the $|F = 1, m_F = 0\rangle$ and $|F = 2, m_F = 0\rangle$ states do not experience any magnetic force at linear order in B.

3.5.1 RF evaporation

After the atoms have been recaptured using the magnetic trap, they are ready to be cooled further via evaporation. The field gradients in a magnetic trap provide a spatially dependent resonance that can be driven by radio-frequency (RF) to spatially select out the most energetic atoms. These atoms are found furthest away from the center of the trap, and are forced to spin-flip from a low-field seeking state to a high-field seeking state by application of RF with frequency ω_{rf} such that $\hbar\omega_{rf} = g_F \mu_B m_F B$ (Fig. 3.6) drives resonant transitions from the $m_F = -1$ state to the untrappable $m_F = 0, +1$ states. The most energetic atoms, i.e., atoms with energies larger than the average energy are selected out, and the remaining atoms elastically scatter and re-thermalize to a lower average temperature.

However, there is one inherent limitation to the quadrupole magnetic trap: the magnetic field zero at the center of the trap causes unwanted Majorana spin-flips and heating, which limits evaporative cooling to temperatures above those required for quantum degeneracy. Evaporation works well as long as the re-thermalization from elastic collisions happens at a rate faster than the non-adiabatic spin-flip rate. As evaporation cools the atoms and the cloud size decreases, the atoms eventually heat and spin-flip faster than they can re-thermalize. Thermalization from elastic collisions happens at a rate faster than the non-adiabatic spin-flip rate.

Two conventional methods commonly used to overcome this disadvantage in quadrupole traps are the time orbiting potential (TOP) trap, and an optical plug. The TOP trap uses a time orbiting bias field to shift the magnetic field zero away from the trap center, while the optical plug method uses a repulsive (blue-detuned) optical potential to push the atoms away from the center. In Ref. [34], we developed a new hybrid technique which combines the magnetic trap with a red-detuned optical dipole trap to achieve degeneracy of ^{87}Rb atoms. This technique does not require an oscillating field or a plug beam. This method is discussed in Sec. 3.6.

In practice, we apply an RF sweep to continuously eject the most energetic atoms out of the trap until the desired equilibrium temperature is reached (Fig. 3.6). In terms of the RF dressed state energy bands of the coupled magnetic sublevels of the $F = 1$ ground hyperfine state shown in Fig. 3.7, a linear RF sweep follows the lowest energy band (shown in solid red). At the end of a sweep, we typically have $N \approx 10^8$, and $T \approx 30\,\mu$K.

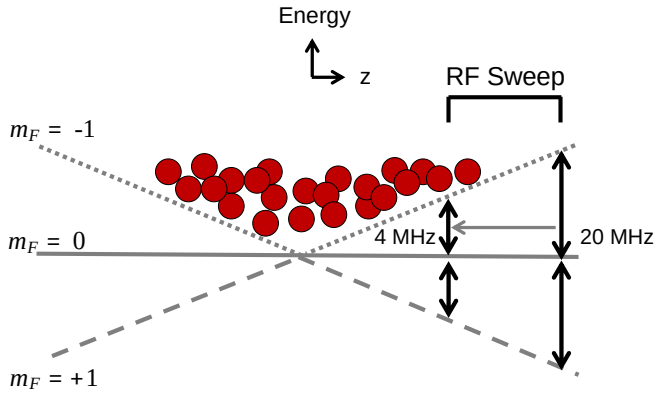

Figure 3.6: Atoms in the magnetic trap are evaporatively cooled with a radio-frequency (RF) sweep (indicated by the gray arrow) from 20 MHz to 4 MHz. The atoms with the highest energies become resonant with the RF transition frequency during the sweep. When resonant, the RF flips the internal state of an atom from the magnetically trappable $m_F = $-1 state to the untrappable $m_F = 0,1$ states. The spin-flipped atoms are evacuated from the trap, and the remaining atoms re-thermalize to a lower temperature.

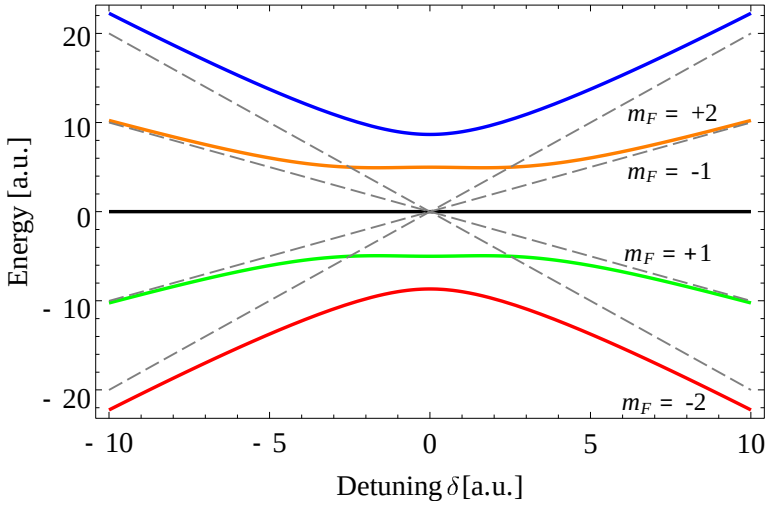

Figure 3.7: The RF dressed energy levels for the ground $F = 2$ manifold are depicted by the solid curves, with the lowest energy band shown in red. The energies of the magnetic sublevels sans dressing are shown as dashed gray lines.

3.6 Quadrupole plus optical dipole: the hybrid trap

As atoms cool and collect in the middle of the magnetic trap during RF evaporation, spin-flips may occur near the Zeeman level crossings (Fig. 3.6). This draw-

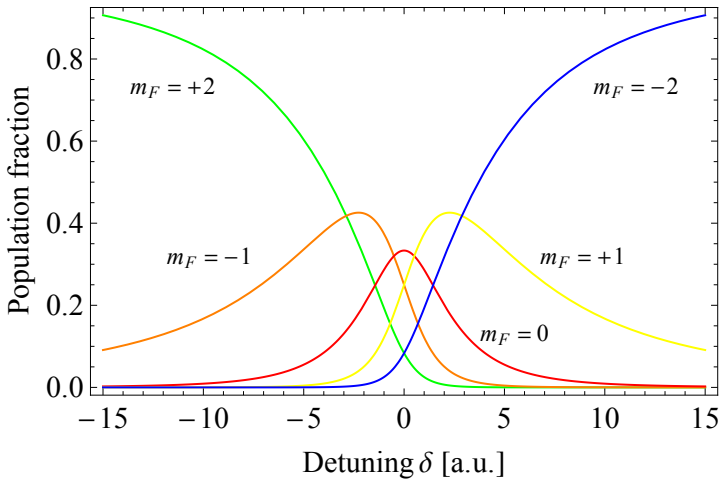

Figure 3.8: Spin populations of the RF dressed spin states in the $F = 2$ ground hyperfine state manifold as a function of the detuning, δ, from RF resonance.

back of the quadrupole magnetic trap must be mitigated. In our hybrid scheme, we minimize spin-flip loss by overlapping an optical dipole trap with the magnetic trap. The initially magnetically trapped atoms are collected in a red-detuned optical dipole trap centered $\approx$ one beam waist below the magnetic quadrupole zero (The alignment below the quadrupole zero is such that the magnetic field gradient supports the atoms against gravity). After RF evaporation, when Majorana loss is significant, atoms remain in the all optical trap.

The hybrid trap works well because it limits Majorana loss in the magnetic trap, and the transfer of the atomic cloud from linear quadrupole to harmonic dipole happens at approximately constant entropy; i.e. the transfer is adiabatic. The transfer process both decreases the temperature and increases the phase space density. For a cloud in thermal equilibrium in a quadratic trap, the Majorana loss rate $\Gamma_m \propto \hbar/ml^2$, where m is the mass of the atom, and l is the half width half maximum of the cloud [7, 35]. This assumption is valid for high density clouds with

high rates of elastic collision [36].

For a two-level system, the single beam ODT potential is

$$U(\mathbf{r}) = -\frac{-3\pi c^2 \Gamma}{2\omega_{12}^3}\left(\frac{1}{\omega_{12}+\omega}+\frac{1}{\omega_{12}-\omega}\right) I(\mathbf{r}), \tag{3.4}$$

where c is the speed of light, Γ is the spontaneous decay rate of the excited state, ω_{12} is the resonant frequency, and ω, $I(\mathbf{r})$ are the frequency and intensity of the dipole laser beam, respectively. We define detuning $\Delta = \omega - \omega_{12}$. For a near-detuned beam $|\Delta| = |\omega - \omega_{12}| \ll \omega_{12}$, the trapping potential simplifies to

$$U(\mathbf{r}) = -\frac{3\pi c^2}{2\omega_{12}^3}\frac{\Gamma}{\Delta} I(\mathbf{r}). \tag{3.5}$$

For a red-detuned beam $\Delta < 0$, $U(\mathbf{r})$ is an attractive potential with a potential minimum at maximum intensity. This remains true for a far-red detuned trap, for which both terms in Eqn. 3.4 must be considered. In the laboratory we use a far-red detuned trap at high intensities to decrease the scattering rate. The trapping potential for such a trap using a Gaussian laser beam is

$$U(\mathbf{r}) = -U_0 \exp\{-2r^2/{\omega_0}^2\} \tag{3.6}$$

where r is the radial distance from the center of the beam, and ω_0 is the beam waist ($1/e^2$ radius).

The combined optical and magnetic potential of the hybrid trap is

$$U(\mathbf{r}) = \mu B' \sqrt{\frac{x^2}{4}+\frac{y^2}{4}+z^2} - U_0 \exp\{-2[x^2+(z-z_0)^2]/w_0^2\} + mgz + E_0, \tag{3.7}$$

where the first term originates from the magnetic trap as discussed, and the second term comes from the Gaussian dipole beam with width w_0 and trap depth U_0. The

third term is the gravitational potential energy of the atom with mass m, and E_0 is an offset added to make the potential energy minimum $U_{\min} = 0$.

We use three pairs of quadrupole coils to provide bias magnetic fields in the $\mathbf{e}_x$, $\mathbf{e}_y$, and $\mathbf{e}_z$ directions. The bias coils serve several functions. These include the cancellation of stray background magnetic fields; defining the quantization axis; and inducing the Zeeman shift on the hyperfine energy levels of the atoms necessary for microwave or RF internal state control. Figure 3.9 shows the magnetic field calibration of the three coils. The coils were designed to provide a field larger than or equal to 1 G/A. The intercept is the calibrated current required by a bias coil pair to cancel out the background magnetic field (i.e. the condition under which the atoms experience zero magnetic field).

Optical forces arising from scalar light-shift in the optical trap confine atoms to the highest intensity region for a far red-detuned laser beam. After complete transfer into the crossed ODT, atoms typically have $N \approx 10^7$, and $T \approx 5\,\mu$K. The dipole trap is approximately harmonic at low energies, and is state-independent (due to large detuning).

In the hybrid trap, we use the strengths of both the magnetic trap (large trap volume and tight confinement) and ODT (efficient all-optical evaporation without magnetic fields), while overcoming their weaknesses by using the two traps together. At low energy, $U(\mathbf{r})$ may be approximated as harmonic:

$$U(\mathbf{r}) \approx \frac{1}{2}[U_x'' x^2 + U_y'' y^2 + U_z''(z - z_{min})^2], \tag{3.8}$$

where U_i'' with $i = x, y, z$ are the trap curvatures, and $\omega_{x,z} \approx 2\sqrt{U/m\omega_0^2}$.

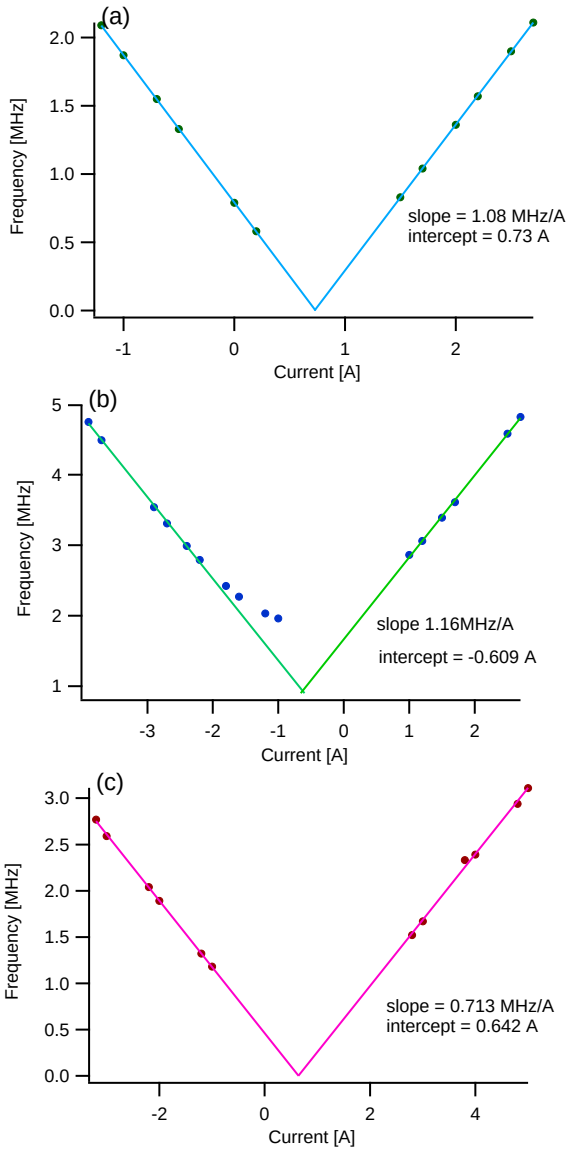

Figure 3.9: Calibration of the bias coils in the science cell along (a) $\mathbf{e}_x$, (b) $\mathbf{e}_y$, and (c) $\mathbf{e}_z$.

After a final adiabatic relaxation of the magnetic trap, the atoms are confined solely in a crossed optical dipole trap. The crossed-dipole trap frequencies along $\mathbf{e}_x$,$\mathbf{e}_y$, and $\mathbf{e}_z$ as a function of the total laser output intensity, as measured by a pick-off photodiode, is shown in Fig. 3.10(a). The trap frequencies were measured by exciting dipole modes of oscillation in the trap and observing the resulting oscillation in the center of mass motion. The measurements were taken by using a

magnetic field gradient to apply a force $F_i = g_F \mu_B m_F (\partial B / \partial x_i)$ on the atoms. The gradient force displaces the $|F = 2, m_f = 2\rangle$ atoms from the center of the harmonic trap; thereby initiating oscillation about the trap minimum. The post time-of-flight position of the atomic cloud as a function of time was measured to determine the trap frequency along each axis. An example measurement is shown in Fig. 3.10(b). After transfer, we perform an all-optical evaporation in the dipole trap by lowering the laser intensity and therefore the depth of the trap. At the end of evaporation, degeneracy is reached.

3.7 A dimensional argument for Bose-Einstein Condensation

Classically, a particle may occupy any point in the phase-space continuum (p_x, p_y, p_z, x, y, z). When considering quantum statistics, however, the three-dimensional phase-space is discrete. The requirement for discreteness arises from the Heisenberg uncertainty principal $\Delta p \Delta x \geq \hbar/2$, so that the smallest allowed volume unit in three-dimensional phase-space is h^3. Up to a constant, the critical number density N_c/V for Bose-Einstein Condensation (BEC) can be derived as follows: consider a bosonic gas with volume V and temperature T, and assume that all states with energies $k_B T$ and below are occupied. The equipartition theorem, $k_B T = p_{max}^2/2m$ (where k_B is the Boltzmann constant) relates T to the maximum momentum p_{max}. Then the total phase-space volume $\mathcal{V} = V \cdot 4\pi p_{max}^3/3$, and the total number of quantum states $\mathcal{N} = \mathcal{V}/h^3$. Degeneracy occurs as the number of quantum states

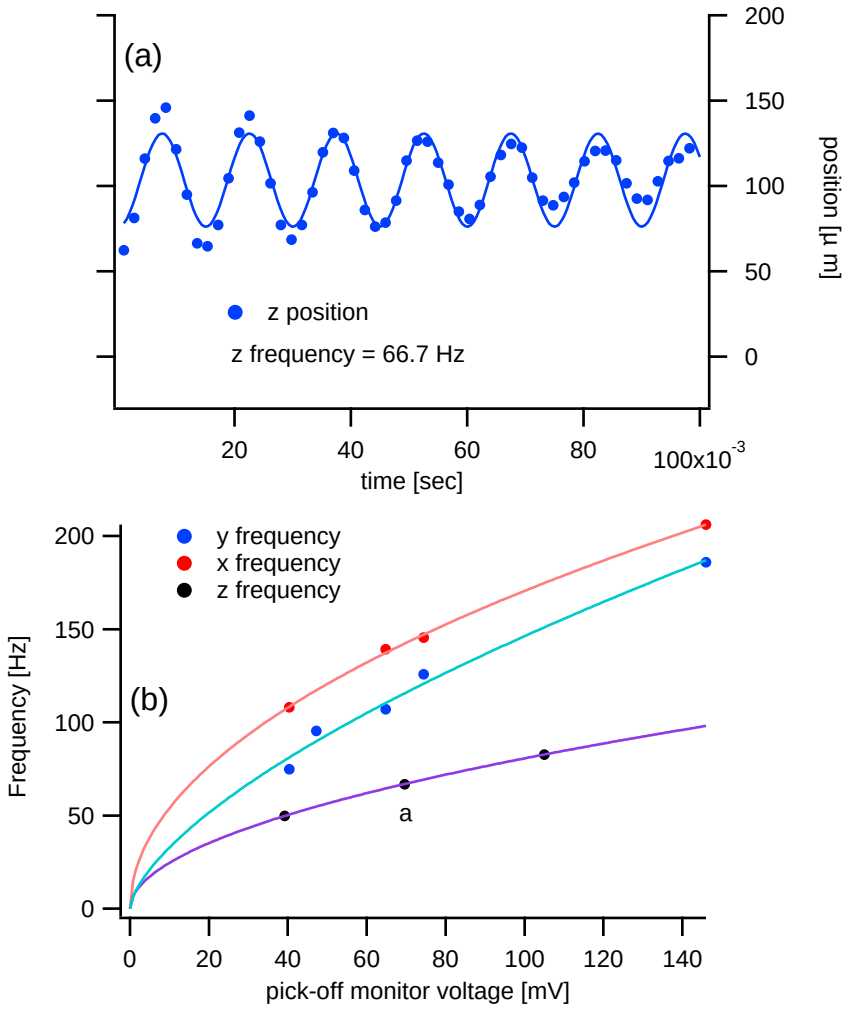

Figure 3.10: Calibration of the crossed-dipole trap frequencies as a function of the total laser intensity. (a) An example trap frequency measurement along $\mathbf{e}_z$, shown as point "a" in (b). (b) The trap frequencies as a function of intensity (trap depth) have a square root dependence, characteristic of a harmonic oscillator. Measurements were taken while keeping the power ratio between the two beams constant.

approaches the total number of particles N. Then for critical number $N_c\mathcal{N}$, we find

$$\frac{N_c}{V} \propto \left(\frac{mk_BT_c}{2\pi\hbar^2}\right)^{\frac{3}{2}}, \tag{3.9}$$

where T_c is the critical temperature. We have found the relation between N_c and T_c, up to a constant, using dimensional analysis. Next we apply quantum statistics to derive the proportionality constant.

3.8 Quantum Statistics

To refine our previous estimate, we first introduce the differences between Boltzmann statistics and quantum statistics for bosons and fermions. To begin, the probability of finding a system in state i with energy E_i and number of particles N_i when the system is in contact with a reservoir with fixed temperature T and chemical potential μ is

$$P_i = \frac{e^{-[E_i - \mu N_i]/k_B T}}{Z}, \tag{3.10}$$

where $Z = \sum_i e^{-[E_i - \mu N_i]/k_B T}$ is the grand partition function which sums over all possible Gibbs factors $e^{-[E_i - \mu N_i]/k_B T}$ so that $\sum_i P_i = 1$ is satisfied.

The Pauli exclusion principle states that no two fermionic particles may occupy the same single-particle state. This means that for a single-state system, the state may either be occupied ($N = 1$) with energy ϵ, or unoccupied ($N = 0$) with energy 0. The partition function for such a system is $Z = 1 + e^{-(\epsilon - \mu)/k_B T}$, and the average number of particles in the single-particle state $\langle n \rangle = \sum_i N_i e^{-[E_i - \mu N_i]/k_B T}/Z$ is given by the Fermi-Dirac distribution

$$\langle n \rangle_{FD} = \frac{1}{e^{(\epsilon - \mu)/k_B T} + 1}. \tag{3.11}$$

With bosons, the single-particle state can be occupied by any number of n particles, so that the sum is a geometric series $Z = \sum_i e^{-(\epsilon - \mu N_i)/k_B T} = 1/(1 - e^{-(\epsilon - \mu)/k_B T})$, where $\mu < \epsilon$ so that the sum converges, and insures that the Bose-Einstein distri-

bution for the average number of particles

$$\langle n \rangle_{BE} = \frac{1}{e^{(\epsilon-\mu)/k_BT} - 1}, \tag{3.12}$$

is always positive. We would like to compare the number distributions of bosons and fermions with that of an ideal gas in which all particles occupy different single-particle states. Such a system is described by the Boltzmann number distribution

$$\langle n \rangle_{Boltzmann} = e^{-(\epsilon-\mu)/k_BT}. \tag{3.13}$$

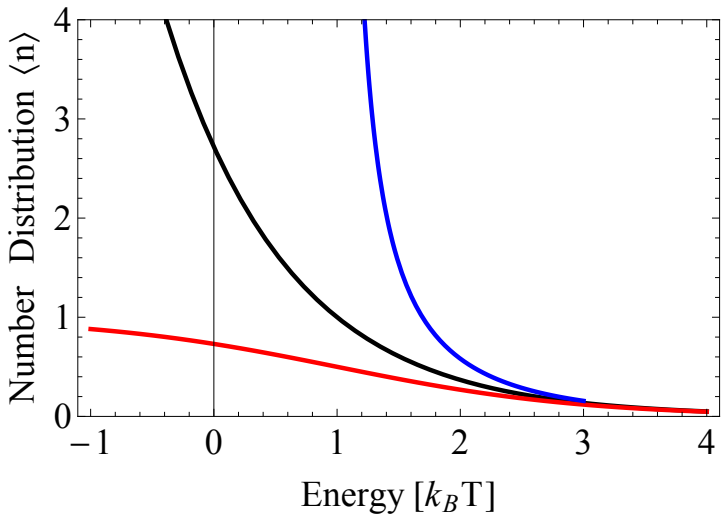

Figure 3.11: Fermi (red), thermal (black), and Bose (blue) number distributions. The energy axis is in units of k_BT, and is offset by the chemical potential μ. The Bose distribution diverges at $\epsilon = \mu$

For $\epsilon \gg \mu$, both quantum distributions approach the classical limit, $\langle n \rangle_{FD}, \langle n \rangle_{BE} \rightarrow \langle n \rangle_{Boltzmann}$, as shown in Fig. 3.11.

The Fermi-Dirac distribution is a step-function when $T = 0$, and all states with energies below μ are occupied, and those above unoccupied. This describes degeneracy for fermions, and $\epsilon_F = \mu$ is the Fermi energy, the energy of the highest

occupied single-particle state. Since degeneracy is reached when every available energy level is filled, starting with the ground state, the total number of atoms present determines the Fermi energy. For a Fermi-gas confined in a box with volume V, $\epsilon_F = h^2/8m(3N/\pi V)^{2/3}$, and $T_F = \epsilon_F/k_B$ is the Fermi temperature.

3.9 Density of states

The critical number of atoms for BEC with the correct pre-factor for an unconfined extended system can be computed using the previously derived Bose-Einstein number distribution and the density of states. We follow the derivation in Pethick and Smith [37] to derive the critical phase-space density required for condensation. A bosonic gas will condense to degeneracy at critical temperature T_c as discussed, and an appreciable number of atoms will occupy the same single-particle ground state. We first re-write the total number of quantum states $\mathcal{N}$ in terms of the energy associated with the free particle momentum $\epsilon = p_{max}^2/2m$ for a particle confined in a box (note: in the laboratory particles are harmonically trapped). The total number of states up to energy ϵ is $G(\epsilon) = V2^{1/2}(m\epsilon)^{3/2}/3\pi^2\hbar^3$. Then the density of states $g(\epsilon) = dG(\epsilon)/d\epsilon = Vm^{3/2}\epsilon^{1/2}/2^{1/2}\pi^2\hbar^3$, which has the form $g(\epsilon) = C_\alpha \epsilon^{\alpha-1}$, with $\alpha = 3/2$ and $C_{3/2} = Vm^{3/2}/2^{1/2}\pi^2\hbar^3$ for a particle in a three-dimensional box. We integrate the density of states weighted by the Bose-Einstein distribution over all energies to find the total number of particles in excited states $N_{excited} = \int_0^\infty d\epsilon g(\epsilon)\langle n\rangle_{BE}$, where the contribution from the ground state is negligi-

ble for large N.

At the critical point before an appreciable number of particles occupy the ground state for condensation, virtually all particles occupy excited states, so that $N = N_{excited}$. The maximum number of particles is in the excited states when $\mu = 0$ (energy required to add a particle to the system is zero):

$$N_c = \int_0^\infty d\epsilon g(\epsilon) \frac{1}{e^{\epsilon/k_B T_c} - 1}. \tag{3.14}$$

Change of variables $x = \epsilon/k_B T_c$ gives

$$N_c = C_\alpha (k_B T_c)^\alpha \int_0^\infty dx \frac{x^{\alpha-1}}{e^x - 1}. \tag{3.15}$$

This integral can be evaluated using special functions as

$$N_c = C_\alpha (k_B T_c)^\alpha \Gamma(\alpha)\zeta(\alpha), \tag{3.16}$$

where the gamma function $\Gamma(\alpha)$ and Riemann zeta function $\zeta(\alpha)$ have analytical solutions. For the three-dimensional particle in a box with $\alpha = 3/2$, we find

$$\frac{N_c}{V} = 2.612 \left(\frac{2\pi m k T_c}{h^2} \right)^{\frac{3}{2}}, \tag{3.17}$$

and 2.612 is the dimensionless phase-space density.

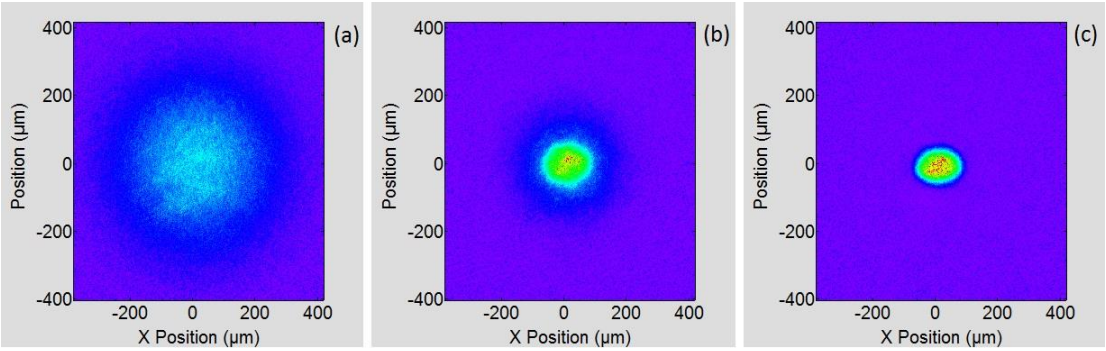

Figure 3.12: Absorption images taken in the chip laboratory after 25 ms time-of-flight. Purple represents zero atom density while red represents the highest atom density. (a) A thermal cloud, (b) a bimodal distribution (coexisting condensed and thermal phases), and (c) a nearly pure Bose-Einstein Condensate

Chapter 4: Apparatus Design and Construction

4.1 Design Motivation and Overview

For the physical design of the atom-chip apparatus, we aimed for a compact, simple system. Instead of a Zeeman slower, we use a vapor-fed 3D MOT cell, and load the MOT using light-induced atomic desorption (LIAD) [28]. The main vacuum components are the MOT and science cells, separated by a differential pumping tube located inside a vacuum chamber, as indicated in Fig. 4.1(b). Attached to this chamber is a gate valve that allows the MOT region to remain under vacuum when the science region is vented, for example, for atom-chip placement. Both vacuum regions have a dedicated ion pump (IP). Additionally, the science region contains a titanium sublimation pump (TSP) which has a connection for a turbo pump during bake out.

The two-celled vacuum system physically separates the MOT optics from the science cell region, leaving increased optical access to the science cell. In order to move atoms from the MOT cell to the science cell, we use magnetic transport [29]. The physical extent and plumbing complexity of the magnetic transport system was minimized by transporting in only one direction and having water-cooled towers to which the coils are mounted, instead of individually water cooled coils. Each tower

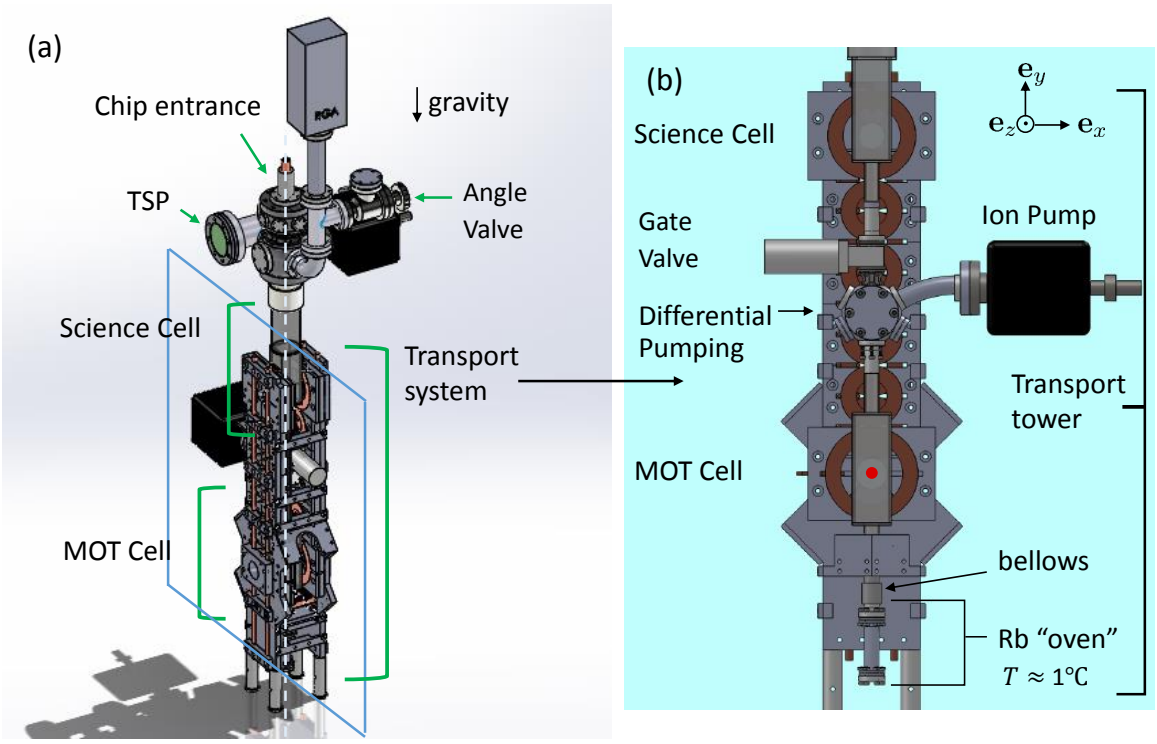

Figure 4.1: (a) The vertical atom-chip apparatus. The atom-chip will enter the vacuum system from the top. The magnetic transport system is used to move the atoms from the MOT cell to the science cell. (b) Cross-section of the apparatus. Of the vacuum components, the "oven" containing solid rubidium is mounted closest to the optical table. The oven connects to the MOT cell, where a vapor-fed MOT is produced using LIAD. Magnetically trapped atoms are then transported through the MOT cell, up through the differential pumping tube, into the science cell where a BEC is achieved in a dipole trap. The gate valve is used when we require venting one of the vacuum regions (while keeping the other under vacuum). The innermost transport coils are visible. With respect to the rest of the transport coils, the MOT and last pair of coils have larger inner diameters.

functions as both a cold plate and a mechanical mount for the coils (Fig. 4.1). The vertical apparatus design was chosen so that the long-armed chip holder could be inserted in the direction of gravity. Further, to simplify coil mounting and to avoid higher currents that would be required if coils wrapped *around* the vacuum system (coils would require much larger inner diameters), we oriented the axial direction $\mathbf{e}_z$ of the transport coils orthogonal to the gravity direction $\mathbf{e}_y$.

4.2 Vacuum Design

4.2.1 Rubidium Source

The oven houses solid rubidium in a 1.33" CFF nipple connected directly below the MOT cell. At this connection, the bellows located in the glass-to-metal adapter provides flexibility in mounting the oven to the table. The oven is fixed to the optical table with a custom designed adapter that houses a thermoelectric cooler (ThorLabs controller TED4015) used to temperature control the vapor pressure in the MOT cell. We typically maintain this "oven" at 1 C to keep the vapor pressure low ($\approx 10^8$ Pa). A constant flow of gaseous nitrogen out of 1/4" OD tubing keeps condensation from building on the temperature sensor. During experiment, LIAD is used to non-thermally increase the vapor pressure during MOT loading. We shine two ≈395-410 nm, 350 mW LED sources onto the MOT cell to accomplish this task (Mightex part SLS-0309-B, with driver SLA-1200-2). To maintain sufficient coating on the inner wall surfaces of the MOT cell, the oven temperature is periodically held at a warmer temperature of $\approx 10\,^{\circ}$C overnight.

4.2.2 Vacuum Cell Design

The MOT cell is composed of two commercial glass-to-metal-seal adapters from Larson Electronic Glass (both with 1.33" CFF, one with a bellows (BP1-075-F1-L1), and the other without (SP-075-F1)), and a custom Pyrex glass rectangular cell fabricated by the NIST optical shop in Gaithersburg, MD. The geometry of

the cell was determined by the anticipated size of the MOT beams ($1/e^2$ diameter at the atoms is $\approx$ 40 mm), and is 1.75" x 1.75" in inner cross-sectional area, 5.5" in length, with thickness 0.125". The science cell is designed similarly, also made from 0.125" thick Pyrex, with rectangular dimensions 4.5" x 1.75" x 1.75", with a short custom length 1.33" rotatable CFF to bellows adapter from Larson (BP1-075-F1(R)-L1-SPCL) attached to the bottom end, and a 4.5" rotatable CFF to bellows glass adapter on the top end (BP1-250-F4(R)-L1). The cross-section of the science cell was kept large in anticipation of a typically-sized chip-carrier with dimensions 1.32" $\times$ 1.32". The chip carrier is a 120-pin, ceramic, pin-grid-array, purchased from Spectrum Semiconductor Materials, Inc. (part CPG12009).

The science cell was designed to extend beyond the cooling towers in height so that the glass-to-metal adapter, which is too wide to fit between the towers, would be out of the way as shown in Fig. 4.1(a). The safe glass-working distance required for the process of attaching the glass-to-metal-seal adapters to the rectangular cell added additional unplanned length to the realized apparatus. The final flange-to-flange length of the MOT cell is $\approx$38 cm, and the science cell has length $\approx$46 cm.

4.2.3 Differential Pumping and Mounting

On the Kimball Physics chamber (part MCF275-SphHex-C2A6), located in between the two cells, are mounted two faced-off 2.75" CFFs. The total chamber plus conflats width along $\mathbf{e}_z$ (coordinates as defined in Fig. 4.1) had to be narrowed because the total width extends beyond the widths of all other vacuum parts (i.e.

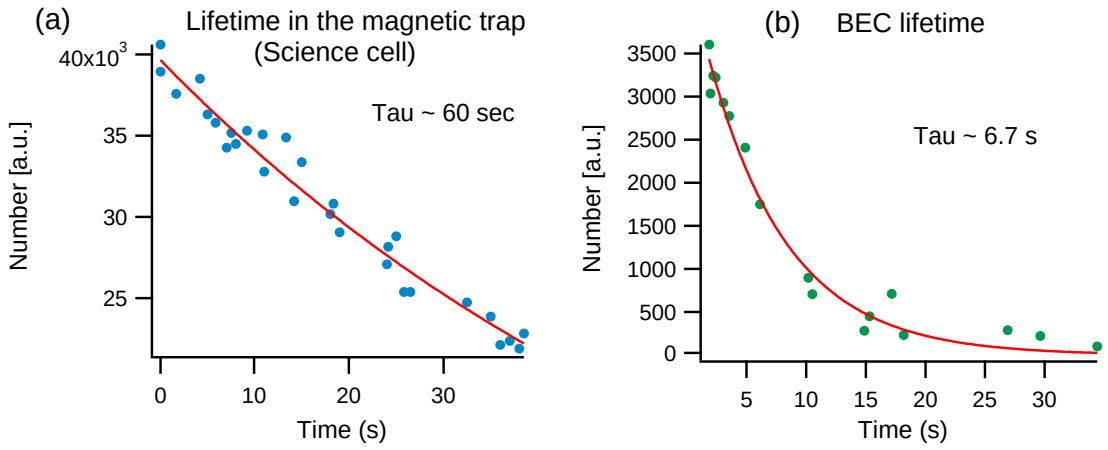

Figure 4.2: Lifetime measurements of (a) magnetically trapped $|F = 2, m_F = 2\rangle$ atoms (blue circles), and (b) a BEC in the same spin polarized state (green circles). The exponential fits are shown in solid red.

it was the limiting factor in how close together we could mount the transport coil pairs). The narrowing allowed the transport coil pairs to be closer together and thus provide a more optimal geometry (to minimize currents required for the desired trap gradient). The chamber houses a differential pumping tube (Duniway CA-133). The differential pumping tube and the two Varian StarCell 20 L/s IPs allow the science cell to be kept at a lower vacuum pressure (compared to the MOT cell) suitable for BEC production and experiment: typically, the lifetime of magnetically trapped atoms in the $|F = 2, m_F = 2\rangle$ state is $\approx$ 5 s in the MOT cell, and $\approx$ 60 s in the science cell (Fig. 4.2(a)). The lifetime of a BEC in the same spin polarized state was measured to be $\approx$ 7 s in the dipole trap, as shown in Fig. 4.2(b).

The experiment is largely supported and attached to the optical table with commercial 80/20 Inc. extruded aluminum frames and fixtures. Additionally, custom supports fix the two cells vertically in place (Fig. 4.4, and V-clamps support the IPs).

Above the science cell, a "cross", a "T", and an elbow make up the connections to the science region IP, angle valve, TSP, and Turbo pump. The elbow keeps the valve out of the TSP's line-of-sight (Fig. 4.1(a)).

4.2.4 Chip Holder

The dimensions of the in-vacuum atom-chip holder was constrained by the vacuum components located along its path to the science cell. The chip will be placed inside the vacuum because we will require the BEC to be $\approx 5\,\mu$m away from the chip surface. The atom-chips are custom fabricated by NIST Center for Nanoscale Science and Technology (CNST) in Gaithersburg.

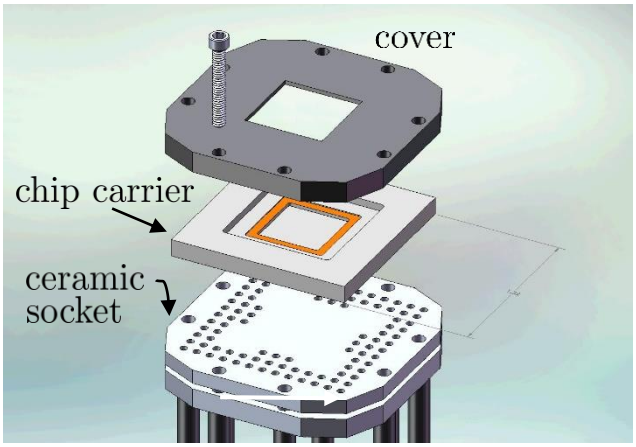

Figure 4.3: The chip will be mounted from the top of the experiment. Stainless steel extends from the uppermost conflat on the apparatus, designed to place the chip near the center of the final quadrupole trap.

4.2.5 Vacuum Bakes

Before assembling the vacuum system, most components were cleaned in an ultrasonic bath. This was a two- or three- step process: first, a bath with soap

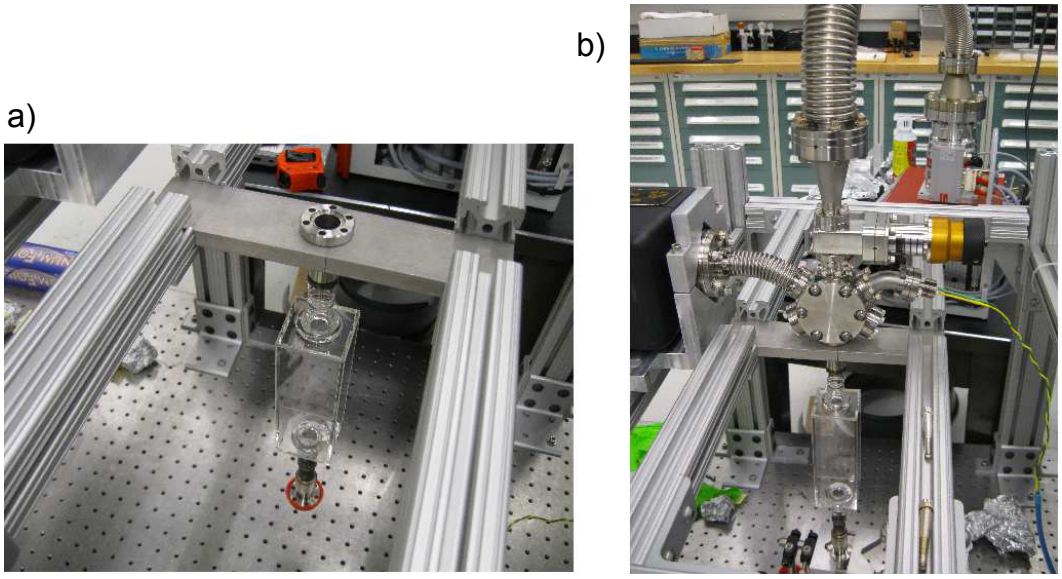

Figure 4.4: First part of vacuum assembly (MOT region). a) The MOT cell is mounted vertically using a custom holder, so that the cell "sits" on the holder. b) The MOT region fully assembled. Screws inserted from underneath the holder seals the cell and octagonal chamber together. Depicted here is the initial "pump" out stage using a turbo pump (Pfeiffer HiCube 80 eco), attached to the chamber at the top, after the gate valve. A 1.33" CFF bellows connects the left side of the chamber to the MOT region IP.

and water if the part was particularly dirty (e.g. oily), then an acetone bath, then lastly a methanol bath. Once the parts were assembled, the entire system was baked (heated) to remove water and hydrogen. The vacuum system was covered in aluminum (Al) foil, then wrapped in heat tape, then wrapped again in several layers of Al foil. We used the Dukal Corp. "survival wrap" as the outermost layer of our oven. Each heat tape temperature was controlled by a Variac. Our apparatus is primarily made up of metal and glass: because these two materials have different thermal expansion coefficients, it is particularly important to avoid rapid temperature changes when baking any of the metal-to-glass joints. We generally increased the temperature at a rate of $\approx$20 C/hour. Fig. 4.5 shows the pressure

change over time of a bake performed on the MOT region of the apparatus.

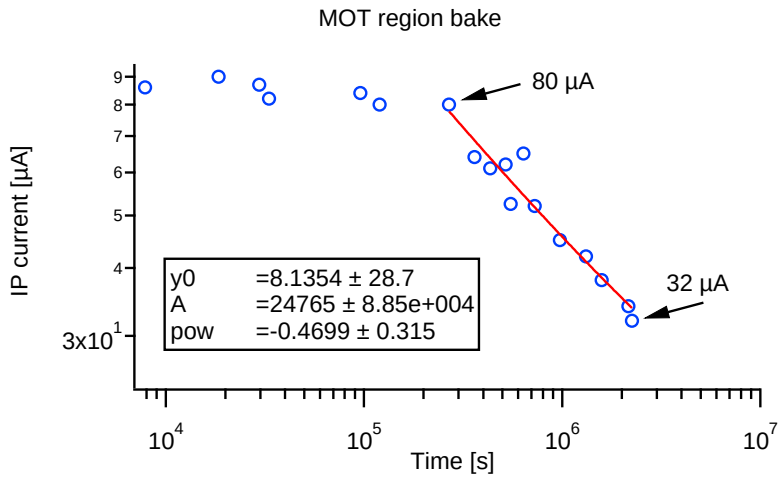

Figure 4.5: MOT region vacuum bake-out performed, while the science cell was being manufactured by the NIST Optical Shop. The vacuum pressure is proportional to ion pump current. The fit to the data from time $\approx 2.7 \times 10^5$ s to $\approx 2.25 \times 10^6$ s is of the form IP current $= y_0 + A*t^p$.

4.3 Magnetic Transport

4.3.1 Transport Design

We magnetically trap and transport atoms in the $|F = 2, m_F = 2\rangle$ state, taking advantage of the factor of two we gain in the energy gradient (Zeeman splitting $\approx$ 1.4 MHz/G) compared to $|f = 1, m_F = -1\rangle$ atoms. The atoms are microwave transferred after magnetic transport (during dipole evaporation) to the lower-loss [36] $|f = 1, m_F = +1\rangle$ state.

Magnetic transport is achieved using a series of overlapping coils in an anti-Helmholtz type configuration. The general idea is to keep the magnetic trap geometry constant while the atoms are spatially moved from the starting location (MOT

cell), to the final position (science cell). This ensures minimal heating of the atoms, and is accomplished by invoking three constraints:

$$\frac{\delta B}{\delta z} = 120\,\mathrm{G/cm}, \tag{4.1}$$

$$\frac{\delta B}{\delta y} = 47\,\mathrm{G/cm}, \text{ and} \tag{4.2}$$

$$A = \frac{(\delta B/\delta x)}{(\delta B/\delta y)} = 1.28, \tag{4.3}$$

where $\delta B/\delta z$, $\delta B/\delta y$, and $\delta B/\delta x$ are the magnetic field gradients along the strong axis, transport axis, and the non-elongated weak axis, respectively and A is the resulting aspect ratio in the $x-y$ plane. We solve for three unknown variables I_1, I_2, and I_3, the currents in three adjacent sets of coil pairs at any given time. We solve for the currents numerically, starting from the center of the MOT coils to the center of the final coil pair (which is used in the hybrid trap [7]). Except for the very first and last transport segments, three coil-pairs are energized at any given time during transport. During transport, the effective magnetic trap is elongated along the transport direction $\mathbf{e_y}$. The calculated transport sequence is shown in Fig. 4.6.

Eleven anti-Helmholtz coil pairs transport magnetically trapped atoms from the MOT cell to the science cell in 2.2 seconds, at an average speed of 200 mm/sec. The transport sequence requires constant trap gradient to minimize heating of the atoms. Further, all currents are positive (the power supplies are uni-polar).

We empirically touched-up the calculated transport sequence. We found that the transport velocity preferred to be slowest in the middle of transport, close to the gate valve, as shown in Fig. 4.7. We suspect that the necessity for slow speeds

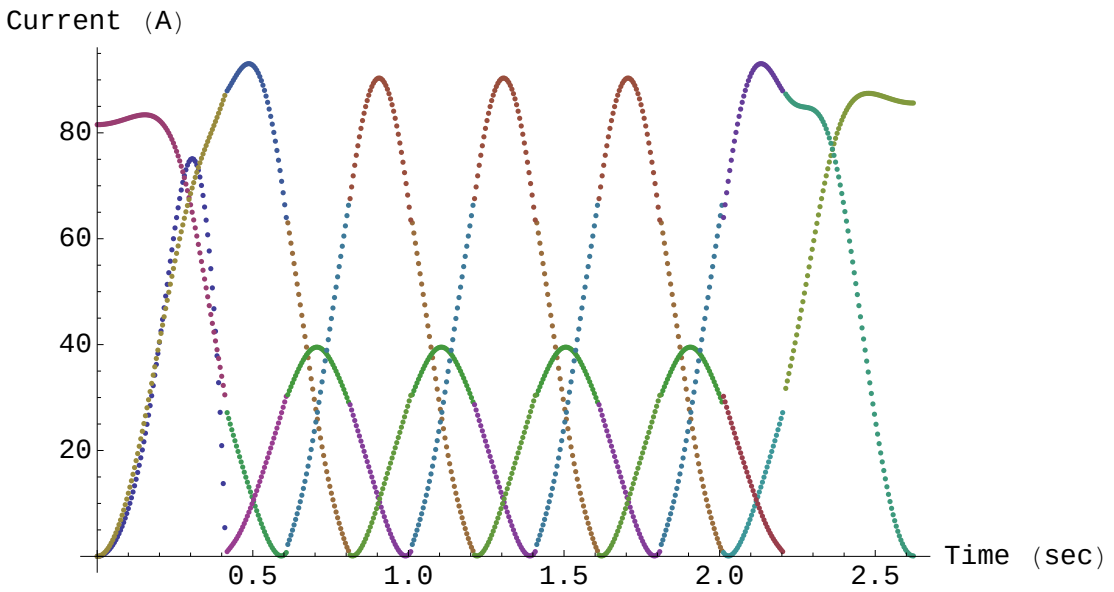

Figure 4.6: Calculated magnetic transport sequence; current in each of four coils as a function of time. The time axis was generated by scaling the calculated gravity gradients to the measured gravity gradients.

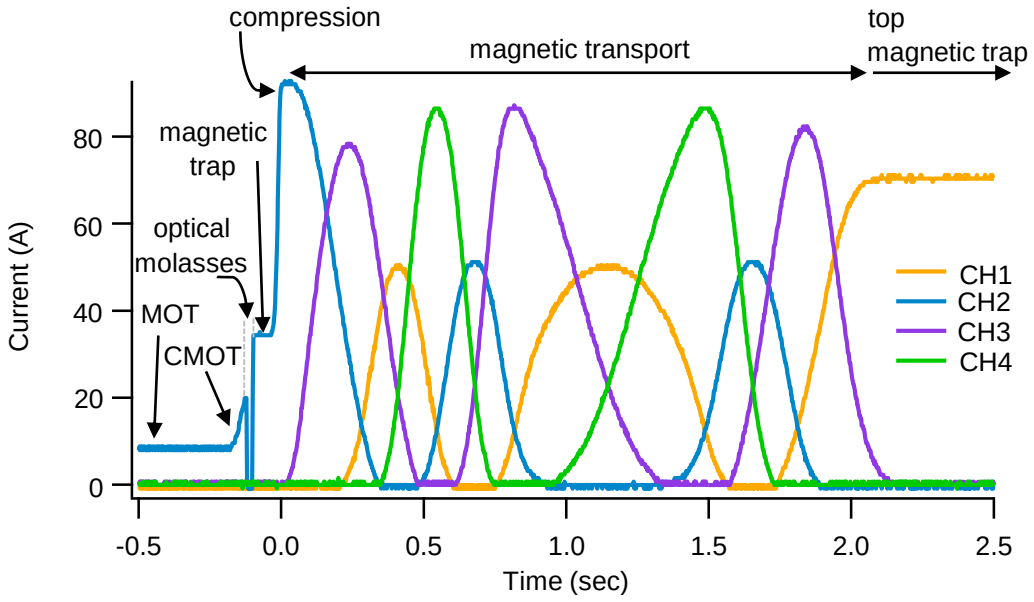

Figure 4.7: Actual magnetic transport sequence; current in each of four coils as a function of time.

in this region may be due to a magnetized component inside the valve. The transport efficiency was measured to be $\approx 85\%$, with most of the loss occurring at the

beginning of transport from collisions with background Rb atoms.

4.3.2 Characterization of the Transport System

The transport system (coils, coil holders, and cooling tower) was designed to fit around the vacuum components, and to provide cooling to the transport coils. For simplicity, we designed all coils to be as similar as possible in geometry. Each transport coil was wound with "ribbon" magnet-wire laminated on one side with Kapton insulation from Alpha-Core. Three types of wire were used to construct the transport coils: wire with copper cross-section $12.7\,\text{mm} \times 0.254\,\text{mm}$ ($0.5" \times 0.01"$) for all "top" quadrupole pairs (coils further away from the vacuum system) and push coil, cross-section $6.35\,\text{mm} \times 0.254\,\text{mm}$ ($0.25" \times 0.01"$) for all "bottom" pairs (coils closest to the vacuum system), and the MOT and final quadrupole pairs were made with custom-sized $0.3" \times 0.02"$ wire. Coil specifications are listed in Table 4.1. We list the specifications from the manufacturer in the second column, and the actual dimensions measured using a caliper, in the third column.

Table 4.1: Wire dimensions

Wire type	Specifications	Measured
A (for "bottom" coils)	$0.25" \times 0.01"$	$0.350" \times 0.013"$
B (for "top" coils)	$0.50" \times 0.01"$	$0.625" \times 0.013"$
C (for "MOT" and "final" coils)	$0.30" \times 0.02"$	$0.425" \times 0.023"$

After the coils were wound and assembled onto the transport tower, we measured the resistance of each coil, as shown in Table. 4.2. The test lead resistance

of 62 mΩ has been taken into account (the resistance listed is for the coil only).

Table 4.2: Characterization of each coil

Coil# Tower 1	Current (A)	Voltage (V)	Resistance (mΩ)	**Coil# Tower2**	Current (A)	Voltage (V)	Resistance (mΩ)
1	4.99	0.509	40	**1**	4.99	0.527	44
2	4.99	0.603	59	**2**	5.02	0.615	61
3	4.99	0.904	119	**3**	4.99	0.904	119
4	4.99	0.597	58	**4**	4.99	0.609	60
5	4.99	0.892	117	**5**	4.99	0.904	119
6	4.99	0.597	58	**6**	4.99	0.609	60
7	4.99	0.904	119	**7**	4.99	0.904	119
8	4.99	0.603	59	**8**	4.99	0.609	60
9	4.99	0.915	121	**9**	4.99	0.921	123
10	10	1.204	58	**10**	4.99	0.621	62
11	4.99	0.527	44	**11**	4.99	0.539	46

Next, a Hall probe was used to measure the magnetic field of three representative coils at different distances Z from the coil surface. The measurements agreed well with the predicted (calculated) values (Table 4.3). The Hall probe was also used to double check the chirality of each coil.

Table 4.3: Gradient measurements

	Magnetic Field Measured/Calculated (Gauss)		
Coil	Z = 0	Z = 12.7mm	Z = 25.4mm
6	42/44	23/24	12/13
7	61/62	38/41	21/22
11	20/21	18/18	13/13

Once we could transport the atoms from the MOT cell to the science cell, we calibrated the magnetic field gradient of each coil pair by measuring the gravity gradient. The results are shown in Table 4.4. The computed gravity currents were

21.3 A for the "MOT" trap (coil pair # 1), 19.9 A for the "final" trap (# 11), 7.4 A for "bottom" coils (all other odd numbered pairs), and 13.4 A for "top" coils (all even numbered pairs).

Table 4.4: Calibration of gradients

Coil pair #	Gravity current (A)	**Coil pair #**	Gravity current (A)
1	19.7	**7**	6.0
2	17.1	**8**	16.8
3	8.7	**9**	8.1
4	16.3	**10**	18.8
5	10.3	**11**	21.0
6	16.6	–	–

Except for the very first and last portion of the transport sequence, all coils of the same geometry run the same spatial current profiles; though we allow variations in the transport velocity. We used genetic optimization [38] to optimize each stage of our experiment, up to BEC production. The example optimization run shown in Fig. 4.8 included 14 transport sequence variables to optimize transport currents as a function of the distance traveled by the atoms (transport velocities were fixed). We found that the algorithm results were comparable to the results obtained with time-consuming manual optimizations. We typically ran the algorithm overnight. Further, because of the high stability of our apparatus, we also ran scans over entire weekends. We also used the algorithm as a multi-tasking tool while working on projects off-line.

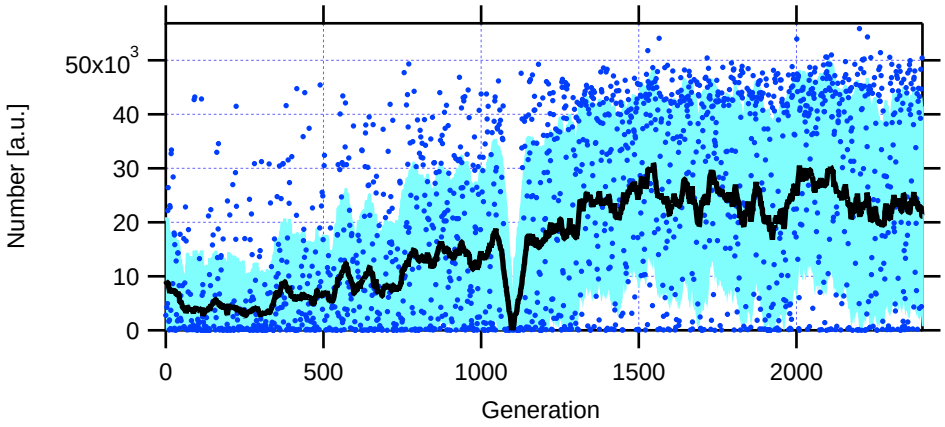

Figure 4.8: Example genetic optimization [38] of the experimental sequence of our apparatus. In this optimization run, we optimized 14 variables in the transport current functions. In this figure we measure atom number as a function of the variables that determine the shape of the commanded current profiles during magnetic transport. These include the variables which determine the maximum current amplitude, the width, and curvature.

4.3.3 Fabrication of Transport Coils

Each coil was wound on an aluminum form machined with the desired coil inner diameter. The design requires removal of excess Kapton to achieve desired coil height and good thermal contact requirements. Each winding form could adapt onto a lathing form with four screws, as shown in Fig. 4.9a. The lathing form fit into a standard 1/2" collet for machining (Fig. 4.9b). To prepare wound coils for machining, the gaps between Kapton layers were filled with a fluid and machinable epoxy (Stycast 1266). To minimize air bubbles and gaps within the epoxy, each coil was placed inside an evacuated bell jar immediately after application of the epoxy for ≈ 30 minutes, then left to cure overnight at room temperature.

Each coil was lathed up to the copper surface and was checked for shorts under a microscope (Fig. 4.10). When a short was identified, the copper was etched with

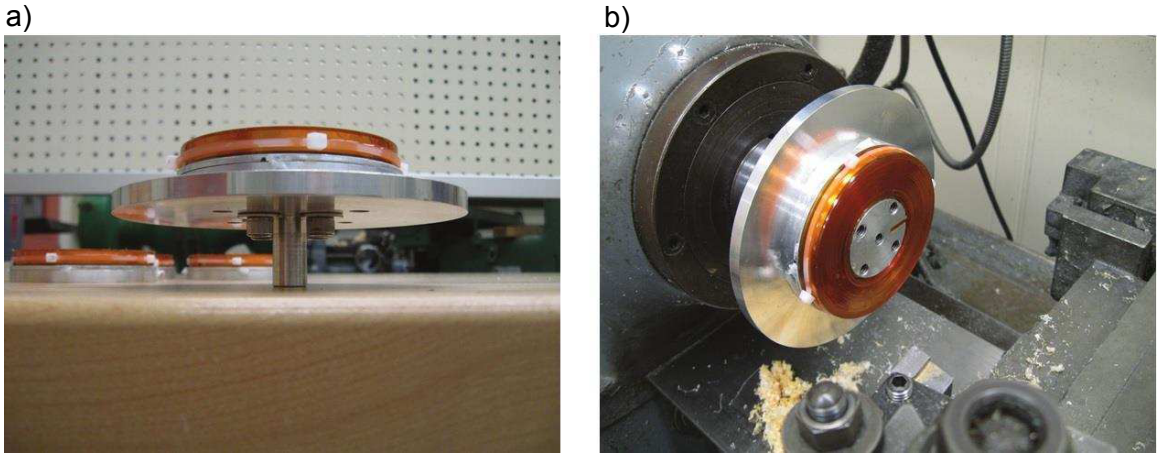

Figure 4.9: a) Transport coil mounted on lathing form. The cable tie was attached to keep the coil from unwinding while the machinable epoxy (Stycast 1266) cured. Each winding form is designed to adapt onto the lathing form for machining. b) We lathed off the excess Kapton on both the front and back surfaces to achieve a smooth finish for better thermal contact between surfaces.

a 1:1.4 mixture of nitric acid and water until no short remained.

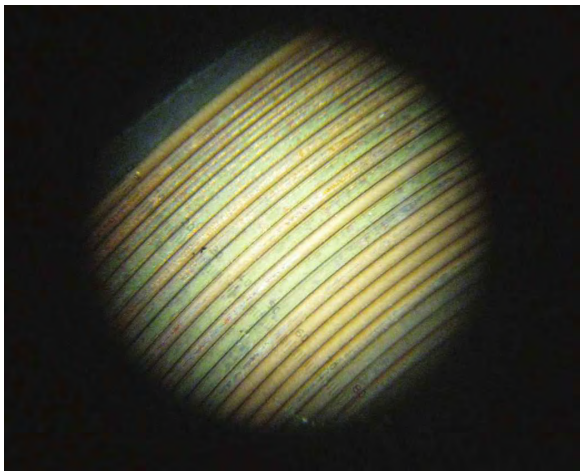

Figure 4.10: A transport coil under a microscope. Each closely lathed-down coil was inspected under a microscope to check for shorts. If a short was discovered, the coil was etched with a nitric acid solution.

4.3.4 Design of coil holders and cooling towers

Coils were fixed to mounting forms with thermally conductive epoxy (Omegabond 200).

The epoxy extends over the coil surface to eliminate height discrepancies between

the mounting form and coil, and provides increased thermal conductivity between coil layers. The coils were then assembled onto two monolithic cold plates containing multiple slits to minimize eddy currents. In addition, thermal compound was applied between each layer. Most of the machined parts are made of aluminum, which is an economical thermal conductor that is relatively easy to machine. The cooling tube clamps are made of stainless steel, which has electrical conductivity an order of magnitude lower than that of aluminum, to prevent shorting the cold plate slits.

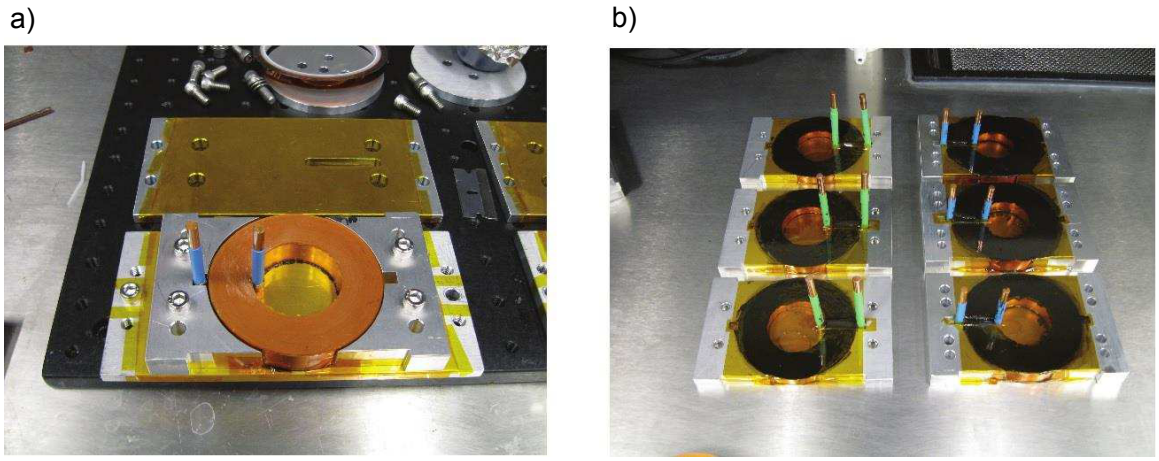

Figure 4.11: Coil mounting procedure. a) A coil has been glued with a thermally conductive epoxy to its holder, and the second side is ready to be glued. The entire assembly is then baked to cure the epoxy. b) Several mounted coils ready for installation.

4.3.5 Current control

Four Agilent 6672A 20V/100A power supplies provide currents to the coils, and three coils run current at any given time of transport. Having a fourth supply allows every Agilent to have a "rest" segment (to completely turn off) before rejoining the

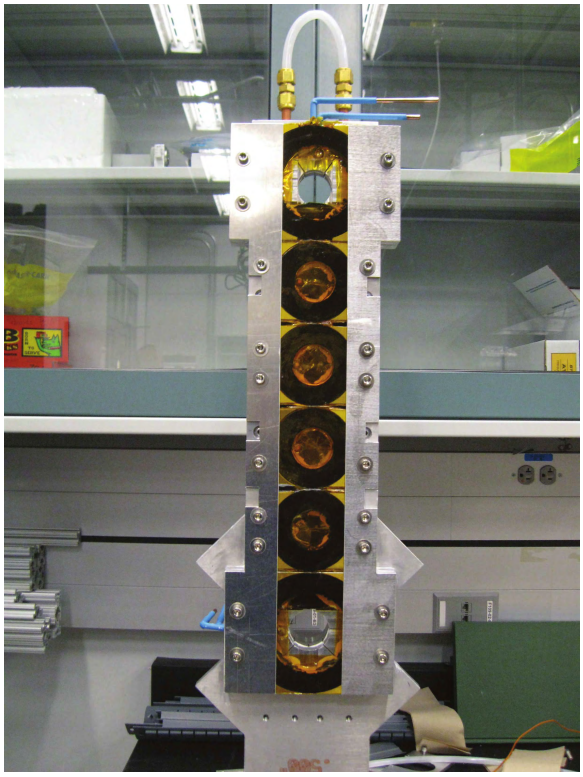

Figure 4.12: Two transport towers (one shown) with eleven transport coil pairs make up the magnetic transport system. The narrow aluminum panels on the right and left sides of the coils provide extra mechanical support to the vertically mounted coils.

cycle. We use MOSFETs (part IXFN520N075T2, 75 V, 480 A from IXYS), which are mounted on water cooled cold plates, to control the currents through the transport coils.

4.4 Microwaves for internal state control

The general set-up of the microwave source used for internal state control was adapted from those used in the lattice and gauge fields labs in the Laser Cooling group [39]. A microwave horn placed several inches from the experiment is used to transfer atoms between the $F = 1$ and $F = 2$ ground hyperfine states. As

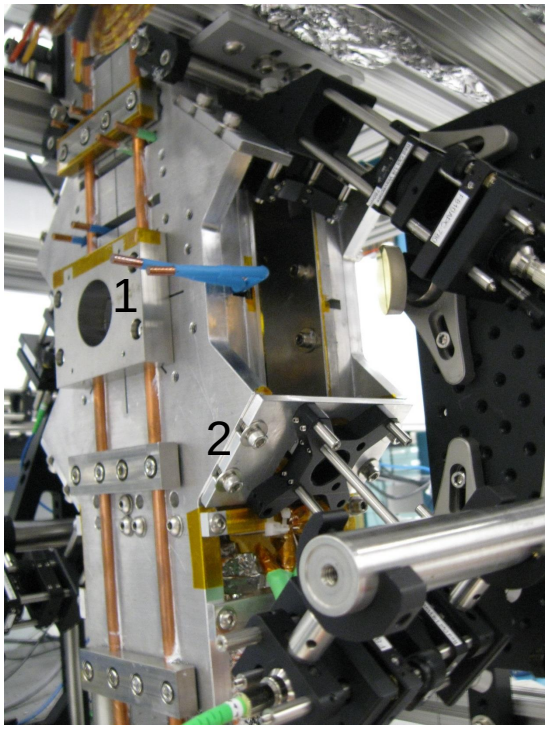

Figure 4.13: The majority of the MOT optics were assembled using Thorlabs 30 mm "cage systems". The MOT region is pictured here, with "1", and "2" indicating transport-tower-to-cage adapter parts. The adapters also serve as clamps: "1" clamps down on the two copper water cooling tubes, and "2" connects the two towers together.

the microwave source, we use Stanford Research Systems SG 384, and send the microwave signal through the set-up shown in Fig. 4.14. The microwave power measured after the various components is listed in Table 4.5.

4.5 Laser systems

We have three laser systems in the laboratory: the master/repump, cooling, and dipole boards, shown in Figs. 4.15, 4.16, and 4.17, respectively [40]. Together, these laser beams provide all of the laser light required for BEC production.

We use a Toptica DL Pro diode laser for the master/repumper, and a Toptica

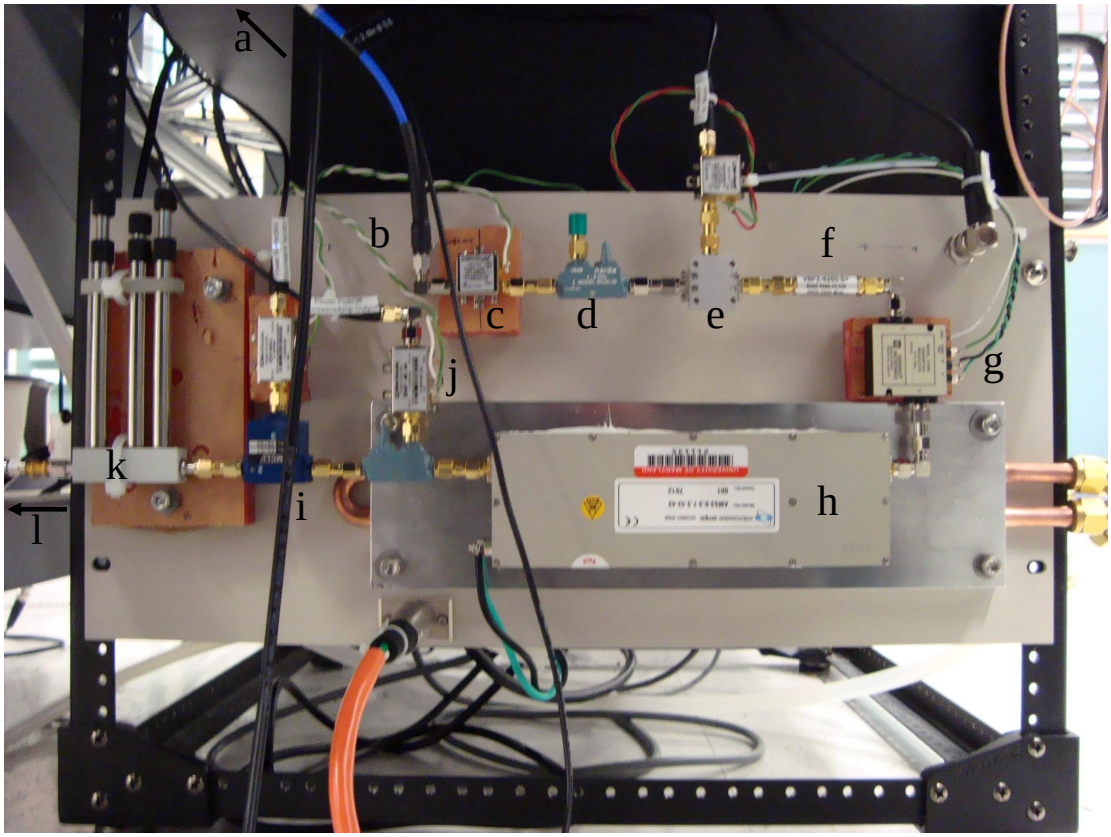

Figure 4.14: Microwave set-up.

TA Pro diode-laser-and-tapered-amplifier integrated system for the cooling board. Toptica's DigiLock 110 provides PID feedback for locking to the saturation absorption signal. We perform saturation absorption spectroscopy with a Triad Technology rubidium reference cell heated to 50 C using ThorLabs' cell heater GCH25-75.

The light to the dipole board is provided by an IPG Photonics 30 W fiber laser. All mirrors are mounted on ThorLabs 1" mirror mounts (POLARIS-K1). We use a metal jacketed high power fiber from NKT Photonics (LMA-PM-15) with custom SMA905 8° angle polished ends.

Table 4.5: Main microwave setup

Label	Element	Output Power (dBm)	Manufacturer (part number)
a	Source	-10.7	Stanford Research Systems (SG384)
b	Cable	-12	company name (part number)
c	Amplifier	14.7	Minicircuits (ZX60-183-S+)
d	Directional Coupler	14.0	Narda (4014C-30)
e	Mixer	-6.7	Marki (IRW-0618MXW-1)
f	Band-Pass Filter	-10.6	Minicircuits (VBFZ-6260-S+)
g	Attenuator (0V)	-11.3	General Microwaves (Herley) (D1956)
h	Amplifier		Microwave Amplifiers (AM53)
i	Circulator-Isolator		MCLI (CS-57)
j	Power Detector		Minicircuits (ZX47-40-S+)
k	Stub Tuner		Maury Microwave 1819C
l	Antenna/Horn		(part number)

4.6 Atom-chip fabrication

In this section, we will give an overview of the main steps used to fabricate our atom-chips (all chips are fabricated by CNST at NIST, Gaithersburg). Fig. 4.18 shows a pictorial summary of these steps. A technique was developed which mixed and matched two lithography techniques. The two techniques used are optical projection lithography (good for features sized greater than 0.4 μm), and electron beam (e-beam) lithography (for features less than 0.4 μm). Due to the fine-resolution of the e-beam technique, imaging the entire RF "Raman" design using this technique would require long write-times and is cost-prohibitive. However, the small wire spacing required for the 100 parallel wires requires the e-beam resolution.

For a cost-effective, time-efficient fabrication, the chip is created using a two-step lithography process: the wire "pads" which branch out from the parallel wires

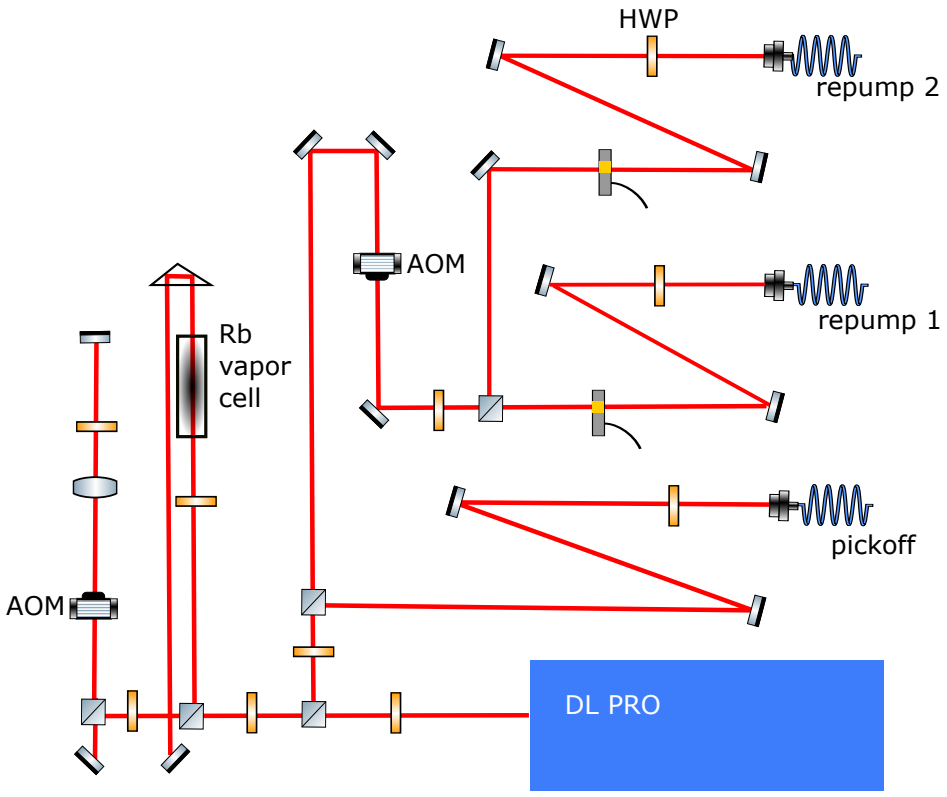

Figure 4.15: The repump/master laser system. The DL Pro is locked to the 87Rb $F = 1 \rightarrow F' = 2$ repumping transition using saturation absorption spectroscopy. We use a pick-off at the laser output (before any AOMs) to beatnote lock the cooling laser.

to where electrical connections are made (via wirebonding) are predominantly drawn with the photo-lithography technique, pictured in Fig. 4.18(d). The resolution R of this technique is diffraction limited, i.e. is dependent on the wavelength λ_l of the light used, and the numerical aperture (NA) of the imaging system, $R \propto \lambda_l/NA$. In the second step, the fine-scaled parallel wires which will create the moving magnetic fields described in Sec. 2.6.2 are drawn with e-beam lithography, Fig. 4.18(g). The e-beam technique may draw features down to 2 nm.

Finally, the image of the wire patterns is etched onto the gold layer using the ion milling technique: Ar+ forms a compound with Au, physically separating Au

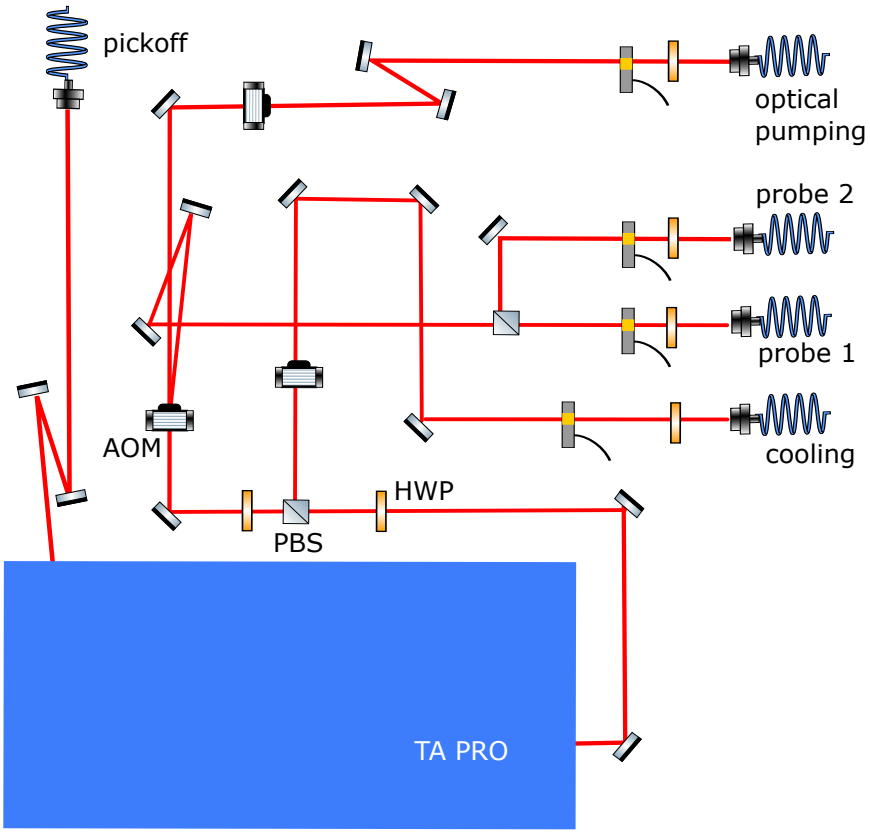

Figure 4.16: The cooling laser board. The Toptica TA Pro provides power to the MOT and probe beams. The laser is beatnote locked to the repump laser (Fig. 4.15), and locks red detuned from the $|f = 2, m_F = 2\rangle$ to $|f = 3, m_F = 3\rangle$ cooling transition.

from the layer. After the gold etching is complete, the resist is stripped off, leaving the gold wire patterns exposed and ready for wiring (Fig. 4.18(g)-(i)).

The cross-section of our first physical test-chip is shown in Fig. 2.7. Bench testing is underway.

4.7 Conclusion

Techniques used to achieve Bose-Einstein condensation were reviewed as the necessary first step in simulating solid-state systems using cold atoms in engineered

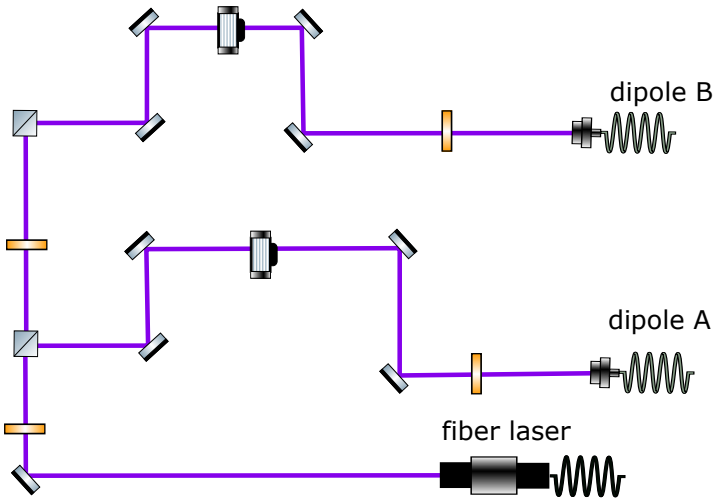

Figure 4.17: The 1064 nm dipole board. The laser is injected into one high power fiber. At the fiber output (located on the experiment board), the beam is split into two using an AOM. The two beams are used as a crossed-dipole trap, an all-optical trap in which Bose-Einstein condensation is achieved.

vector potentials. The atom-chip experiment will replace Raman light-coupling with RF coupling to eliminate scatter and may pave the way for next-generation experiments that simulate condensed matter systems. The first test chip for light-less "Raman"artificial gauge fields is currently under development.

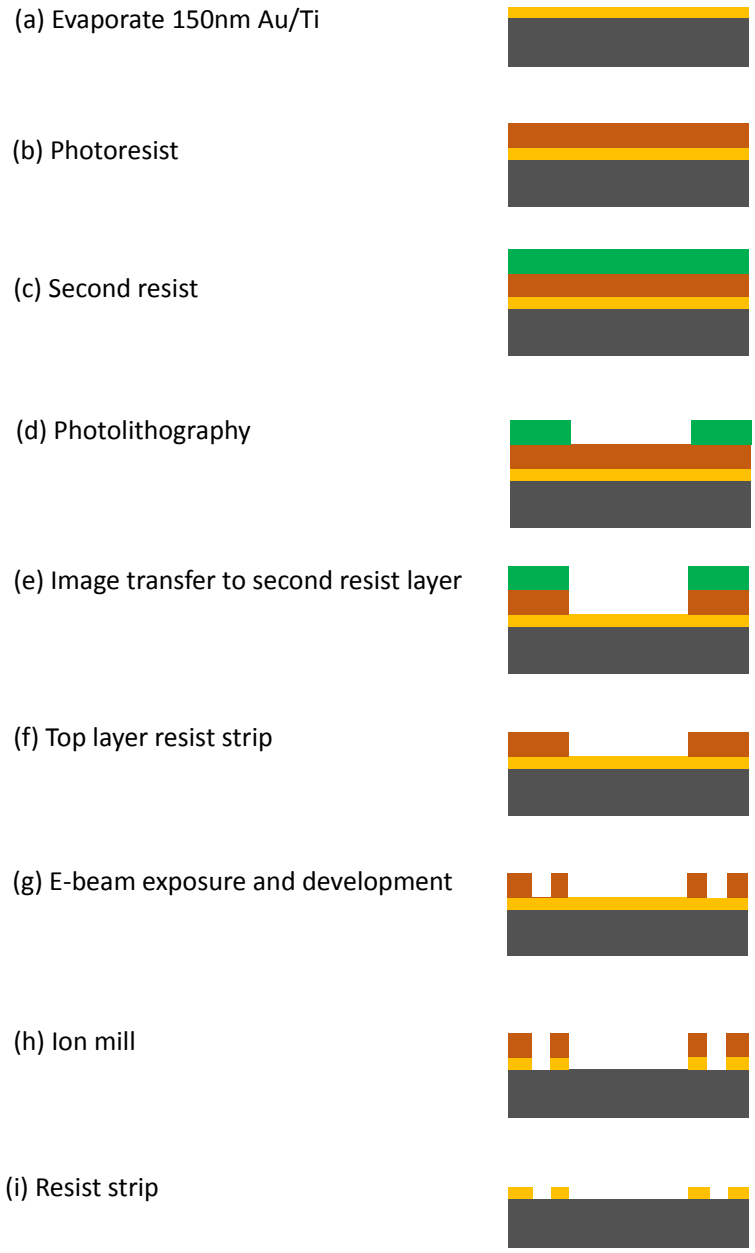

Figure 4.18: Two-layer lithography. The patterning technique developed at CNST uses both electron lithography and optical projection lithography. In the preliminary steps, (a) Au is evaporated onto a sapphire substrate, (b) the Au is covered with photoresist used for photo-lithography imaging, and (c) a layer of resist appropriate for electron beam lithography is laid on top of the photoresist. Now the chip design pattern is ready to be imaged on to the resists: (d) photo-lithography for structures 2 μm - 0.4 μm, (e) image transfer onto the second resist layer, (f) removal of the photoresist exposes the surface of the second resist, which is now ready for e-beam lithography: (g) E-beam process for the fine features of the chip (i.e. the parallel wires). This step (g) completes the drawing process, and finally (h) the ion mill is used to etch the image on to the Au layer. Finally, (i) The resist is removed and the patterned Au remain.

Chapter 5: Multiple-camera off-resonance defocused imaging of ultracold atomic gases

5.1 Introduction

Ultracold atoms exist in isolation, enshrouded in ultrahigh vacuum, so that nearly every measurement on them relies on their interaction with electromagnetic fields. The most common measurements use a probe laser beam that is attenuated and phase shifted by the atoms to recover two-dimensional images of the integrated density–the column density–of the atoms. Whether the technique be absorption imaging, or phase-contrast imaging (PCI), the spatially resolved column density of the atomic cloud is recovered to retrieve information about the experiment.

In this chapter, we extend the method of off-resonance defocused (ORD) imaging pioneered in Refs. [41–43]. In ORD imaging, a probe laser propagates through a thin atomic cloud and is both absorbed and phase-shifted, in contrast to on-resonant-absorption or phase-contrast imaging in which the probe is dominantly absorbed or phase-shifted, respectively. Both the absorption and phase-shift are proportional to the quantity of interest, the column density. For small detunings δ, the absorption $\propto 1/\delta^2$, while the phase-shift $\propto 1/\delta$: the phase-shift dominates

quickly as δ is increased. Typically, absorption imaging [44] is used for clouds of low to medium OD using a on-resonance probe beam (no phase-shift), and PCI [45] is used to image clouds of high OD using a far-detuned probe beam (negligible absorption). In absorption imaging and PCI, images are recorded by a detector at the focus of the imaging system. In ORD imaging, a defocused image is taken by a detector positioned away from the focus: remarkably, Ref. [42] showed that it is possible to digitally refocus intensity images of atoms without knowing the phase of the underlying electric field. Still, ORD was beset with unavoidable imaging artifacts; here we demonstrate a technique to reconstruct defocused images of ultracold atoms absent artifacts. In this technique, multiple-camera off-resonance defocused (MORD) imaging, we simulateously use three cameras placed at different defocused distances and show that suitably placed cameras allow for artifact-free reconstruction of the atomic column density. We then compare this technique to conventional imaging techniques and show that its signal to noise ratio (SNR) is comparable to absorption imaging near atomic resonance and comparable to phase contrast imaging far from resonance.

This chapter is organized as follows; in Sec. 5.1 we discuss the solution to the vector wave equation under the paraxial approximation for a thin, dilute cloud. In Sec. 5.2, we describe absorption and phase-contrast imaging. We then make additional approximations to the electric field which has propagated through the cloud, and derive the ORD and MORD solutions to the wave equation. In Sec. 5.3, we describe the experimental implementation of the MORD method, and the procedure we used to prepare condensates of low OD. In Sec. 5.4, we present our experimental

MORD results and theoretically compare this method to absorption and phase-contrast imaging.

5.1.1 Propagation of an electromagnetic wave

First we introduce the theoretical problem, starting with the propagation of an electromagnetic wave. For our neutral atomic systems interrogated by a monochromatic probe laser beam with wavelength λ and wave number $k_0 = 2\pi/\lambda$, the evolution of the electric field of the beam in the presence of atoms with complex susceptibility χ, is described by the scalar wave equation:

$$\nabla^2 E_i(\mathbf{r}) + k_0^2[1 + \chi(\mathbf{r})]E_i(\mathbf{r}) = 0, \tag{5.1}$$

also known as the Helmholtz equation, for each polarization component i, provided that the susceptibility χ changes slowly with respect to λ (i.e. the cloud is not too dense) [46]. In the next section we derive the solution to eqn. (5.1) for a thin, dilute medium.

5.1.2 Solving the Helmholtz equation

The Helmholtz equation, valid for monochromatic light traveling through a homogeneous isotropic medium, has the formal solution

$$E(\mathbf{r} + \Delta z\mathbf{e}_z) = \exp\left[\pm i\Delta z\left(\nabla_\perp^2 + k_0^2 + \chi(\mathbf{r})k_0^2\right)^{1/2}\right] E(\mathbf{r}) \tag{5.2}$$

for light traveling along $\mathbf{e}_z$, where $\nabla_\perp^2 = \partial^2/\partial^2 x + \partial^2/\partial^2 y$, and $E(\mathbf{r} + \Delta z\mathbf{e}_z)$ is the field which has propagated a distance Δz through the medium, and E($\mathbf{r}$) is the field

before propagation. From here forward, we consider the complex susceptibility of a two-level atom:

$$\chi(\mathbf{r}) = \frac{\sigma_0}{k_0}\left[\frac{i - 2(\delta/\Gamma)}{1 + I(\mathbf{r})/I_{\text{sat}} + 4(\delta/\Gamma)^2}\right]\rho(\mathbf{r}), \tag{5.3}$$

where $\sigma_0 = 3\lambda^2/2\pi$ is the resonant cross-section, I_{sat} is the saturation intensity, δ is the probe detuning from atomic resonance, and Γ is the linewidth of the transition. Here we define $\Delta = \delta/\Gamma$ as the detuning in linewidth units.

For the problem at hand, we take the paraxial approximation and consider a cloud with finite thickness δz under the condition $\delta z \ll (\delta l)^2/\pi\lambda$, where $(\delta l)^2/\pi\lambda$ is the depth of field, and δl is the minimum resolvable length determined by the imaging system resolution [46]. In the paraxial approximation, $E(\mathbf{r} + \Delta z\mathbf{e}_z)$ is negligibly diffracted from its original path along $\mathbf{e}_z$ so that $\nabla_\perp^2 \ll k_0^2$. This approximation can be made for a dilute cloud with density $\rho(\mathbf{r}) \ll k_0^3$. For such a thin, dilute system, $|\chi(\mathbf{r})| \ll 1$.

The electric field after propagation through the cloud, is found by repeatedly applying a step-wise propagator to the initial electric field. Such a propagator under the paraxial approximation is found by taking the small susceptibility limit of the argument in eqn. (5.2): $\{1 + [\chi(\mathbf{r}) + (\nabla_\perp^2/k_0^2)]\}^{1/2} \approx \{1 + (1/2)\,[\chi(\mathbf{r}) + (\nabla_\perp^2/k_0^2)]\}$. Then we find the separable solution $E(\mathbf{r} + \Delta z\mathbf{e}_z) = \exp(i\Delta z k_0)E'(\mathbf{r})$ for a wave propagating along $\mathbf{e}_z$. Inserting this field into the scalar wave equation, we find the paraxial wave equation

$$-2ik_0\frac{\partial E'(\mathbf{r})}{\partial z} = \nabla_\perp^2 E'(\mathbf{r}) + k_0^2\chi(\mathbf{r})E'(\mathbf{r}). \tag{5.4}$$

The electric field $E'(\mathbf{r})$ described above depends weakly on z, allowing the sus-

ceptibility integral to be solved numerically for any probe intensity $I(\mathbf{r})$ using the split-step Fourier method (SSFM, Sec. 5.6).

Under the paraxial approximation, the step-wise propagation operator through a dilute medium is

$$\mathbf{Q}'(\Delta z) = \exp\left[i\frac{k_0}{2}\int_z^{z+\Delta z}\chi(\mathbf{r})\,dz\right]. \tag{5.5}$$

5.2 Imaging techniques

5.2.1 Introduction

We now derive an invertible relation between the observed intensity and the atomic column density that recovers all but a small range of spatial frequencies: the basis of the ORD imaging technique. The electric field propagating through the cloud using eqn. (5.5) is

$$E(\mathbf{r}+\Delta z\mathbf{e}_z) = E_0\exp\left[(ik_0/2)(\chi_R+i\chi_I)\rho(\mathbf{x})\right], \tag{5.6}$$

where $\chi_I = \mathrm{Im}[\chi(\mathbf{r})]$, $\chi_R = \mathrm{Re}[\chi(\mathbf{r})]$, and $\rho(\mathbf{x}) = \int_z^{z+\Delta z}\rho(\mathbf{r})dz$ is the two-dimensional column density. Thus the electric field just after interacting with the atoms is

$$E(\mathbf{x}, z=0^+) = E(\mathbf{x}, z=0^-)e^{-\alpha(\mathbf{x})}e^{i\phi(\mathbf{x})}, \tag{5.7}$$

where $\alpha(\mathbf{x}) = k_0\chi_I\rho(\mathbf{x})/2$ and $\phi(\mathbf{x}) = k_0\chi_R\rho(\mathbf{x})/2$, are the absorption and phase-shift, respectively. The intensity $I = c_0\epsilon_0|E|^2/2$ of the light recorded by a detector is proportional to the square of the electric field amplitude.

For the imaging techniques discussed here, there are generally three images recorded by any given camera: I_j^1 is an image with the atoms present, and I_j^2 is an

image of the probe laser absent the atoms. Then the fraction of the light absorbed by the atoms is

$$f_j = \frac{I_j^1}{I_j^2}, \tag{5.8}$$

where the "j" subscripts indicate that the images are in real space.

Next we describe the absorption and PCI techniques that will be compared to the ORD and MORD methods in Sec. 5.4.3. Following the descriptions of the two frequently used imaging techniques, we will derive the exact solution to the scalar Helmholtz equation for the defocused techniques in Secs. 5.2.3 and 5.2.4.

5.2.2 Absorption and PCI techniques

In a typical imaging system, as depicted in Fig. 5.1, two lenses might be used to focus the image of an object onto a detector. In the Keplerian imaging system in Fig. 5.1, the first lens is positioned a distance f_1 from the object (a BEC), the second lens is placed a distance $f_1 + f_2$ from the first lens, and finally, the detector is placed at the focus of the second lens. The image magnification $M = f_2/f_1$, where f_1, f_2 are the focal lengths of the first and second lens, respectively. This system describes the basis of absorption and phase-contrast imaging described in this manuscript. Next we discuss these two techniques in detail.

The electric field E after propagation through an object modeled under the thin-object approximation may be separated into its unscattered and scattered parts E_0 and ΔE, respectively, so that the total field $E = E_0 + \Delta E$ [44]. In absorption imaging the intensity recorded on the camera $I \propto |E|^2 \propto \exp(-2\alpha)$ so that the

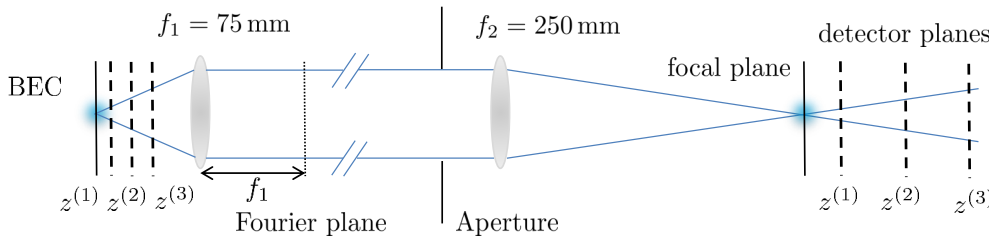

Figure 5.1: A simplified schematic of a two-lens Keplerian imaging system with magnification $M \approx 3$. In absorption and PCI, the detector plane is placed at the focal plane. In MORD, the three detector planes $z^{(i)}$ are located away from the focus. This is equivalent to having three detectors next to BEC, as shown. The imaging resolution is limited by the aperture diameter.

phase information is lost. Using Beer's law, $dI/dz = -\rho(x, y, z)\sigma I$, where σ is the effective scattering cross-section for a two-level atom, the optical depth corrected for the probe detuning and non-negligible intensity, is

$$\mathrm{OD} = -(1 + 4\Delta^2) \ln\left[\frac{I_1 - I_3}{I_2 - I_3}\right] + \frac{I_2 - I_1}{I_{\mathrm{sat}}}. \tag{5.9}$$

For an infinitely thin cloud, $\mathrm{OD} = \sigma_0 \rho(\mathbf{x})$, so that the OD is proportional to the atoms' column density. The second term on the rhs of eqn. (5.9) is negligible in the low intensity limit [47].

Next we discuss PCI. Unlike on-resonance absorption imaging, the recorded intensity of a phase-contrast image contains phase information from which the column density is extracted. PCI is typically implemented by creating a θ phase shift (with optimal signal at $\theta = \pi/2$) to the unscattered probe laser light so that $E_0 \to E_0 \exp(\pm i\pi/2)$. In this way, the phase-shifted light interferes with the light refracted by the atoms, giving an intensity pattern again proportional to the column density [45]. The phase-shift is created by placing a plate with a phase retarding spot slightly larger than the focused beam spot-size into the imaging system (Fig. 5.1).

The spot is placed in the Fourier plane, the plane located a distance f_1 from the first lens, in between the two lenses, where the unscattered probe laser beam comes to a focus. Then the PCI intensity signal is

$$I_{pc} = I_0[2 + e^{-2\alpha} - 2e^{-\alpha}\cos(\phi) + 2e^{-\alpha}\cos(\phi \mp \theta) - 2\cos(\pm\theta)], \tag{5.10}$$

where θ is the phase shift from the phase plate. Next, we choose $\theta = \pi/2$ and make the assumption $\phi \ll 1$ (appropriate for thin dilute clouds). In this case,

$$I_{pc} = I_0(2 + e^{-2\alpha} - 2e^{-\alpha} \pm 2e^{-\alpha}\phi), \tag{5.11}$$

and the intensity is linear in ϕ. The $\pi/2$ phase shift is chosen to maximize this phase signal (for example, for $\theta = \pi$, the Taylor expansion is dominated by nearly all even functions, so that $I \propto \phi^2$. For a far-detuned beam, $\exp(-\alpha) \to 1$, eqn. (5.11) reduces to $I_{pc}/I_0 = [1 \pm 2\exp(-\alpha)\phi]$, and the theoretical model works well for any optical depth. Next we discuss the ORD and MORD methods.

5.2.3 ORD single image reconstruction

We made the paraxial approximation to the electric field which has propagated through an atomic cloud in Sec. 5.1.2. Then, we assumed that the electric field did not diffract as it traveled through the cloud (i.e., that it was thin compared to the depth of field). We introduce additional assumptions about the interaction between the light and atomic, allowing us to derive the ORD imaging technique. Going forward we introduce the Fourier transform of a two-dimensional function $f(\mathbf{x})$ as $\tilde{f}(\mathbf{u}) = \int_{-\infty}^{\infty} f(\mathbf{x})\exp(-2\pi i\mathbf{u}\cdot\mathbf{x})\mathrm{d}\mathbf{x}$, where spatial frequency $u = |\mathbf{u}|$ with $u^2 = u_x^2 + u_y^2$ is related to the wave number k_0 by $u = 2\pi k_0$, where $k_0^2 = k_x^2 + k_y^2 + k_z^2$ is a constant.

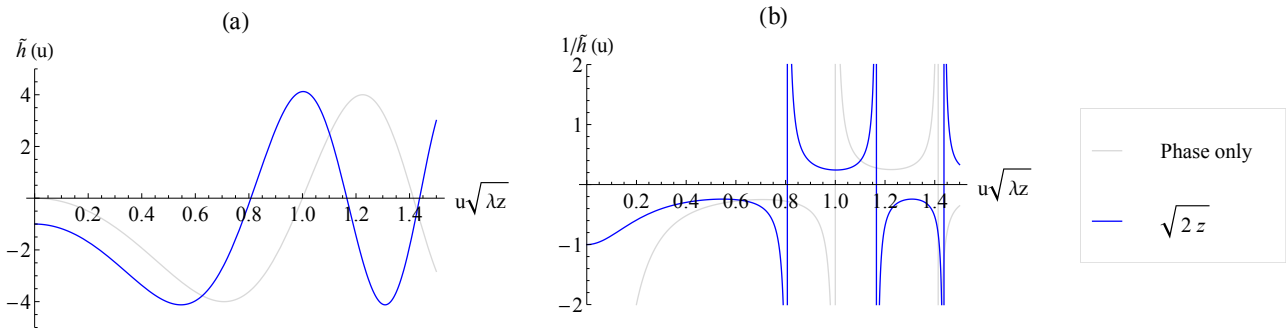

Figure 5.2: (a) The location of the first singularity determines the smallest spatial frequency for which the reconstruction requires regularization. (b) Divergences present in reconstructing the 2D column density.

Re-expressed in terms of $\mathbf{u}$, the paraxial transfer function in free-space (derived in Sec. 5.6) is

$$\tilde{h}_{parax} = \exp(ikz)\exp\left[-i\pi\lambda z(u_x^2 + u_y^2)\right]. \tag{5.12}$$

Using the convolution theorem, we readily obtain the Fresnel diffraction integral:

$$\begin{aligned} E(x,y,z) &= \frac{i}{\lambda z}\exp(ikz)\int_{-\infty}^{\infty} E(x',y',z=0) \\ &\times \exp\left\{\frac{i\pi}{\lambda z}\left[(x-x')^2+(y-y')^2\right]\right\}\mathrm{d}x'\mathrm{d}y'. \end{aligned} \tag{5.13}$$

Now using eqn. (5.13) and the electric field just after it traversed the cloud in eqn. (5.7), we find the normalized Fourier transform of the intensity detected at the camera

$$\begin{aligned} \frac{\tilde{I}(\mathbf{u};z)}{I_0} &= \int_{-\infty}^{\infty}\exp(-\alpha(\mathbf{x}+\lambda z\mathbf{u}/2)-\alpha(\mathbf{x}-\lambda z\mathbf{u}/2) \\ &+ i\phi(\mathbf{x}-\lambda z\mathbf{u}/2)-i\phi(\mathbf{x}+\lambda z\mathbf{u}/2))\times\exp(-2\pi i\mathbf{x}\cdot\mathbf{u})\mathrm{d}\mathbf{x}. \end{aligned} \tag{5.14}$$

Next we add extra assumptions on ϕ and α. We approximate that the phase is slowly-varying: $|\phi(\mathbf{x}+\lambda z\mathbf{u}/2)-\phi(\mathbf{x}-\lambda z\mathbf{u}/2)| \ll 1$, and that absorption is small: $2\alpha(\mathbf{x}) \ll 1$. At lowest order in ϕ and α, the intensity is:

$$\frac{\tilde{I}(\mathbf{u};z)}{I_0} \approx \int_{-\infty}^{\infty}[1-\alpha(\mathbf{x}+\lambda z\mathbf{u}/2)-\alpha(\mathbf{x}-\lambda z\mathbf{u}/2) \tag{5.15}$$
$$+ \; i\phi(\mathbf{x}-\lambda z\mathbf{u}/2)-i\phi(\mathbf{x}+\lambda z\mathbf{u}/2)]\times\exp(-2\pi i\mathbf{x}\cdot\mathbf{u})\mathrm{d}\mathbf{x}\,,$$

which is just a Fourier integral for ϕ and α. Defining the Fourier transforms of ϕ and α as $\widetilde{\phi}$ and $\widetilde{\alpha}$, respectively, we find

$$\frac{\tilde{I}(\mathbf{u};z)}{I_0} = \delta(\mathbf{u}) - 2\widetilde{\alpha}(\mathbf{x})\cos(\pi\lambda z u^2) + 2\widetilde{\phi}(\mathbf{x})\sin(\pi\lambda z u^2). \tag{5.16}$$

Explicitly for the atomic dielectric function, this is

$$\frac{\tilde{I}(\mathbf{u};z)}{I_0} = \frac{-\sigma_0}{1+I_0/I_{\mathrm{sat}}+4\Delta^2}[2\Delta\sin(\pi\lambda z u^2)+\cos(\pi\lambda z u^2)]\tilde{\rho}(\mathbf{u}) \tag{5.17}$$
$$= \tilde{h}(\mathbf{u})\tilde{\rho}(\mathbf{u}), \tag{5.18}$$

where $\tilde{h}(\mathbf{u})$ is the contrast transfer function (CTF) defining a linear relationship between $\tilde{I}/I_0$ and the Fourier transformed calculated column density $\tilde{\rho}(\mathbf{u})$. The example CTF and its inverse, plotted in Fig. 5.2, shows that singularities exist at certain values of the spatial frequencies u, the locations of which are dependent upon the camera postion z and the detuning Δ. The ratio $\chi_I/\chi_R = -1/2\Delta$ determines the quality of information at low spatial frequencies. If $\chi_I/\chi_R > 0$, the phase and absorption terms compete and the inverse CTF diverges. Therefore information is lost in this region. There are two mathematically equivalent cases to achieve the "good" $\chi_I/\chi_R < 0$ condition: $\Delta < 0$ (red detuning) with $z < 0$ (negative defocus), and $\Delta > 0$ (blue detuning) with $z > 0$ (positive defocus). Measurement noise is amplified near the divergences, so that no useful information can be extracted from these frequencies.

Here we qualitatively describe the process of regularization used to mitigate the amplification of noise (or loss of signal) near divergences in the inverse CTF. Regularization limits the extent to which the inverse CTF can diverge in Fourier space. We may also consider the problem in real space. In addition to the image of interest, we assume an image that is spatially uniform (its Fourier components are zero), and take the weighted average of the two images in Fourier space. The spatially uniform image is included only when the signal-to-noise ratio of the reconstructed image in real space would otherwise fall below one. In our MORD method to be discussed in Sec. 5.2.4, we retrieve information at all spatial frequencies relevant to the system (the minimum resolvable frequency is bound by the detector size, and the maximum by the resolution of the imaging system). We do so by using multiple cameras simultaneously to eliminate divergences introduced by any single camera.

5.2.4 Three image reconstruction

We showed in Sec. 5.2.3 that in the single camera (ORD) method, spatial frequencies exist for which we retrieve no information, where $\tilde{h} \to 0$. These spatial frequencies are dependent on z, the displacement of the camera from focus (Fig. 5.3). Thus by adding cameras to the system at different displacements z, we recover information at all spatial frequencies and eliminate the need for regularization. It is appropriate to model shot-noise as additive white noise (i.e. noise that is uncorrelated and uniform over all spatial frequencies). Then the total mean square error

(due to shot-noise) is $\sum_{(i)} |\tilde{h}^{(i)}(\mathbf{u})\tilde{\rho}(\mathbf{u}) - \tilde{f}_k^{(i)}(\mathbf{u})|^2 + |\alpha\tilde{\rho}(\mathbf{u})|^2$, where $i = 1...3$ is the camera number, and the second term is the Tikhonov regularization [48] term with regularization constant α. The mean square error is minimized when

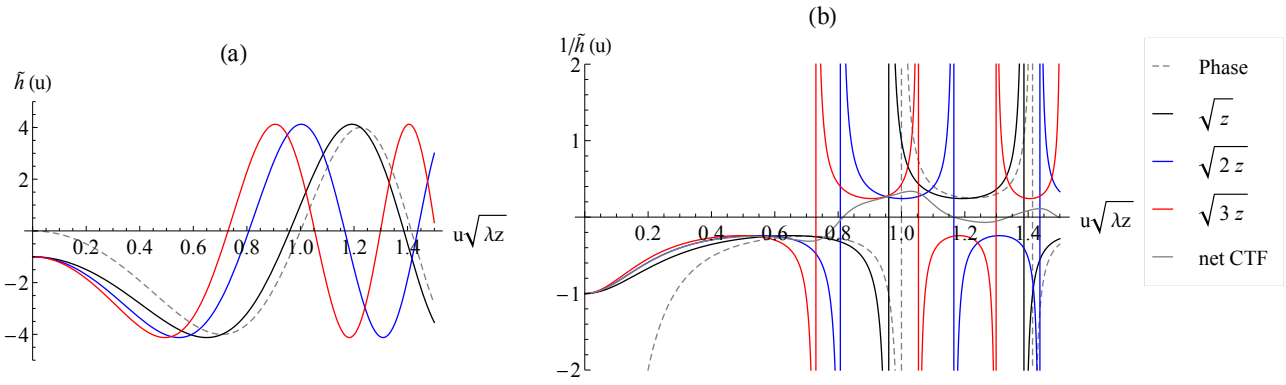

Figure 5.3: contrast transfer functions (CTFs) for three different detector positions. By picking appropriate z values, contrast information may be retrieved for all spatial frequencies u. In (b), the individual inverse CTFs are plotted, along with the combined CTF.

$$\tilde{\rho}(\mathbf{u}) = \frac{\sum_{(i)} \tilde{h}^{(i)}(\mathbf{u})\tilde{f}_k^{(i)}(\mathbf{u})}{\sum_{(i)} |\tilde{h}^{(i)}(\mathbf{u})|^2 + \alpha^2}. \tag{5.19}$$

If singularities have no overlap, α may be set to zero, and the calculted column density is effectively minimized by the weighted average of the three images in Fourier space. Eqn. (5.19) models shot-noise as additive white-noise, and assumes $\tilde{\rho}(\mathbf{u})$ and the shot-noise are uncorrelated. The above equation is an exact solution to the scalar wave equation without singularities (as long as the displacements $z^{(i)}$ of the cameras are chosen without overlapping divergences.) Next we discuss the physical implementation of this method.

5.3 Experimental techniques

5.3.1 Physical set-up

We implemented the MORD technique using a two-lens imaging system with magnification $M \approx 3$ (as shown in Fig. 5.1), and placed three detectors at different distances from the focal plane. The system consisted of a pair of 25.4 mm diameter lenses with focal lengths $f_1 = 75$ mm and $f_2 = 250$ mm separated by 325(10) mm. Then the magnification along the beam propagation direction was M^{-2}, and the effective distance away of a camera from focus was $\Delta z_{eff} = \Delta z/M^2$. An aperature with a 18(1) mm diameter in the Fourier plane blocked image distortions arising from the 25 mm dichroic mirror used in the imaging system periscope. The imaging system had an effective numerical aperture NA ≈ 0.12, and an effective resolution of ≈ 8 μm. After the final lens, the light was directed to our three detectors using non-polarizing beam splitters (BSs) with reflection to transmission (R:T) ratios 70:30 and 50:50 to split the probe into three beams with nominally equal powers (Fig. 5.4). We detected each probe light on a charge-coupled device (CCD) camera with detector size 648×488 square pixels with pixel width 5.6 μm. Each camera was on a translation stage, so that the set-up could be used for both the defocused and standard absorption imaging methods. The three cameras shared a triggering pulse for simultaneous image capture.

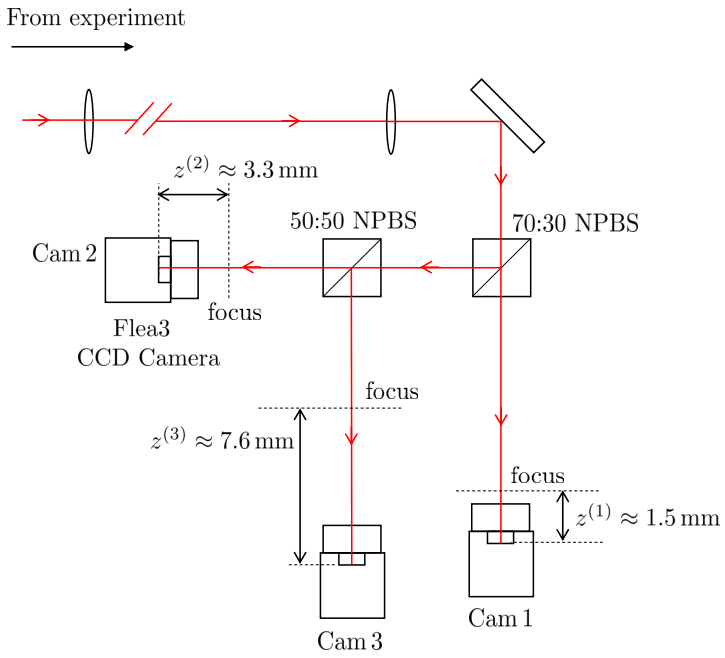

Figure 5.4: Schematic of our MORD setup. The two-lens imaging system described by Fig. 5.1 is implemented with two non-polarizing beam splitters that nominally split the probe laser beam into three equal intensities. Each image is then recorded by its designated camera. Each camera takes a defocused image at position $z^{(i)}$ from focus.

5.3.2 Experimental procedure

Here we describe the experimental procedure used to acquire the images for the MORD technique. We collected about 1×10^9 ^{87}Rb atoms in a vapor-fed six-beam magneto-optical trap, performed sub-Doppler cooling, and then trapped the atoms in the $|f = 2, m_F = 2\rangle$ state in a spherical quadrupole trap. We then used magnetic transport [49] to move the resulting cloud about 42 cm vertically in 2.2 s, giving an ensemble at ≈ 120 μK with about 1×10^8 atoms. We then evaporated to degeneracy in the combined magnetic/optical technique described in Ref. [34]. During

evaporation, we performed a microwave transfer between the ground hyperfine states $|f = 2, m_F = 2\rangle$ to $|f = 1, m_F = -1\rangle$, giving 100×10^3 atom Bose-Einstein condensates (BECs) in a cross-optical dipole trap every 15 s in the $|f = 1, m_F = -1\rangle$ state. The BEC was trapped in a crossed-dipole trap with frequencies $\approx$ 110Hz, 75Hz, and 50Hz along $\mathbf{e}_x$,$\mathbf{e}_y$, and $\mathbf{e}_z$ respectively. To achieve the desired optical depth to test our imaging technique, we then performed a partial $\approx$ 10 % transfer to the $|f = 2, m_F = 1\rangle$ state with a short ($\ll \pi/2$) microwave pulse [50]. We then used a probe beam detuned $\Delta = 2\Gamma$ from the $f = 2$ to $f' = 3$ cycling transition without repump to image the transferred $N \approx 1 \times 10^4$ atoms after a 6 ms TOF with the three cameras simultaneously. The probe intensity $I \approx 2.5 I_{\rm sat}$, where the saturation intensity $I_{\rm sat} \approx 3.5 {\rm mW/cm}^2$ [51] for a circularly polarized probe beam.

In the defocused technique, the intensity I_j^1 in eqn. (5.8) is the off-resonant, defocused absorption image of the atoms. Additionally, a third image I_j^3 is taken with neither the atoms nor the probe laser light. This background image is subtracted from I_j^1 and I_j^2 to remove any dark counts from the detector.

5.4 Measurement and analysis

5.4.1 Experimental data

Fig. 5.5(a) shows the raw data recorded by each camera using the experimental techniques described in Sec. 5.3. We prepare the raw data by applying a Fermi mask to get rid of probe artifacts present at the detector edges (Fig. 5.5(b)). To compare the ORD and MORD imaging techniques, we show the single-camera ORD

results in Fig. 5.5(c), and the two- and three-camera MORD reconstructed results in Fig. 5.5(d). The background of the MORD method has visibly fewer artifacts than the ORD reconstructed images.

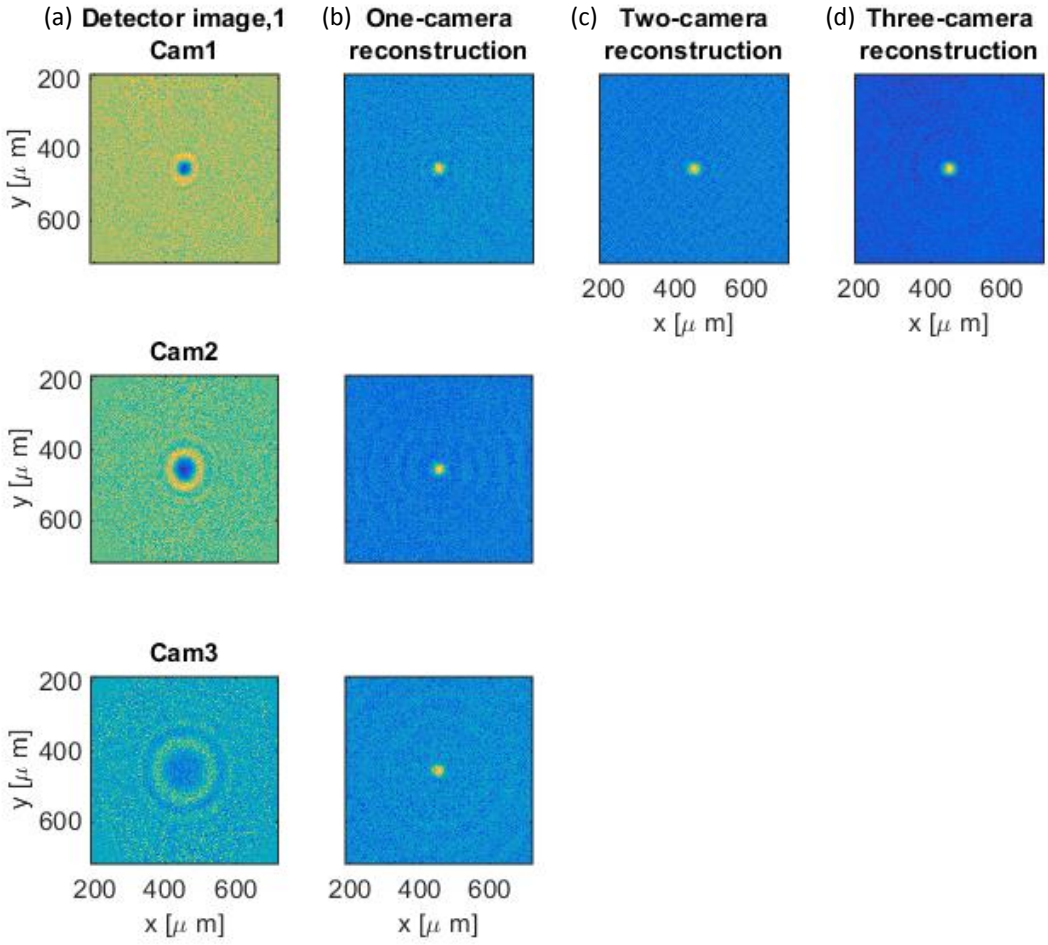

Figure 5.5: Set of images taken by the three cameras: (a) the raw data, after applying a Fermi mask to get rid of artifacts at the edges which do not contain density information but contributes to noise, (b) individual single-image ORD reconstructions for each camera, (c) a two-camera reconstruction, and (d) the three-camera MORD reconstruction. The "rings" present in the ORD method are less prevalent in the MORD technique.

5.4.2 Systematics in the MORD method

Next we consider the following sources of systematic uncertainties in the calculated column density of the MORD method: the theoretical model eqn. (5.19) as shown in Fig. 5.6, the uncertainties in camera positions $z^{(i)}$ (Fig. 5.7), and the quality of the $\mathbf{e}_x - \mathbf{e}_y$ registration of the three images during reconstruction. We then compare the statistical uncertainties of the three-camera method to those of absorption imaging and PCI. We show that except for the on-resonance case, the MORD imaging technique gives smaller uncertainties than absorption imaging at the same detuning. Further, the MORD method has slightly larger but comparable uncertainties to PCI for large detunings, and smaller uncertainties for small detunings where PCI uncertainty diverges.

In our simulations, the SSFM (see Sec. 5.6) was used to propagate the electric field through the atomic cloud. Fig. 5.6(a),(b) show the systematic fractional uncertainties in the reconstructed OD for different probe detunings. Fig. 5.6(c) gives the uncertainty for different probe intensities, plotted for a range of OD values. Further, in Fig. 5.7, we vary the $z^{(i)}$ values from the actual, forward propagated distances: by adding an offset to the $z^{(i)}$ used in the reconstruction, we find $\Delta\rho/\rho_0$ associated with the uncertainties in the $z^{(i)}$ positions of the three cameras that we measured in experiment. The uncertainties stay small for any single camera that is offset by up to several millimeters. Next we discuss the statistical uncertainties of MORD, absorption, and phase-contrast imaging techniques.

5.4.3 Uncertainties and comparisons to other imaging techniques

We take detector shot noise to be the only source of statistical uncertainty, and neglect the read noise of the camera. The shot-noise of an image is given by $\sqrt{\mathcal{N}}$, where $\mathcal{N} = |E|^2(\Delta x)^2 dt/\hbar\omega$ is the number of incident photons on the detector, with the intensity recorded $|E|^2$, pixel width Δx, laser beam frequency ω, and imaging pulse-length dt. The statistical uncertainty in the calculated column density is found by propagating the noise in the fractional uncertainty of f_j^0 (eqn. (5.8)) through each step of the density calculation. We start with the squared noise in real space

$$(\delta f_j^0)^2 = \sum_n \left(\frac{\partial f_j^0}{\partial \mathcal{N}_j^n}\right)^2 (\delta \mathcal{N}_j^n)^2, \text{where shot noise } \delta\mathcal{N}_j^n = \sqrt{\mathcal{N}_j^n}, \tag{5.20}$$

and $n = 1...3$ is the image number. In experiment, the intensity at the camera is recorded as photoelectron counts by the camera, which is proportional to $\mathcal{N}$. In eqn. (5.20), $\mathcal{N}_j^n$ represents the number of photons. For the background image, $\delta\mathcal{N}_3 = 0$. As stated in Sec. 5.3.2, a uniform probe propagates through free space to the atoms. After the probe interacts with the atoms, it propagates a distance Δz in free space. Since in experiment we use non-polarizing beamsplitters to split the probe intensity into three beams, the intensity detected at each camera is one-third the original intensity. Shot-noise was simulated at the detector under these conditions. In the next step towards column-density retrieval, we take the Fourier transform of the fractional intensity (eqn. (5.8)):

$$\tilde{f}_k = \frac{1}{\sqrt{N}} \sum_j e^{-ikj} f_j, \text{ where } N = \text{ the number of pixels.} \tag{5.21}$$

Next, in the ORD method, the transformed image is multiplied to the single transfer function $\tilde{h}_k$ associated with the detector: $\tilde{f}'_k = \tilde{f}_k \tilde{h}_k$. In the MORD method considered here, we take the weighted average (as implemented in eqn. (5.19)) of all the images with their corresponding transfer functions:

$$\tilde{f}'_k = \frac{\sum_{(i)} \tilde{h}^{(i)} \tilde{f}^{(i)}_k}{\sum_{(i)} |\tilde{h}^{(i)}|^2} = \sum_{(i)} \tilde{h}'^{(i)} \tilde{f}^{(i)}_k, \text{ where } \tilde{h}'^{(i)} = \frac{\tilde{h}^{(i)}}{\sum_{(i)} |\tilde{h}^{(i)}|^2} \tag{5.22}$$

and $C_k \equiv \sum_{(i)} |\tilde{h}^{(i)}|^2$ is a constant. The column density of the atomic cloud is found by taking the inverse Fourier transform of $\tilde{f}'_k$:

$$\tilde{f}'_j = \frac{1}{\sqrt{N}} \sum_k e^{ikj} \tilde{f}'_k = \frac{1}{\sqrt{N}} \sum_k e^{ikj} \sum_{(i)} \tilde{h}'^{(i)} \tilde{f}^{(i)}_k \tag{5.23}$$

$$= \frac{1}{\sqrt{N}} \sum_{(i)} \sum_{j'} \left[\frac{1}{\sqrt{N}} \sum_k e^{ik(j-j')} \tilde{h}'^i_k \right] f^{(i)}_{j'} = \frac{1}{\sqrt{N}} \sum_{(i)} \sum_{j'} H^{(i)}_{j-j'} f^{(i)}_{j'} \tag{5.24}$$

where $H^{(i)}_{j-j'} = (1/\sqrt{N}) \sum_k \exp[ik(j-j')] \tilde{h}'^i_k$.

Then the final total squared uncertainty sums over all cameras $i = 1...3$:

$$(\delta f'_j)^2 = \frac{1}{n} \sum_{(i)=1}^{n} \sum_{j'} \left(\frac{\partial f'_j}{\partial f^{(i)}_{j'}} \right)^2 (\delta f^{(i)}_{j'})^2 = \frac{1}{N} \sum_i \sum_{j'} (H^{(i)}_{j-j'})^2 (\delta f^{(i)}_{j'})^2, \tag{5.25}$$

where n is the total number of cameras. We would like to compare this result to the uncertainties in the absorption and PCI methods. Using the formalism described by eqn. (5.20), we find the squared uncertainty for absorption imaging using eqn. (5.9):

$$(\delta \mathrm{OD})^2 = \left[\frac{1 + 4\Delta^2}{\mathcal{N}_1} + \frac{1}{\mathcal{N}_{\mathrm{sat}}} \right]^2 \mathcal{N}_1 + \left[\frac{1 + 4\Delta^2}{\mathcal{N}_2} + \frac{1}{\mathcal{N}_{\mathrm{sat}}} \right]^2 \mathcal{N}_2. \tag{5.26}$$

Next, we find that the uncertainty in the OD for PCI using eqn. (5.11) to be

$$(\delta \mathrm{OD})^2 = \left[\frac{1 + \mathcal{N}_1/\mathcal{N}_{\mathrm{sat}} + 4\Delta^2}{2\Delta} \frac{1}{\mathcal{N}_2} + \frac{1}{2\Delta \mathcal{N}_{\mathrm{sat}}} \left(\frac{\mathcal{N}_1}{\mathcal{N}_2} - 1 \right) \right]^2 \mathcal{N}_1 \tag{5.27}$$

$$+ \left[\frac{1 + \mathcal{N}_1/\mathcal{N}_{\mathrm{sat}} + 4\Delta^2}{2\Delta} \right]^2 \frac{\mathcal{N}_1^2}{\mathcal{N}_2^3}.$$

The statistical fractional uncertainties as a function of probe detuning is plotted in Fig. 5.8 for MORD, absorption, and PCI methods, using eqns. (5.25), (5.26), and (5.27), respectively.

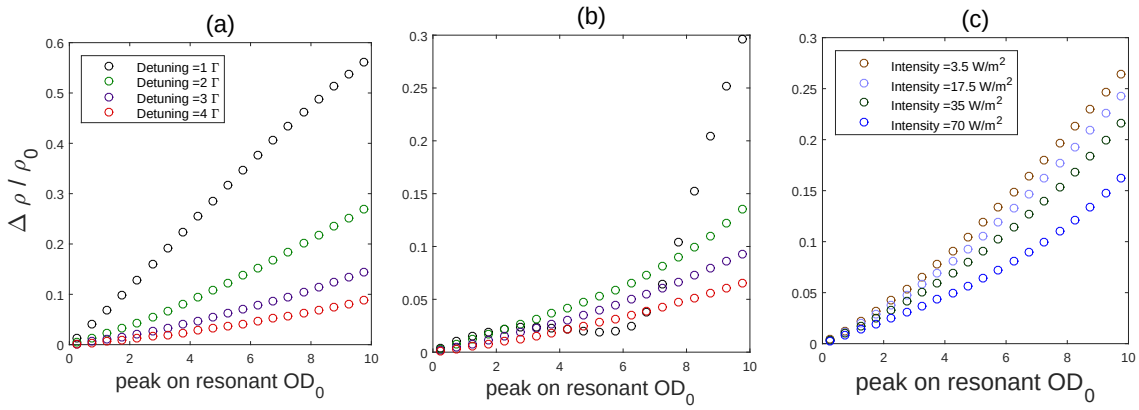

Figure 5.6: MORD systematic fractional uncertainties in the calculated OD and its dependence on detuning using the low intensity approximation in the reconstruction (a), using the intensity in our experiment (b), and the uncertainty dependence on probe intensity (c).

5.5 Conclusion

We have demonstrated improvement in the single-camera ORD technique by using three cameras simultaneously to eliminate the divergences that arise in the contrast-transfer function. We studied the systematic uncertainties of the MORD method, and theoretically compared multiple techniques using simulated data treated in equal footing. We showed that the MORD method is comparable to PCI. Therefore, in experiment, the easier to implement MORD set-up may be preferable to PCI.

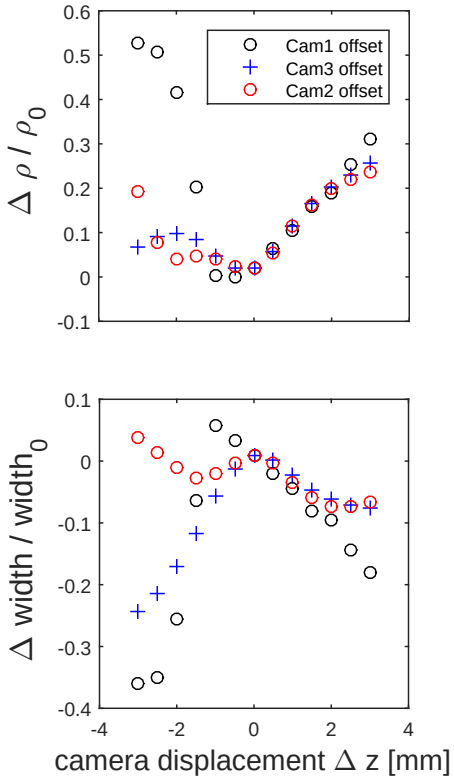

Figure 5.7: Added camera displacement Δz to each camera (independently, and not at the same time). The offset is used in the reconstruction (not in the forward z). Fractional uncertainty in OD vs. Δz (top), reconstructed width vs Δz (bottom).

5.6 Methods

A free space solution to eqn. (5.1) is a plane wave of the form $E(x,y,z) = \exp[i(k_x x + k_y y + k_z z)]$ for $k_0^2 = k_x^2 + k_y^2 + k_z^2$. For a probe beam propagating along $\mathbf{e}_z$, we may re-express the electric field as

$$E(\mathbf{r}) = \exp\left[i\left(k_x x + k_y y + z\sqrt{k_0^2 - k_x^2 - k_y^2}\right)\right] \tag{5.28}$$

$$= E(\mathbf{r}; z=0)\exp(iz\sqrt{k_0^2 - k_{2\mathrm{D}}^2}), \tag{5.29}$$

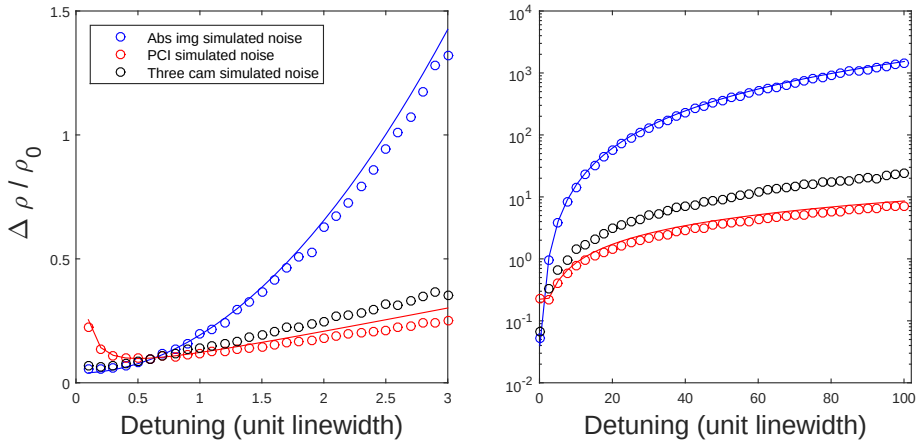

Figure 5.8: Systematic uncertainties of simulated data, for absorption imaging (blue), phase-contrast imaging (red), and MORD (back). The simulated data and analytical solutions are shown as circles and solid lines, respectively.

where $E(\mathbf{r}; z = 0) = \exp(i\mathbf{k}_{2D} \cdot \mathbf{r}_{2D})$. The propagation behavior of the electric field has two regions: when $k_0^2 > k_x^2 + k_y^2$, $E(\mathbf{r})$ propagates sinusoidally, and for $k_0^2 < k_x^2 + k_y^2$, the field decays exponentially (is an evanescent wave).

The general free space solution to eqn. (5.1) is given by the weighted sum over all possible values of $\mathbf{k}_{2D}$:

$$E(\mathbf{r} + \Delta z \mathbf{e}_z) = \int_{-\infty}^{\infty} \exp\left(i\Delta z \sqrt{k_0^2 - k_{2D}^2}\right) \widetilde{E}(\mathbf{k}_{2D}) \exp(i\mathbf{k}_{2D} \cdot \mathbf{r}_{2D}) d\mathbf{k}_{2D} \,, \tag{5.30}$$

known as the angular spectrum representation, where the exact free space transfer function

$$\widetilde{\mathbf{P}}(\mathbf{k}_{2D}, \Delta z) = \exp\left(i\Delta z \sqrt{k_0^2 - k_{2D}^2}\right) \tag{5.31}$$

propagates the original field $E(\mathbf{r}; z = 0)$ by distance Δz. The free-space propagator under the parxial approximation is

$$\widetilde{\mathbf{P}}'(\mathbf{k}_{2D}, \Delta z) = \exp\left(-i\Delta z \frac{k_{2D}^2}{2k_0^2}\right). \tag{5.32}$$

For propagation through an infinitely thin medium, the propagator

$$\mathbf{Q}(\Delta z) = \exp\left[ik_0 \int_z^{z+\Delta z} \sqrt{\chi(\mathbf{r})}\, dz\right]. \tag{5.33}$$

If the medium is a thin dilute cloud for which the paraxial approximation applies (eqns.(5.32),(5.5)), there exists a numerical solution to the paraxial wave equation (eqn. (5.4)) using the split-step Fourier method (SSFM):

$$E(\mathbf{r} + \Delta z \mathbf{e}_z) = P'(\Delta z/2)Q'(\Delta z)P'(\Delta z/2)E(\mathbf{r}). \tag{5.34}$$

where $E(\mathbf{r} + \Delta z \mathbf{e}_z)$ is the electric field that propagated a step Δz. The SSFM given by eqn. (5.34) is iterated through the thickness of the cloud. Correction to the SSFM starts at third order in Δz [52].

Chapter 6: Conclusion and Outlook

During my tenure at NIST, the light-induced gauge fields laboratory has made stunning progress in the field. The lab has gone from the production of a BEC in a new apparatus, to the first demonstration of an artificial gauge field, and most recently, the current team members of this lab visualized skipping orbits in the quantum Hall regime. Synthetic gauge fields are an appealing field because of their applicability to a wide range of disciplines, from condensed matter experiments, topological materials, theoretical proposals beyond real materials, to high energy physics.

Going forward, there are crucial milestones that could be realized with gauge fields, such as observing fractional quantum Hall states in real space, and the realization of flux lattices, perhaps enabled by alkaline earth [53] or lanthanide [54] quantum gases.

With our new atom-chip apparatus, we performed an off-resonance defocused imaging experiment with multiple cameras to reconstruct the OD of BECs with comparable results to PCI. While the results are comparable, the physical implementation of the MORD technique in the laboratory is relatively simple and offers potential advantages over PCI. While absorption imaging is a workhorse technique,

it is satisfying to demonstrate a technique with improved fundamental limits (relative to ORD), with the prospect of enabling new experiments. The MORD may have applications in extended atomic systems that require both high resolution imaging and wide field of view without spatial divergences, such as continuous atom lasers and atomic ring gyroscopes. Going beyond MORD, it is possible to reconstruct the phase and amplitude of the electromagnetic field using simultaneous multi-camera images which may allow for holographic reconstruction of the 3D atomic density.

Our newly constructed atom-chip apparatus could realize the first demonstration of an artificial gauge field without spontaneous emission. FPGA programming of individual nanofabricated wires will allow the creation of exotic arbitrary potentials. Once rf "Raman" is successfully demonstrated with ^{87}Rb, ^{6}L can be introduced into the system, setting up for even more exotic phenomena with Fermionic systems.

Appendix A: Atom-light interaction

A.1 An Atom in the Presence of an External Magnetic Field

The Hamiltonian of an atom interacting with an external magnetic field is

$$\hat{H} = A_{hf}\mathbf{I}\cdot\mathbf{J} - \boldsymbol{\mu}\cdot\mathbf{B}. \tag{A.1}$$

The nucleus has an intrinsic magnetic moment $\boldsymbol{\mu}_I = -g_I\mu_B\mathbf{I}$. The $\mathbf{I}\cdot\mathbf{J}$ term arises from the interaction between the dipolar electromagnetic field emanating from the nucleus, and the electron's intrinsic electric dipole moment $\boldsymbol{\mu}_J = -g_J\mu_B\mathbf{J}$ (where $\mathbf{J} = \mathbf{L} + \mathbf{S}$ and we assume $\mathbf{L} = 0$). This interaction gives rise to the hyperfine structure, and at zero external magnetic field, the size of the hyperfine splitting is proportional to the hyperfine constant A_{hf}. The Zeeman interaction term $-\boldsymbol{\mu}\cdot\mathbf{B}$ arises from the interaction between the atom's total magnetic moment $\boldsymbol{\mu}$, and the external magnetic field $\mathbf{B} = B_0\hat{e}_z$. The total magnetic moment $\boldsymbol{\mu}$ comprises both $\boldsymbol{\mu}_J$ and $\boldsymbol{\mu}_I$: $\boldsymbol{\mu} = \boldsymbol{\mu}_J + \boldsymbol{\mu}_I = -\mu_B(g_J\mathbf{S} + g_I\mathbf{I})$.

If the applied field is weak, the hyperfine interaction dominates and good quantum numbers are F, and m_F. However if the field is very strong, the hyperfine interaction is negligible and $\mathbf{I}$ and $\mathbf{J}$ are effectively uncoupled and separately conserved. Then good quantum numbers become $|J, m_J; I, m_I\rangle$. Next we consider in

detail the Hamiltonian in the region between these two cases. In the medium-field region, we must consider the combination of $|F, m_F\rangle$ and $|J, m_J; I, m_I\rangle$ states.

A.2 Arbitrary field strength interaction

The Hamiltonian re-written in terms of raising and lowering operators is

$$\hat{H} = A_{hf} I_z J_z + \frac{A_{hf}}{2}(J_+ I_- - J_- I_+) + \mu_B B_0 (g_J S_z + g_I I_z), \tag{A.2}$$

where $J_\pm = J_x \pm i J_y$, similarly for $I_\pm$. The Hamiltonian can be solved exactly for $J = 1/2$, applicable to the ground states of all alkalis ($L = 0, S = 1/2$). In this case, $m_J = \pm 1/2$, so the interaction only couples two sets of states $|m_J, m_I = m_F - m_J\rangle$:

$$|m_J = \pm 1/2, m_I = m_F \mp 1/2\rangle,$$

where $m_F = m_J + m_I$ is conserved for all magnetic fields. Since

$$J_\pm |J, m_J\rangle = \sqrt{(J \mp m_J)(J \pm m_J + 1)}\,|J, m_J \pm 1\rangle, \tag{A.3}$$

the terms in the Hamiltonian involving the ladder operators couple the two m_J states. The matrix elements of the Hamiltonian is

$$\begin{aligned}
\langle m_J = \pm 1/2|\hat{H}|m_J = \pm 1/2\rangle &= -A_{hf}\left(\frac{1}{4} \mp m_F\right) + \mu_B B_0 \left(g_I m_F \pm \frac{1}{2}(g_J - g_I)\right) \\
\langle m_J = \pm 1/2|\hat{H}|m_J = \mp 1/2\rangle &= \frac{A_{hf}}{2}\sqrt{\left(I + \frac{1}{2}\right)^2 - m_F^2}.
\end{aligned} \tag{A.4}$$

Diagonalization of the Hamiltonian results in the eigenvalues given by the Breit-Rabi formula [55]

$$E_\pm = -\frac{A_{hf}}{4} + g_I \mu_B m_F B_0 \pm \frac{A_{hf}}{2}\left(I + \frac{1}{2}\right)\sqrt{1 + \frac{2m_F}{I + \frac{1}{2}}x + x^2}, \tag{A.5}$$

where

$$x = \frac{\mu_B B_0}{A_{hf}} \frac{(g_J - g_I)}{(I + \frac{1}{2})}. \tag{A.6}$$

A.3 Time-Dependent Perturbation in the Weak-Field Limit

Next we consider the interaction with a time-varying magnetic field

$$\mathbf{B} = \mathbf{B}_0 + \mathbf{B}_{rf}\cos(\omega_{rf}t). \tag{A.7}$$

The bias field $\mathbf{B}_0 = \mathrm{B}_0\mathbf{e}_z$, the oscillating field $\mathbf{B}_{rf}\cos(\omega_{rf}t) = B_{rf}\cos(\omega_{rf}t)\mathbf{e}_x$, and $|\mathrm{B}_{rf}| \ll |\mathrm{B}_0|$. Since $\boldsymbol{\mu}_J \gg \boldsymbol{\mu}_I$, we neglect $\boldsymbol{\mu}_I$ and re-express the Zeeman interaction Hamiltonian as $\hat{H} = \boldsymbol{\mu}_J \cdot \mathbf{B} = g_J\mu_B\mathbf{S}\cdot\mathbf{B} = g_J\mu_B\mathbf{J}\cdot\mathbf{B}$ for $L = 0$. Since $\mathbf{F}$ is the good quantum number in the region of small fields, we write the Hamiltonian in terms of the projection of $\mathbf{J}$ on $\mathbf{F}$. Both a classical vector model and a quantum mechanical approach using the projection theorem (in which the theorem is applied to each vector component of $\mathbf{J}$) show that the Hamiltonian may be reexpressed as

$$\begin{aligned}
\hat{H} &= g_J\mu_B \frac{\langle \mathbf{J}\cdot\mathbf{F}\rangle}{F(F+1)}\mathbf{F}\cdot\mathbf{B} \\
&= g_F\mu_B\mathbf{F}\cdot\mathbf{B} \\
&= g_F\mu_B F_z B_0 + g_F\mu_B F_x B_{rf}\cos(\omega_{rf}t) \\
&= \omega F_z + \Omega F_x\cos(\omega_{rf}t) \\
&= \hat{H}_0 + \hat{H}',
\end{aligned} \tag{A.8}$$

Where $\omega \equiv g_F\mu_B B_0$, $\Omega \equiv g_F\mu_B B_{rf}$. Without $\mathbf{B}_{rf}$, to first-order the Zeeman shift is the familiar $E^{(1)} = \langle\hat{H}\rangle = g_F\mu_B m_F B_0$, and the energy splitting scales linearly with the magnetic field.

We want to eliminate the time dependence by going into the rotating frame with the unitary time-evolution operator $U(t) = e^{i\omega' t F_z/\hbar}$, so that the state ket in the rotating frame $|\Psi'\rangle = U(t)|\Psi\rangle$. Then the Schrödinger equation for the state ket rotating at frequency ω' about F_z is

$$\begin{aligned}
i\hbar\frac{\partial|\Psi'\rangle}{\partial t} &= i\hbar\frac{\partial}{\partial t}\left(U(t)|\Psi\rangle\right) \\
&= i\hbar U(t)\frac{\partial}{\partial t}|\Psi\rangle + i\hbar\left(\frac{\partial U(t)}{\partial t}\right)U(t)|\Psi\rangle \\
&= U(t)\hat{H}U^{\dagger}(t)U(t)|\Psi\rangle - \omega' F_z|\Psi'\rangle \\
&= [U(t)\hat{H}_0 U^{\dagger}(t) + U(t)\hat{H}'U^{\dagger}(t) - \omega' F_z]|\Psi'\rangle \\
&= [(\omega - \omega')F_z + U(t)\hat{H}'U^{\dagger}(t)]|\Psi'\rangle \\
&= \hat{H}_{rot}|\Psi'\rangle
\end{aligned}$$

where $\hat{H}_{rot}$ is the Hamiltonian in the rotating frame. Since in the $|\psi\rangle \doteq (m_F = 1, m_F = 0, m_F = -1)$basis,

$$U(t) = e^{i\omega' t F_z/\hbar} = \begin{pmatrix} e^{i\omega' t} & 0 & 0 \\ 0 & 1 & 0 \\ 0 & 0 & e^{-i\omega' t} \end{pmatrix}$$

we find that $U(t)\hat{H}'U^{\dagger}(t)$

$$= \frac{1}{2}\begin{pmatrix} 0 & e^{i(\omega_{rf}+\omega')t} + e^{-i(\omega_{rf}-\omega')t} & 0 \\ e^{i(\omega_{rf}-\omega')t} + e^{-i(\omega_{rf}+\omega')t} & 0 & e^{i(\omega_{rf}+\omega')t} + e^{-i(\omega_{rf}-\omega')t} \\ 0 & e^{i(\omega_{rf}-\omega')t} + e^{-i(\omega_{rf}+\omega')t} & 0 \end{pmatrix}.$$

If we let $\omega' = \omega_{rf}$, and make the RWA by dropping the terms that oscillate at $2\omega_{rf}$, $U(t)\hat{H}'U^{\dagger}(t) = \Omega F_x/2$, so the Hamiltonian is time-independent in the rotating frame. The full Hamiltonian is then

$$U(t)\hat{H}'U^{\dagger}(t) = \begin{pmatrix} \delta & \Omega/2 & 0 \\ \Omega/2 & 0 & \Omega/2 \\ 0 & \Omega/2 & -\delta \end{pmatrix} \tag{A.9}$$

where $\delta = \omega - \omega_{rf}$.

Appendix B: Machine drawings

Here we include the Science cell design in B.1. We then present the drawings for the machined parts that make up the magnetic transport system. Figs. B.2, B.3, B.4, and B.5 are coil holders designed to fit around the outer diameter of coils. Examples of mounted coils are shown in Fig. 4.11. Fig. B.6 is the spacer placed in between the final coil and the cold plate (Fig. B.10), and similarly, Fig. B.7 is the MOT coil spacer. The cage adaptors referred to in Fig. 4.13 are shown as drawings in Figs. B.8, B.9.

Further, Figs. B.11, B.12, and B.13 are coil winding forms. They also functioned as coil holders when excess Kapton tape was faced off the coils surfaces using a lathe. Moreover, Fig. B.14 is the cooling tube clamp which fixes the copper cooling tubes onto the cooling towers, and Fig. B.15 is the MOT cell holder design, as seen in Fig. 4.4.

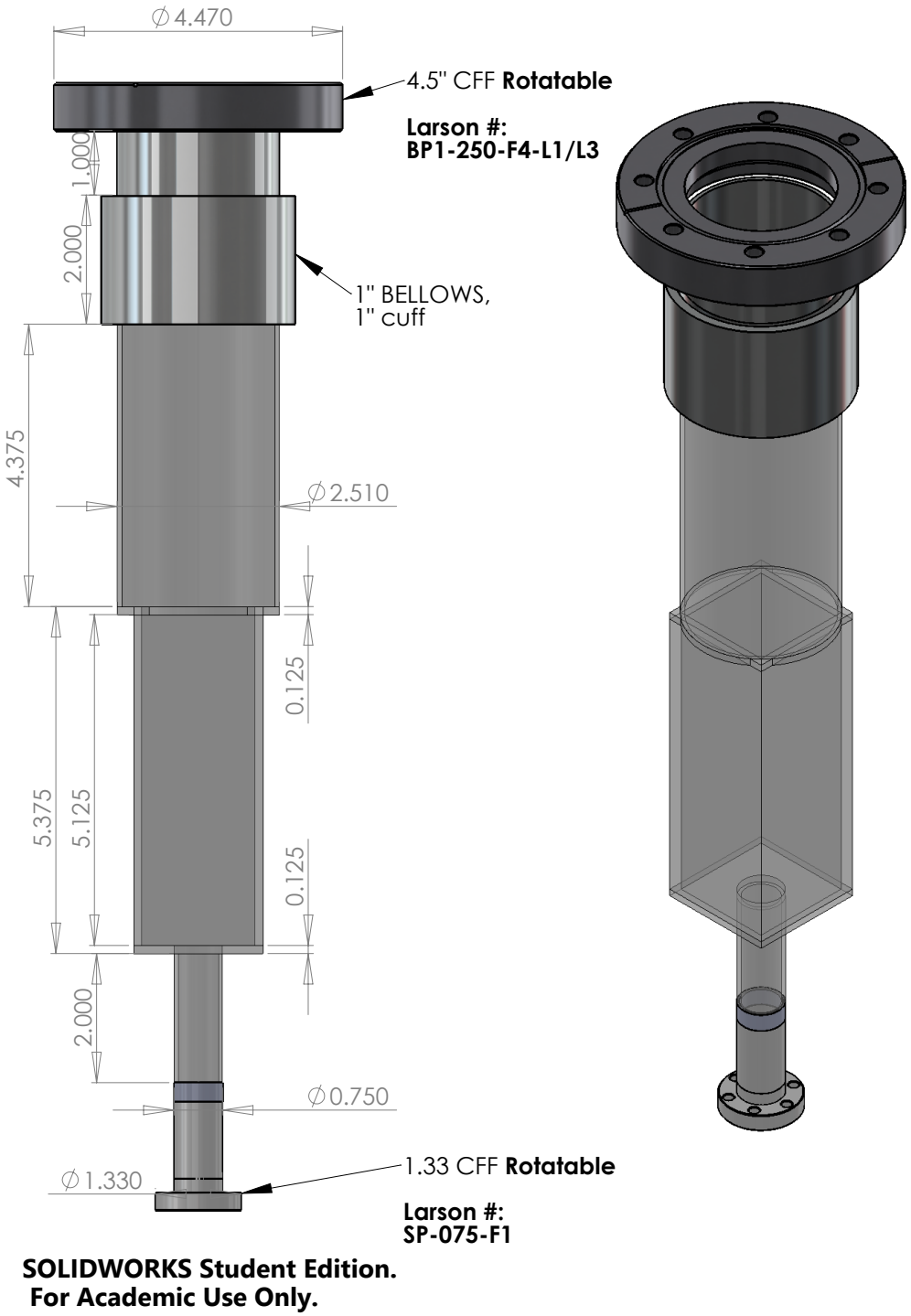

Figure B.1: Science cell

Figure B.2: "Bottom" Coil, holder

Figure B.3: "Top" Coil, holder

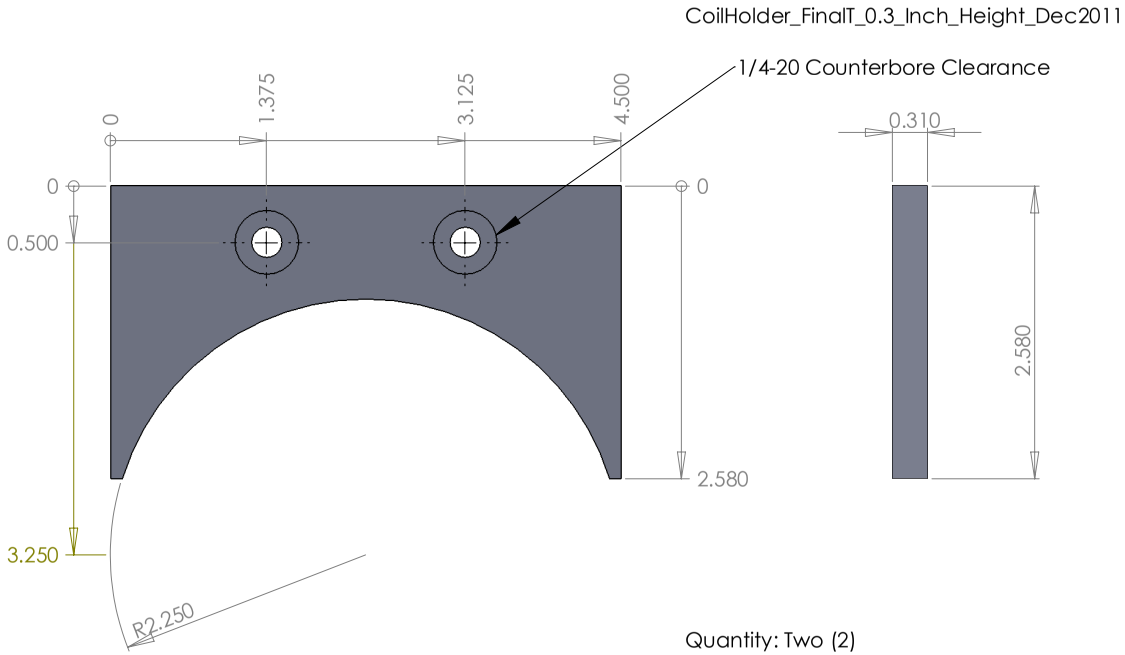

Figure B.4: Final coil, holder

Figure B.5: MOT coil, holder

Figure B.6: Final coil spacer

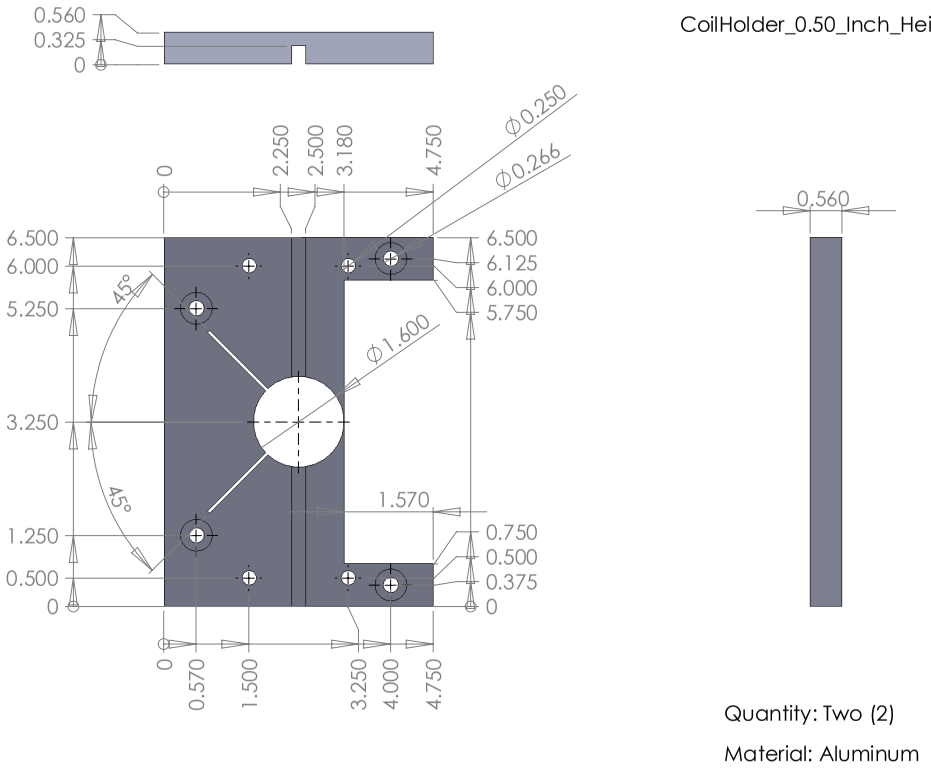

Figure B.7: MOT coil spacer

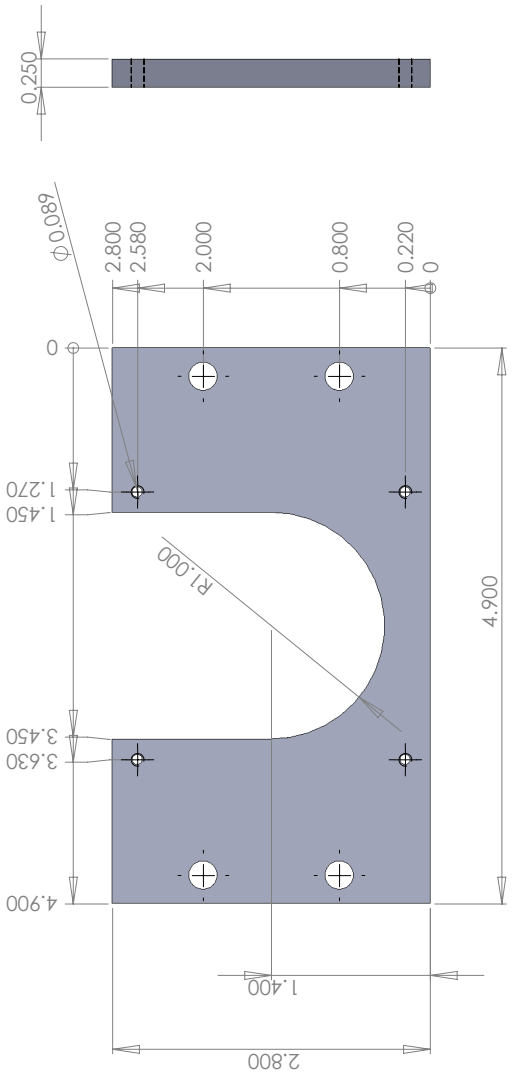

Figure B.8: Cage adapter

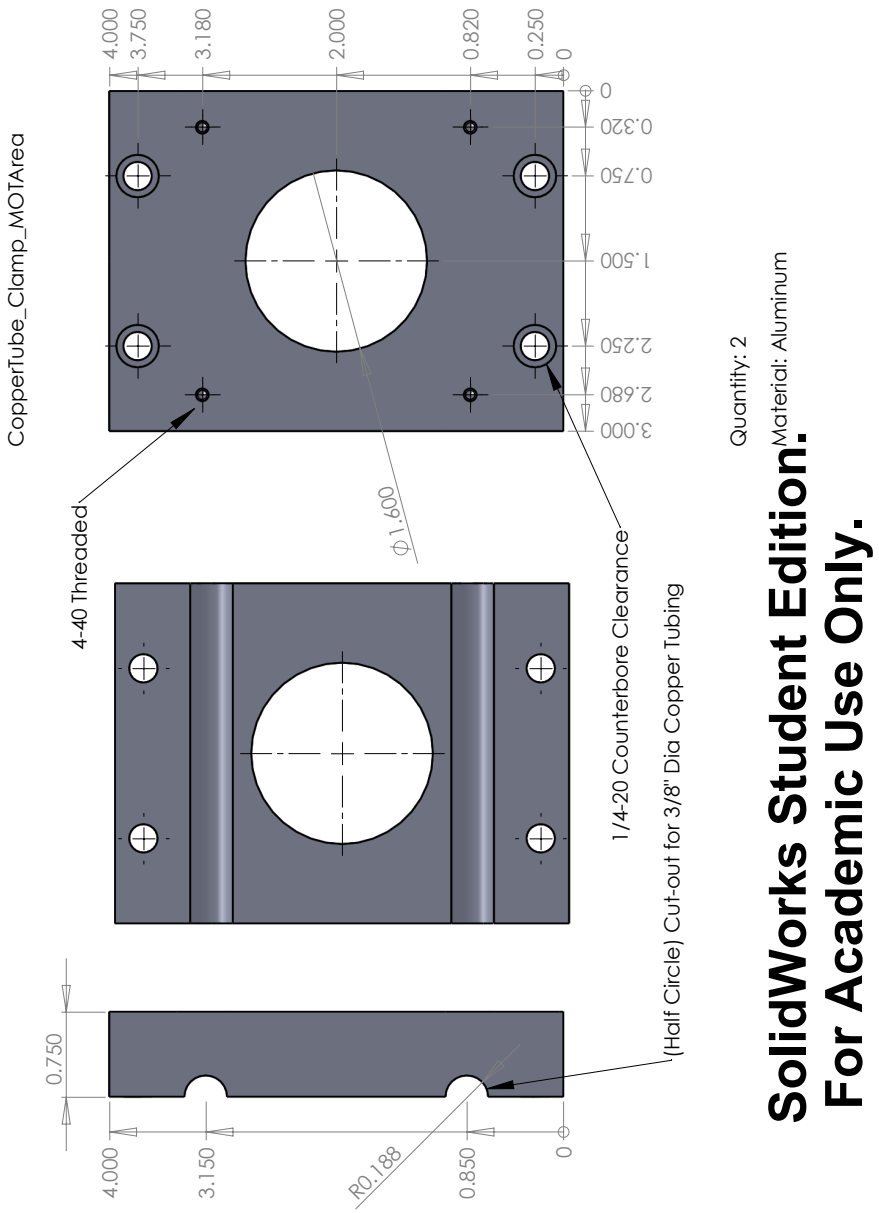

Figure B.9: MOT region cooling tube clamp. Adapts to Thorlabs cage.

Figure B.10: Transport tower cold plate

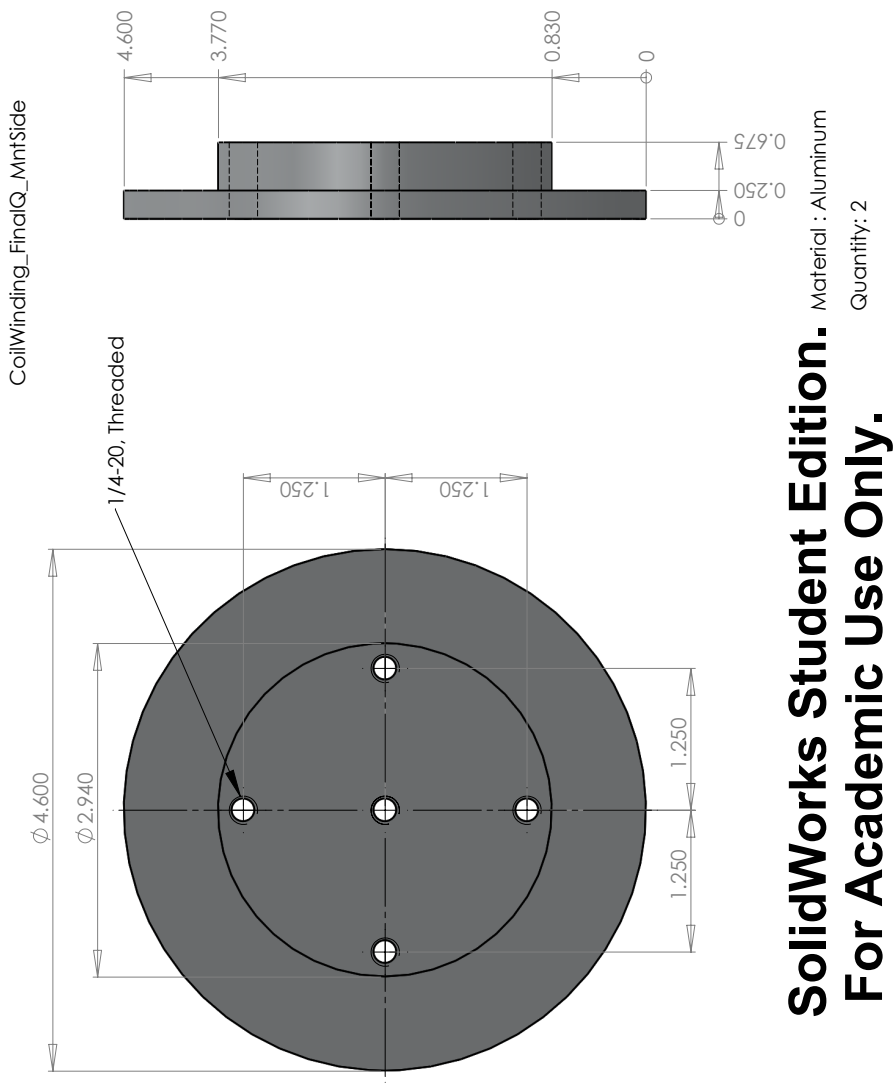

Figure B.11: Coil winding form: final coil

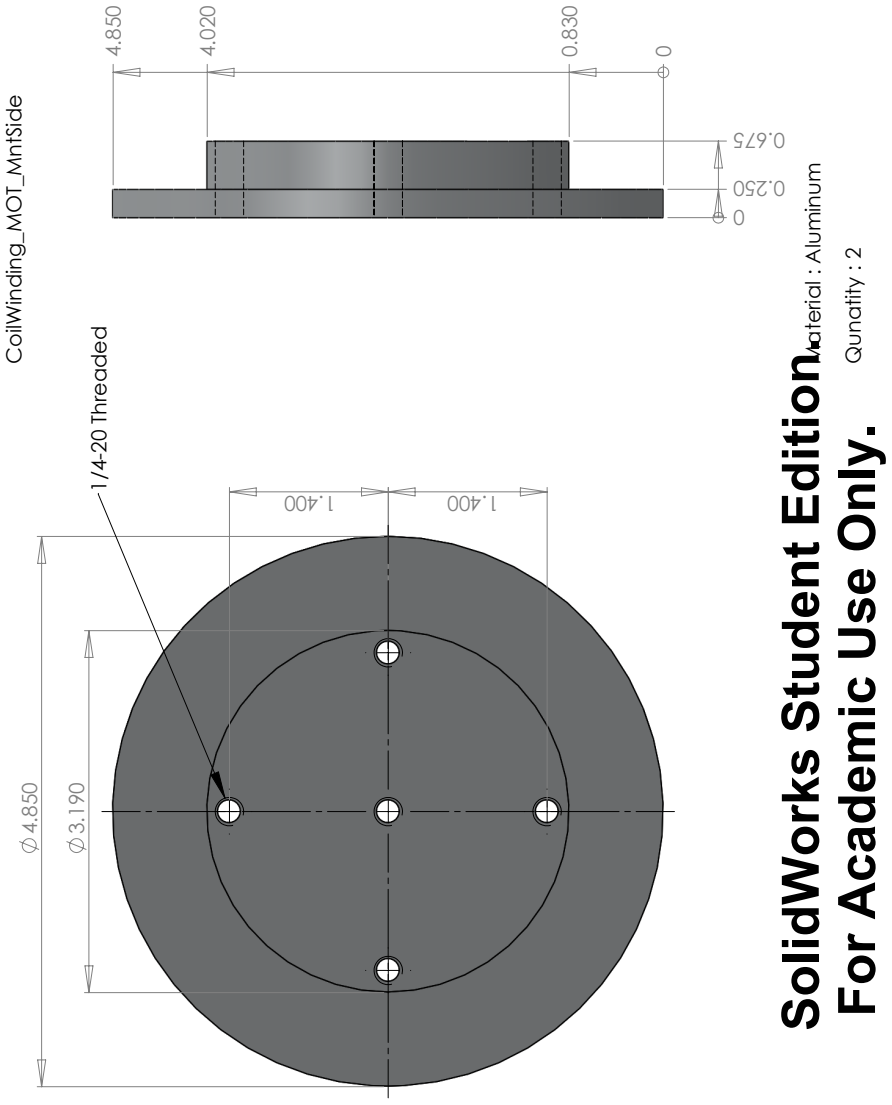

Figure B.12: Coil winding form: MOT coil

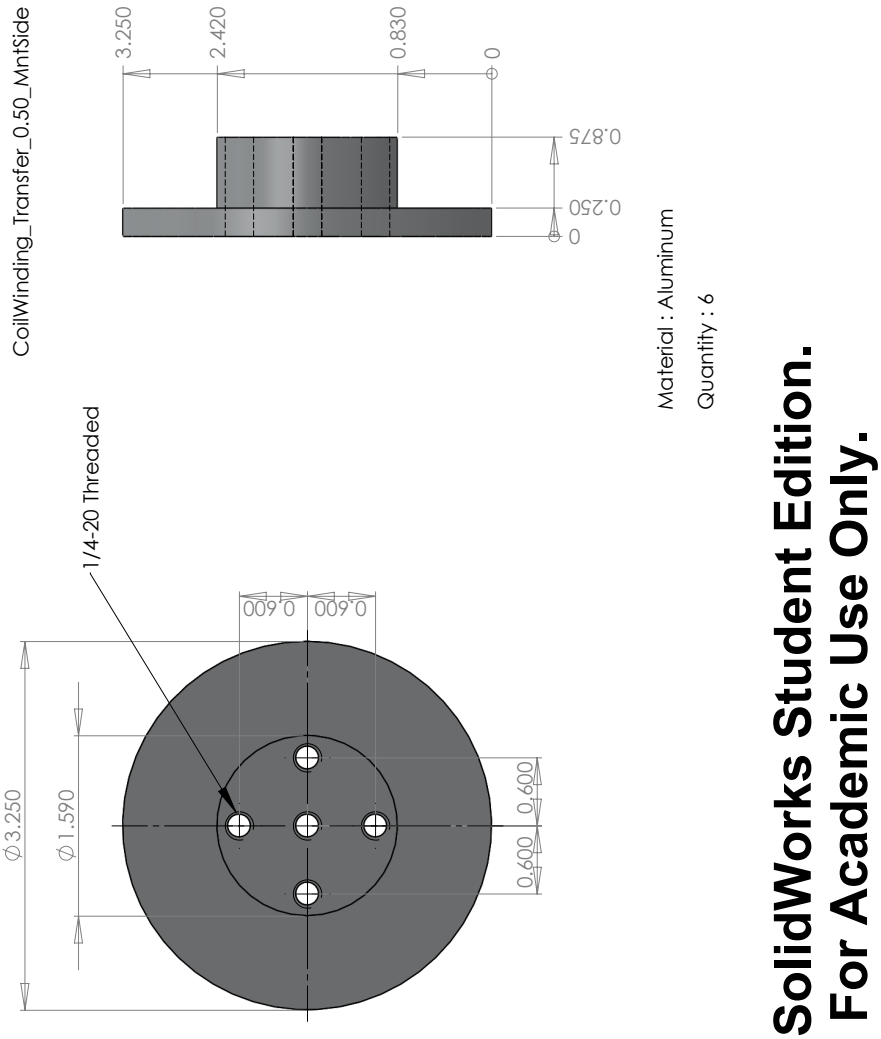

Figure B.13: Coil winding form: "Top" coil

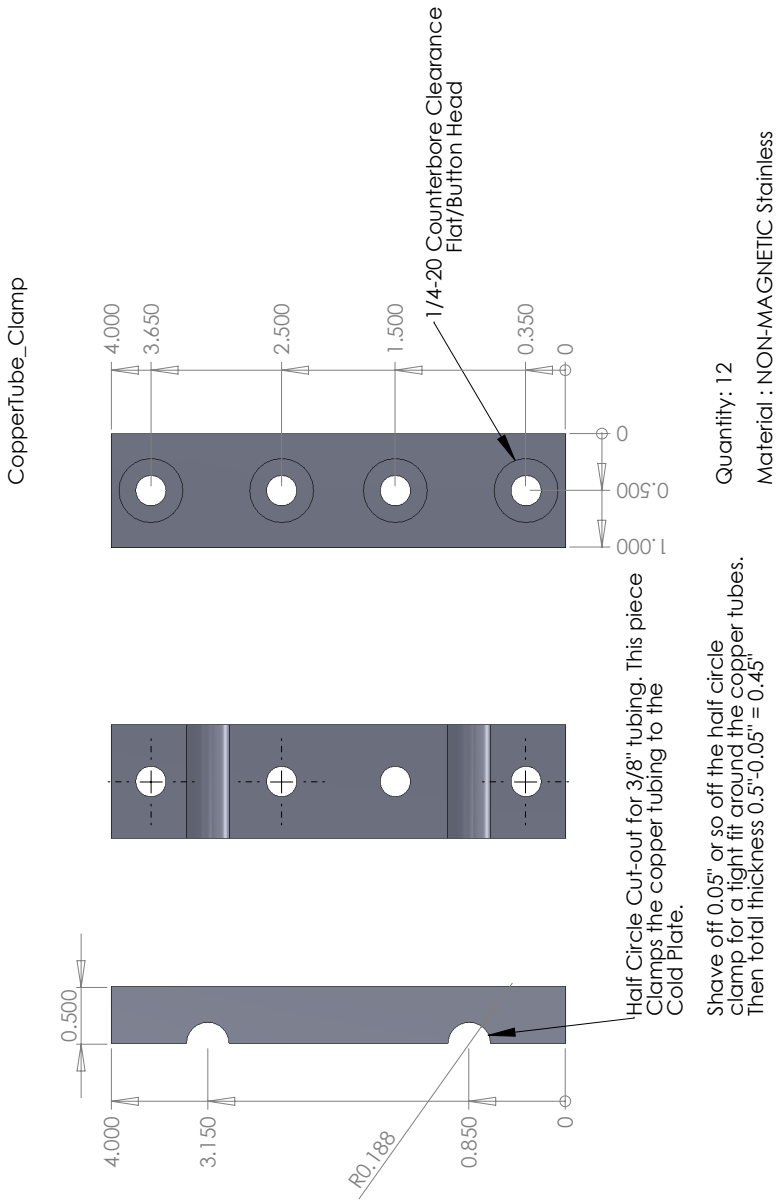

Figure B.14: Clamp for copper water cooling tube

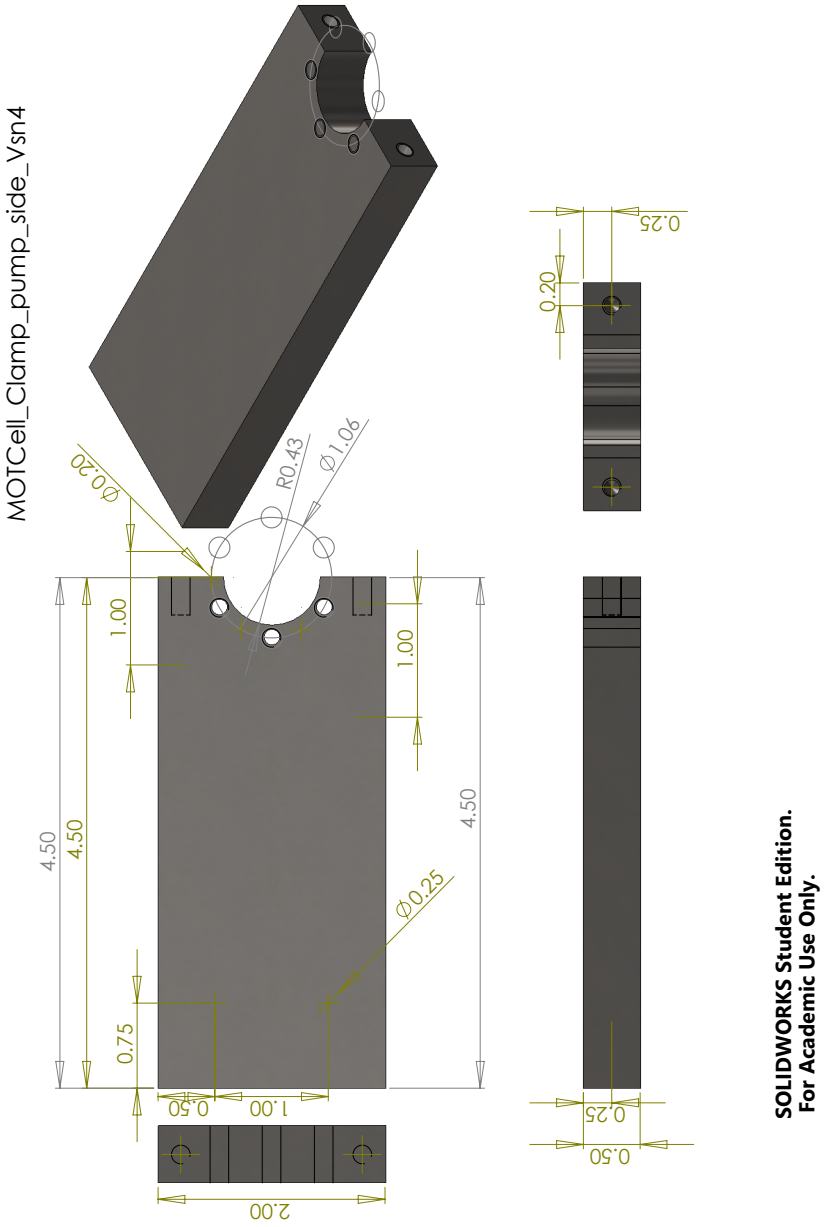

Figure B.15: MOT cell holder

Bibliography

[1] Xiao-Liang Qi and Shou-Cheng Zhang. Topological insulators and superconductors. *Rev. Mod. Phys.*, 83:1057–1110, Oct 2011.

[2] Y.-J. Lin, R. L. Compton, A. R. Perry, W. D. Phillips, J. V. Porto, and I. B. Spielman. Bose-einstein condensate in a uniform light-induced vector potential. *Phys. Rev. Lett.*, 102:130401, Mar 2009.

[3] R. A. Williams, L. J. LeBlanc, K. Jimnez-Garca, M. C. Beeler, A. R. Perry, W. D. Phillips, and I. B. Spielman. Synthetic partial waves in ultracold atomic collisions. *Science*, 335(6066):314–317, 2012.

[4] L J LeBlanc, M C Beeler, K Jimnez-Garca, A R Perry, S Sugawa, R A Williams, and I B Spielman. Direct observation of zitterbewegung in a boseeinstein condensate. *New Journal of Physics*, 15(7):073011, 2013.

[5] M C Beeler, R a Williams, K Jiménez-García, L J LeBlanc, a R Perry, and I B Spielman. The spin Hall effect in a quantum gas. *Nature*, 498(7453):201–4, 2013.

[6] N. Goldman, I. Satija, P. Nikolic, A. Bermudez, M. A. Martin-Delgado, M. Lewenstein, and I. B. Spielman. Realistic time-reversal invariant topological insulators with neutral atoms. *Phys. Rev. Lett.*, 105:255302, Dec 2010.

[7] Y.-J. Lin, A. R. Perry, R. L. Compton, I. B. Spielman, and J. V. Porto. Rapid production of ^{87}Rb Bose-Einstein condensates in a combined magnetic and optical potential. *Phys. Rev. A*, 79:063631, Jun 2009.

[8] HUI ZHAI. Spin-orbit coupled quantum gases. *International Journal of Modern Physics B*, 26(01):1230001, 2012.

[9] Jean Dalibard, Fabrice Gerbier, Gediminas Juzeliūnas, and Patrik Öhberg. *Colloquium* : Artificial gauge potentials for neutral atoms. *Rev. Mod. Phys.*, 83:1523–1543, Nov 2011.

[10] N Goldman, G Juzelinas, P hberg, and I B Spielman. Light-induced gauge fields for ultracold atoms. *Reports on Progress in Physics*, 77(12):126401, 2014.

[11] M. H. Anderson, J. R. Ensher, M. R. Matthews, C. E. Wieman, and E. A. Cornell. Observation of bose-einstein condensation in a dilute atomic vapor. *Science*, 269(5221):198–201, 1995.

[12] K. B. Davis, M. O. Mewes, M. R. Andrews, N. J. van Druten, D. S. Durfee, D. M. Kurn, and W. Ketterle. Bose-einstein condensation in a gas of sodium atoms. *Phys. Rev. Lett.*, 75:3969–3973, Nov 1995.

[13] Lindsay J. LeBlanc, Karina Jimnez-Garca, Ross A. Williams, Matthew C. Beeler, Abigail R. Perry, William D. Phillips, and Ian B. Spielman. Observation of a superfluid hall effect. *Proceedings of the National Academy of Sciences*, 109(27):10811–10814, 2012.

[14] K. Jiménez-García, L. J. LeBlanc, R. A. Williams, M. C. Beeler, A. R. Perry, and I. B. Spielman. Peierls substitution in an engineered lattice potential. *Phys. Rev. Lett.*, 108:225303, May 2012.

[15] Y.-J. Lin, R. L. Compton, K. Jimenez-Garcia, J. V. Porto, and I. B. Spielman. Synthetic magnetic fields for ultracold neutral atoms. *Nature*, 462:628–632, Dec 2009.

[16] Y.-J. Lin, R. L. Compton, K. Jimenez-Garcia, W. D. Phillips, J. V. Porto, and I. B. Spielman. A synthetic electric force acting on neutral atoms. *Nat Phys*, 7:531–534, Mar 2011.

[17] Y.-J. Lin, K. Jimenez-Garcia, and I. B. Spielman. Spin-orbit-coupled bose-einstein condensates. *Nature*, 471:83–86, Mar 2011.

[18] J. Higbie and D. M. Stamper-Kurn. Periodically dressed bose-einstein condensate: A superfluid with an anisotropic and variable critical velocity. *Phys. Rev. Lett.*, 88:090401, Feb 2002.

[19] J. Higbie and D. M. Stamper-Kurn. Generating macroscopic-quantum-superposition states in momentum and internal-state space from bose-einstein condensates with repulsive interactions. *Phys. Rev. A*, 69:053605, May 2004.

[20] I. B. Spielman. Raman processes and effective gauge potentials. *Phys. Rev. A*, 79:063613, Jun 2009.

[21] K. Jiménez-García, L. J. LeBlanc, R. A. Williams, M. C. Beeler, A. R. Perry, and I. B. Spielman. Peierls substitution in an engineered lattice potential. *Phys. Rev. Lett.*, 108:225303, May 2012.

[22] Y. K. Kato, R. C. Myers, A. C. Gossard, and D. D. Awschalom. Observation of the spin hall effect in semiconductors. *Science*, 306(5703):1910–1913, 2004.

[23] J. Wunderlich, B. Kaestner, J. Sinova, and T. Jungwirth. Experimental observation of the spin-hall effect in a two-dimensional spin-orbit coupled semiconductor system. *Phys. Rev. Lett.*, 94:047204, Feb 2005.

[24] J. H. Huckans, I. B. Spielman, B. Laburthe Tolra, W. D. Phillips, and J. V. Porto. Quantum and classical dynamics of a bose-einstein condensate in a large-period optical lattice. *Phys. Rev. A*, 80:043609, Oct 2009.

[25] Yu-ju Lin, Igor Teper, Cheng Chin, and Vladan Vuletić. Impact of the casimir-polder potential and johnson noise on bose-einstein condensate stability near surfaces. *Phys. Rev. Lett.*, 92:050404, Feb 2004.

[26] M. Trinker, S. Groth, S. Haslinger, S. Manz, T. Betz, S. Schneider, I. Bar-Joseph, T. Schumm, and J. Schmiedmayer. Multilayer atom chips for versatile atom micromanipulation. *Applied Physics Letters*, 92(25):–, 2008.

[27] B. P. Anderson and M. A. Kasevich. Loading a vapor-cell magneto-optic trap using light-induced atom desorption. *Phys. Rev. A*, 63:023404, Jan 2001.

[28] Gustavo Telles, Tetsuya Ishikawa, Matthew Gibbs, and Chandra Raman. Light-induced atomic desorption for loading a sodium magneto-optical trap. *Phys. Rev. A*, 81:032710, Mar 2010.

[29] Markus Greiner, Immanuel Bloch, Theodor W. Hänsch, and Tilman Esslinger. Magnetic transport of trapped cold atoms over a large distance. *Phys. Rev. A*, 63:031401, Feb 2001.

[30] E. L. Raab, M. Prentiss, Alex Cable, Steven Chu, and D. E. Pritchard. Trapping of neutral sodium atoms with radiation pressure. *Phys. Rev. Lett.*, 59:2631–2634, Dec 1987.

[31] Steven Chu, L. Hollberg, J. E. Bjorkholm, Alex Cable, and A. Ashkin. Three-dimensional viscous confinement and cooling of atoms by resonance radiation pressure. *Phys. Rev. Lett.*, 55:48–51, Jul 1985.

[32] David E. Pritchard. Cooling neutral atoms in a magnetic trap for precision spectroscopy. *Phys. Rev. Lett.*, 51:1336–1339, Oct 1983.

[33] O. J. Luiten, M. W. Reynolds, and J. T. M. Walraven. Kinetic theory of the evaporative cooling of a trapped gas. *Phys. Rev. A*, 53:381–389, Jan 1996.

[34] Y.-J. Lin, A. R. Perry, R. L. Compton, I. B. Spielman, and J. V. Porto. Rapid production of ^{87}rb bose-einstein condensates in a combined magnetic and optical potential. *Phys. Rev. A*, 79:063631, Jun 2009.

[35] Wolfgang Petrich, Michael H. Anderson, Jason R. Ensher, and Eric A. Cornell. Stable, tightly confining magnetic trap for evaporative cooling of neutral atoms. *Phys. Rev. Lett.*, 74:3352–3355, Apr 1995.

[36] J. Sding, D. Gury-Odelin, P. Desbiolles, F. Chevy, H. Inamori, and J. Dalibard. Three-body decay of a rubidium Bose-Einstein condensate. *Applied Physics B*, 69(4):257–261, 1999.

[37] H. Smith C.J. Pethick. *Bose-Einstein Condensation in Dilute Gases*. Cambridge University Press, 2008.

[38] I. Geisel, K. Cordes, J. Mahnke, S. Jllenbeck, J. Ostermann, J. Arlt, W. Ertmer, and C. Klempt. Evolutionary optimization of an experimental apparatus. *Applied Physics Letters*, 102(21):–, 2013.

[39] R. C. Brown. Nonequilibrium manybody dynamics with ultracold atoms in optical lattices and selected problems in atomic physics. *Ph.D. Thesis*, 2014.

[40] Alexander Franzen. Componentlibrary. *licensed under a Creative Commons Attribution-NonCommercial 3.0 Unported License*.

[41] L. D. Turner, K. F. E. M. Domen, and R. E. Scholten. Diffraction-contrast imaging of cold atoms. *Phys. Rev. A*, 72:031403, Sep 2005.

[42] Lincoln D. Turner, Karl P. Weber, David Paganin, and Robert E. Scholten. Off-resonant defocus-contrast imaging of cold atoms. *Opt. Lett.*, 29(3):232–234, Feb 2004.

[43] L. D. Turner. Holographic imaging of cold atoms. *PhD Thesis, University of Melbourne*, 2004.

[44] W. Ketterle, D. S. Durfee, and D.M. Stamper-Kurn. Making, probing and understanding Bose-Einstein condensates. *In Bose-Einstein condensation in atomic gases, Proceedings of the International School of Physics "Enrico Fermi", Course CXL*, pages 67–176, 1999.

[45] M. R. Andrews, D. M. Kurn, H.-J. Miesner, D. S. Durfee, C. G. Townsend, S. Inouye, and W. Ketterle. Propagation of sound in a Bose-Einstein condensate. *Phys. Rev. Lett.*, 79:553–556, Jul 1997.

[46] Andika Putra, Daniel L. Campbell, Ryan M. Price, Subhadeep De, and I. B. Spielman. Optimally focused cold atom systems obtained using density-density correlations. *Review of Scientific Instruments*, 85(1):–, 2014.

[47] G. Reinaudi, T. Lahaye, Z. Wang, and D. Guéry-Odelin. Strong saturation absorption imaging of dense clouds of ultracold atoms. *Opt. Lett.*, 32(21):3143–3145, Nov 2007.

[48] A. N. Tikhonov and V. Y. Arsenin. Solution of ill-posed problems. *Washington, DC.: V. H. Winston and Sons*, 1977.

[49] Markus Greiner, Immanuel Bloch, Theodor W. Hänsch, and Tilman Esslinger. Magnetic transport of trapped cold atoms over a large distance. *Phys. Rev. A*, 63:031401, Feb 2001.

[50] Anand Ramanathan, Srgio R. Muniz, Kevin C. Wright, Russell P. Anderson, William D. Phillips, Kristian Helmerson, and Gretchen K. Campbell. Partial-transfer absorption imaging: A versatile technique for optimal imaging of ultracold gases. *Review of Scientific Instruments*, 83(8):083119, 2012.

[51] Daniel A Steck. Rubidium 87 d line data, 2001.

[52] M. D. Feit and J. A. Fleck. Light propagation in graded-index optical fibers. *Appl. Opt.*, 17(24):3990–3998, Dec 1978.

[53] Fabrice Gerbier and Jean Dalibard. Gauge fields for ultracold atoms in optical superlattices. *New Journal of Physics*, 12(3):033007, 2010.

[54] Xiaoling Cui, Biao Lian, Tin-Lun Ho, Benjamin L Lev, and Hui Zhai. Synthetic gauge field with highly magnetic lanthanide atoms. *Physical Review A*, 88(1):011601, 2013.

[55] G. Breit and I. I. Rabi. Measurement of nuclear spin. *Phys. Rev.*, 38:2082–2083, Dec 1931.